Dissertation
submitted to the
Combined Faculty of Natural Sciences and Mathematics
of Heidelberg University, Germany
for the degree of
Doctor of Natural Sciences

Put forward by
Shirin, Rahmanian
born in: Mashhad, Iran
Oral examination: May 5th, 2020

Application of Fluorescent Nuclear Track Detectors for Cellular Dosimetry in Ion Beam Radiotherapy

Referees: Prof. Dr. João Seco
Prof. Dr. Oliver Jäkel

Declaration

I, Shirin Rahmanian , declare here that this Ph.D. thesis is the result of my own research, and that all sources used in this work have been duly referenced. This thesis has not been submitted to any other university or institute for a degree award.

Heidelberg, February 24$^{\text{th}}$, 2020

.....

Shirin Rahmanian

Abstract

Ion beam radiotherapy (IBRT) offers a more conformal dose distribution and an enhanced relative biological effectiveness (RBE) in the Bragg peak region as compared to conventional photon therapy. This enhanced RBE is due to the highly localized energy deposition pattern of ion beams, which due to its stochastic nature, is subject to large fluctuations on cellular and sub-cellular scales, resulting in a large variation of biological response in cells exposed to the same beam.Therefore, a cell hybrid detector capable of quantifying local energy deposition at such microscopic scales and correlating it to a biological response is highly desirable. For this purpose, Fluorescent Nuclear Track Detectors (FNTDs) covered with cells have been shown to be an effective cell-hybrid detector, as they can provide information on individual cellular energy deposition with the ability to directly visualize cellular response. In this thesis, a new framework, referred to as the "Cell Dose" model, was established to define dosimetric quantities relevant for quantifying energy deposition at sub-cellular scales, that can be measured with FNTDs as a model detector: specific dose and specific LET. When energy deposition inside the cell nuclei is of interest, the "Cell Dose" quantities can complement the microdosimetric and macroscopic quantities as intermediate quantities between the two. The theoretical framework includes a sampling method that incorporates uncertainties due to five different sources of variations: cross-sectional area of the nuclei, number of particles entering the cell nucleus, the chord lengths of the particles inside the cell nucleus, the linear energy transfer (LET) of the individual particle, and the energy loss straggling of the particles inside the cell nucleus. The distribution of the new dosimetric terms specific dose and specific LET in the cell-wide population was studied for different ions and energies at different depths of their depth-dose profiles, and the individual contribution of these different sources was assessed. The results indicated that there is a great variation (24-55%) in terms of energy deposition in the cell nuclei, with LET variation of the particles as the major contributor. It was shown that with the use of microscopy and FNTDs, the uncertainty in measurement can potentially be reduced down to only 4-14 %. Furthermore, these dosimetric quantities were compared to experimental results with FNTDs which indicated the possibility of correlating the physical parameters, obtained from FNTDs, to different biological response parameters. With additional improvements and studies, the new "Cell Dose" model may be a valuable tool in radiobiological studies with ion beams, as it can provide valuable information to better understand the underlying physical nature of ion beams in producing cellular response.

Zusammenfassung

Die Ionenstrahlherapie (IBRT) bietet eine präzisere Dosisverteilung und eine verbesserte relative biologische Wirksamkeit (RBW) im Bereich des *Bragg-Peaks* im Vergleich zur konventionellen Photonentherapie. Diese verbesserte RBW ist auf das hochgradig lokalisierte Muster der Energiedeposition von Ionenstrahlen zurückzuführen, das aufgrund seiner stochastischen Natur großen Schwankungen auf zellulärer und subzellulärer Ebene unterliegt, was zu einer größen Variation der biologischen Reaktion in Zellen führt, die dem gleichen Strahl ausgesetzt sind. Daher ist ein Zell-Hybriddetektor, der in der Lage ist, lokale Energiedeposition auf solchen mikroskopischen Skalen zu quantifizieren und mit einer biologischen Reaktion zu korrelieren, sehr wünschenswert. Zu diesem Zweck haben sich mit Zellen bedeckte Fluoreszenz-Kernspurdetektoren (FNTDs) als wirksamer Zell-Hybriddetektor erwiesen, da sie Informationen über die individuelle Energiedeposition innerhalb der Zelle mit der Möglichkeit zur direkten Visualisierung der zellulären Reaktion liefern können. In dieser Arbeit wurde ein neuer Rahmen, das so genannte "Zelldosis"-Modell, geschaffen, um dosimetrische Größen zu definieren, die für die Quantifizierung der Energiedeposition auf subzellulären Skalen relevant sind und die mit FNTDs als Modelldetektor gemessen werden können: spezifische Dosis und spezifischer LET. Wenn die Energiedeposition innerhalb der Zellkerne von Interesse ist, können die "Zelldosis"-Größen die mikrodosimetrischen und makroskopischen Größen als Zwischengrößen zwischen den beiden ergänzen. Der theoretische Rahmen umfasst eine Sampling-Methode, die Unsicherheiten aufgrund von fünf verschiedenen Variationsquellen berücksichtigt: die Querschnittsfläche des Zellkerns, die Anzahl der in den Zellkern eintretenden Teilchen, die Pfadlängen der Partikel im Inneren des Zellkerns, den linearen Energietransfer (LET) des einzelnen Teilchens und der Streuung des Energieverlusts der Teilchen im Zellkern. Die Verteilung der neuen dosimetrischen Größen spezifische Dosis und spezifischer LET in der zellweiten Population wurde für verschiedene Ionen und Energien in verschiedenen Tiefen ihrer Tiefendosisprofile untersucht, und der Beitrag dieser verschiedenen Quellen wurde bewertet. Die Ergebnisse zeigen, dass es eine große Variation (24-55%) in Bezug auf die Energiedeposition in den Zellkernen gibt, wobei die LET-Variation der Teilchen den größten Beitrag ausmacht. Es wurde gezeigt, dass die Messunsicherheit durch den Einsatz von Mikroskopie und FNTDs potenziell auf nur 4-14% reduziert werden kann. Außerdem wurden diese dosimetrischen Größen mit experimentellen Ergebnissen mit FNTDs verglichen, was die Möglichkeit aufgezeigt hat, die mit FNTDs gewonnenen physikalischen Parameter mit verschiedenen biologischen Reaktionsparametern zu korrelieren. Mit zusätzlichen Verbesserungen und Studien kann das neue "Zelldosis"-Modell ein wertvolles Werkzeug in strahlenbiologischen Studien mit Ionenstrahlen sein, da es wertvolle Informationen zum besseren Verständnis der zugrunde liegenden physikalischen Natur von Ionenstrahlen bei der Erzeugung der zellulären Reaktion liefern kann.

Table of Contents

Chapter 1

Introduction

1.1 Motivation

In radiation therapy, in order to inactivate cancer cells, the tumor is exposed to ionizing radiation, which deposits energy in the exposed cells causing DNA damage. This DNA damage, which can lead to cell death, is the main target of radiotherapy [1, 2]. Conventional radiotherapy is performed with photons, namely x-ray or gamma rays, and since the discovery of x-rays in 1895, has been successfully used in clinics worldwide. The majority of the energy deposited from the photons is delivered at relatively shallow depths below the skin, and the rest is gradually lost until the photon exits the body. Such pattern of energy deposition makes photon therapy not ideal for deep-seated tumors or for tumors that require high dose of radiation, since the surrounding healthy tissues will also get damaged, posing a high risk in critical organs. Radiation therapy with charged particles such as protons and heavier ions, commonly referred to as ion beam radiotherapy (IBRT), is used as an alternative method to overcome this challenge and has gained tremendous popularity over the past few decades [3, 4]. Energy deposition of ion beams [Section 2.2] is characterized by gradual energy loss as the particle slows down in matter, and when the ion finally stops, the maximum energy loss is reached in the so called Bragg peak. This inverse depth-dose profile of ion beams (as shown in Figure 1.1) offers a unique advantage over photons as it allows for better dose precision and localization of the radiation damage to the tumor, thus sparing more healthy tissues.

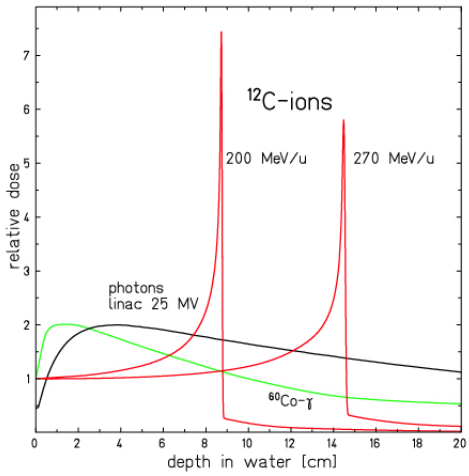

Figure 1.1: Depth-dose profiles of carbon ions as compared to photons. Reprinted from [4].

Furthermore, heavier ions such as carbon ions have the additional advantage of increasing ionization density towards the Bragg Peak, which results in increased relative biological effectiveness (RBE) in the Bragg peak as compared to the entrance region [5]. This differential RBE increase is one of the main rationales for use of the carbon ions in the clinics. The fundamental reason for the altered RBE of heavy ions compared to photons and protons lies in the way that heavier ions deposit their energy on a microscopic scale, which is characterized by higher ionization density around the primary ion track that increases toward the distal edge of the spread-out Bragg peaks (SOBP) [5]. While this RBE differential observed in heavier ions has a great clinical advantage, it poses a new challenge for treatment planning as its calculation is based on predictions from experimental data and not easily computable as many different factors are in play, such as physical properties of the ion beam, the fragmentation process of the primary beam, type of the irradiated tissue and the biological environment of the target. To address the problem of RBE calculation, many ion-beam treatment facilities have incorporated a form of biophysical modeling [Section 2.10]. However, in correlating the physical properties of the ion beams to biological response, there still remains a huge gap of knowledge in the underlying mechanisms. One of the steps that can help to shorten this gap is correlating the physical parameters to single cell biological outcome, and consequently studying the effects of energy deposition in single cells and its variation on the wider cell population. Such single-cell characterization is particularly important as radiobiological experiments have shown that cells exposed to the same beam can vary greatly in their biological response [6]. It is believed that this cellular variation

in biological response is mainly due to the stochastic nature of energy deposition of heavy charged particles at microscopic scales. Therefore, radiobiological experiments using cell-hybrid detectors consisting of a physical compartment to detect and measure physical beam properties at microscopic level and a biological compartment to directly observe the biological outcome offer a great way to correlate the two and gain more insights in the cellular and physical mechanisms involved.

Fluorescent Nuclear Track Detectors (FNTDs) covered with cells have been shown to be effective cell-hybrid detectors for this purpose as they allow for direct visualization of ion tracks after irradiation in cells and have been recently used for correlating different biological endpoints [7–9]. However, to characterize the physical effects for such understanding at the cellular level, it is not clear which physical quantities to use, since macroscopic quantities [Section 2.3] (i.e. as obtained from treatment planning or the beam quality) are not adequate to describe the damage at the cellular level. Microdosimetric quantities [Section 2.6], such as lineal energy or specific energy, or even further nano scale quantities are not at a scale that is suited to be used with currently available hybrid techniques in radiobiological experiments. Consequently, the goal of this thesis is to establish a framework for single cell dosimetry (the new "Cell Dose" model), which consists of a formalism to define appropriate quantities and tools to study their behavior computationally and to experimentally measure them.

1.2 Aims

To achieve the goal mentioned above, the aims of this thesis are given as follows:

- Creating a new "Cell Dose" model based on theoretical/computational methods for calculating energy deposition and its variation at a single cell level and defining relevant dosimetric terms based on most relevant sources of energy variation.
- Using the new model to study different clinically relevant conditions to calculate new "Cell Dose" quantities and cellular energy deposition variation in order to compare different ion types, irradiation plans, irradiation parameters and different depth positions.
- Applying the new "Cell Dose" model to test the applicability of cell-hybrid detectors by obtaining uncertainty values for the dosimetric terms and variation sources that were defined and chosen in the established framework.
- Using experimental data with FNTDs to benchmark the theoretical/computational model and provide some current applicable examples and identify the advantage and shortcomings of current techniques in order to suggest improvements for future studies.

Chapter 2

Theoretical Background

2.1 Ionizing Radiation

Radiation refers to the transport of energy from a source through vacuum or a medium in the form of electromagnetic waves (photons) or subatomic particles. If the energy of the particle or photon is high enough to ionize molecules or atoms of the medium (target material), it is referred to as ionizing radiation. Charged particles, which are the subject under study in this work, are classified as directly ionizing radiation as they can directly ionize the atoms or molecules of the target material. Neutral particles (photons and neutrons), however, are referred to as indirectly ionizing since they first release their energy to a charged particle in the target material, which in turn causes the target ionization.

2.2 Interaction of Charged Particles with Matter

When a charged particle passes through matter, its Coulomb electric field interacts with the orbital electrons and nuclei of the target material, resulting in partial loss of its kinetic energy [10]. Usually, the energy transfer from the particle to the target matter is small, therefore the particle undergoes many interactions until all of its kinetic energy is transferred to the matter. The probability of any type of interaction, or in other terms the interaction cross section (σ), depends on the type of the particle and its kinetic energy. To further distinguish charged particles, they are divided into light particles (ie. electrons and positrons) and heavy charged particles (ions). In this thesis, only charged particles with $Z \leq 10$ are considered, as heavier ions are not used in radiation therapy, and so their interaction is beyond the scope of this thesis. Heavy

charged particles lose their energy mainly by inelastic collision with the orbital electrons of the target material, and compared to electrons the interaction with target nuclei is mainly via scattering and fragmentation and thus do not lose any significant amount of energy through Bremsstrahlung radiation [10]. Another difference in interaction of heavier particles compared to electrons is that, due to their much heavier mass, they do not scatter much when they traverse the target material after each collision. Therefore, direction of the impinging ion remains mainly constant as they lose energy, which results in a well-defined range in the target material. This finite range is of great importance in radiation therapy as it allows for a more precise dose localization in the targeted volume.

Furthermore, due to the high mass and less scattering, the mean energy loss per unit length , ($\frac{\overline{dE}}{dx}$), is quite different for heavy charged particles compared to photons and electrons. The mean energy loss per unit length for therapeutic ions of relatively high initial kinetic energy (50-400 MeV/u) is described by the relativistic Bethe formula [11]:

$$\frac{\frac{\overline{dE}}{dx}}{\rho} = K \cdot \frac{{z_{eff}}^2}{\beta^2} \cdot \frac{Z}{A} \cdot [\frac{1}{2} \ln(\frac{2 \cdot m_e \cdot c^2 \cdot \beta^2 \cdot W_{max}}{I^2 \cdot (1-\beta^2)}) - \beta^2 + corr] \tag{2.1}$$

where K=0.30705 MeV cm^2 g^{-2} , z_{eff} is the effective charge of the projectile, β is its relativistic velocity, Z and A are the atomic number and atomic mass of the medium, respectively, W_{max} is the maximum energy transferable to a free electron in a single collision, I is the mean excitation energy of the medium, m_e is the mass of electron, c is the speed of light, and *corr* is the collection of different correction terms that account for different effects (density effect, shell, Barkas and Bloch correction).

As seen from the Bethe equation (Eq 2.1) the stopping power varies mainly as a function of $\frac{z^2}{\beta^2}$, so the stopping power should increase with decreasing speed. However, the effective charge of the projectile reduces as it gradually collects target electrons, which reduces the energy loss. The combination of these two features produces a sharp rise and fall of energy deposition at the end of the ion track, the so called Bragg peak, rendering the characteristic depth-dose profile of heavy charged particles (as shown by the red curves in Figure 1.1). This "inverted" depth-dose profile of ion beams is exploited in radiotherapy in order to concentrate the maximum dose to the tumor while minimizing the damage to surrounding healthy tissue. In clinical applications, in order to irradiate the entire tumor with high dose, several monoenergetic ion Bragg peaks can be superimposed to form a so called spread-out Bragg peak (SOBP) (as shown in Figure 2.1).

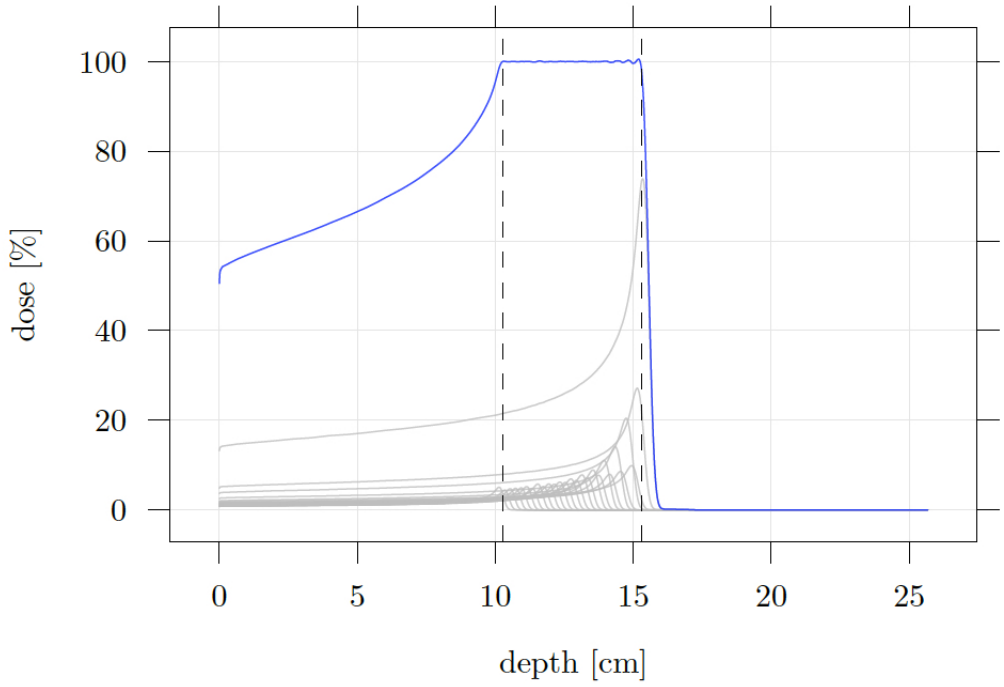

Figure 2.1: Spread-out Bragg peak (SOBP) for carbon ions (shown in blue) showing the individual pristine Bragg curves (gray) that were superimposed to form the SOBP.

While lateral scattering and nuclear interactions don't play an important role in the energy loss process of heavy charged particles, they are factors that characterize the ion track and its particle spectrum in matter, and therefore need to be considered in radiation treatment planning. Elastic scattering of heavy charged particles occur in very small angles compared to electrons due to their large mass and can be described by Rutherford's scattering formula [12]. In a thick layer, multiple Coulomb scattering occurs and can be estimated by theories such as Moliere [13] and Highland's theory [14]. While each time the projectile is deflected by a small angle, the effect of angular deflection increases and causes a lateral spread, known as the lateral penumbra. As particles traverse through matter, the penumbra increases with depth and decreasing energy, causing an increased beam penumbra at the distal end of the particle range. The other feature of heavier ions, such as carbon ions, is the nuclear fragmentation of the projectile arising from nuclear interaction of the ion with the target nuclei. This fragmentation causes mainly an accumulation the ion's fragments (secondary particles) with same velocity of the impinging ions (primary particles), resulting in a spectrum of different particles with different charges and masses. Due to very low recoil energy

and short range, target fragmentation only contributes an insignificant amount to this spectrum. The fragments with smaller Z have a larger range in matter than the primary ion. This longer range of different fragments is responsible for the tail after the Bragg peak in heavier ions, which needs to be considered in treatment planning.

2.3 Dosimetric Quantities and Terms

In this section, the radiometric and dosimeteric terms relevant to the work of this thesis are defined mainly in accordance and convention of the most recent reports of International Commission on Radiation Units and Measurements (ICRU) [15]

2.3.1 Fluence

The fluence, Φ, is defined as the quotient of dN, the number of particles incident on a sphere and its cross-sectional area dA (as shown in Figure 2.2) :

$$\Phi = \frac{\mathrm{dN}}{\mathrm{dA}} \tag{2.2}$$

The unit for fluence is m^{-2}.

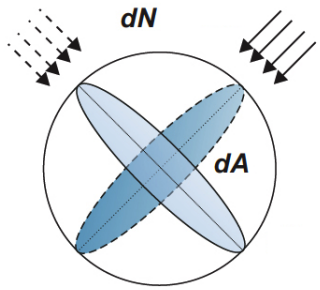

Figure 2.2: Areal definition of fluence

One can define an areal fluence Φ_A by summing all particles i that pass through an Area A having a polar angle ϑ with respect to the Area as:

$$\Phi_A = \sum_i \frac{1}{A.\cos(\vartheta_i)} \tag{2.3}$$

An alternative definition for dosimetric calculations using the volume and trajectory lengths of particles has been proposed by Papeiz and Battista [16] as follows:

$$\Phi_A = \sum_i \frac{dl_i}{dV} \tag{2.4}$$

where dl_i are the the sum of all particle trajectories' lengths in volume dV. A graphical representation of this fluence definition, as measured in FNTDs, is shown in Figure 2.3.

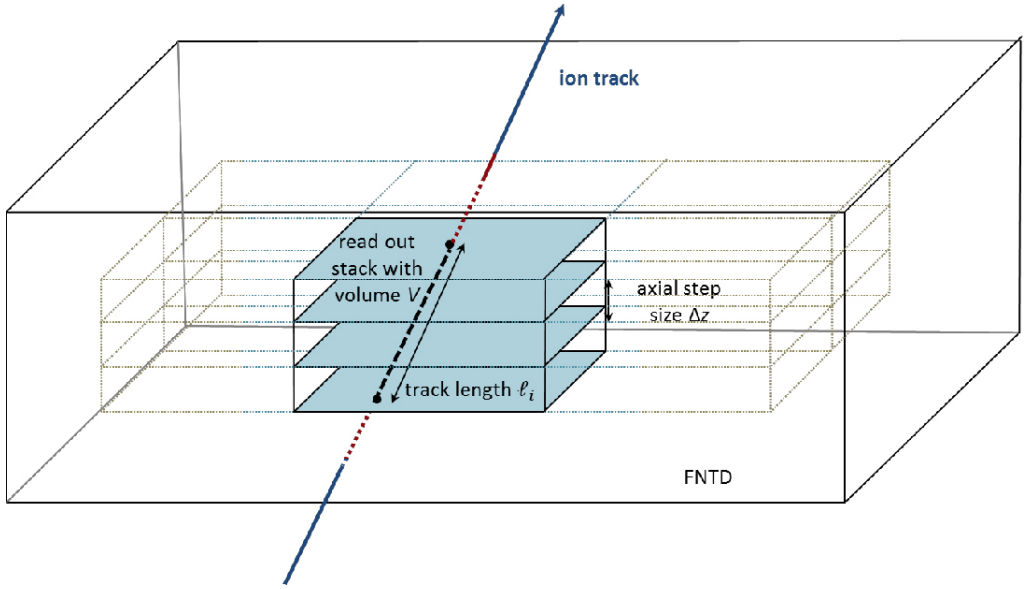

Figure 2.3: Volume definition of fluence

2.3.2 Energy Imparted

The energy imparted, ϵ, by radiation to matter in a given volume is defined as :

$$\epsilon = \sum_i \epsilon_i \tag{2.5}$$

where ϵ_i is the energy deposition in each single interaction i. This single energy deposition is given by:

$$\epsilon_i = \epsilon_{in} - \epsilon_{out} + Q \tag{2.6}$$

where ϵ_{in} is the energy of the impinging ionizing particle entering the interaction (except its rest energy) and ϵ_{out} is the sum of the energies of all charged and non-charged ionizing particles (except their rest energy) exiting the interaction. Q is the change of rest energies of the nucleus and elementary particles in this interaction.

Combining equations 2.5 and 2.6 the energy imparted to a given volume can be defined as:

$$\epsilon = R_{in} - R_{out} + \sum Q \tag{2.7}$$

where R_{in} is the sum of all radiant energy of charged and non-charged particles entering this volume (except for their rest energy), and R_{out} is the sum of all radiant energy emitted from this volume.

ϵ is a stochastic quantity and has the unit Joule (J). The term stochastic quantity, explained further in this chapter, refers to a quantity whose value varies randomly and thus cannot be predicted [10]. Since radiation is random in nature, the associated stochastic quantities are described by probability distributions, which are defined for finite domains only [10]. The expectation value of a stochastic quantity (as in here for example ϵ) is the mean (here $\bar{\epsilon}$) of its measured values, as the number n of observations approaches infinity.

2.3.3 Absorbed Dose

Absorbed dose, D in a given volume is defined as:

$$D = \frac{d\bar{\epsilon}}{dm} \tag{2.8}$$

where $d\bar{\epsilon}$ is the mean energy imparted by ionizing radiation in a volume of mass, dm. The unit for absorbed dose is J kg^{-1}. The specific name for this unit is called gray (Gy).

2.3.4 Stopping Power

Stopping power describes the stopping of charged particles in matter due to loss of energy from interactions with atomic electrons of the target. Stopping power is defined as quotient of the mean energy lost, $d\bar{E}$, by the charged particle by the distance, dx, transversed in matter:

$$S = \frac{d\bar{E}}{dx} \tag{2.9}$$

The unit for stopping power is J m^{-1}, which can also be expressed in keVμm^{-1}. Often, the mass stopping power, S/ρ, is used, which is the stopping power divided by the density of the material.

Absorbed dose D in a thin target material with density ρ can be calculated from stopping power for a parallel particle beam with fluence ϕ via the following relationship [4] :

$$D[Gy] = 1.6\text{x}10^{-9} \cdot S[\frac{keV}{\mu m}] \cdot \Phi[\text{cm}^{-2}] \cdot \frac{1}{\rho}[\frac{\text{cm}^3}{\text{g}}] \tag{2.10}$$

The stopping power can be expressed as sum of three independent components : electronic stopping power, radiative stopping power and nuclear stopping power:

$$S = (\frac{d\bar{E}}{dx})_{el} + (\frac{d\bar{E}}{dx})_{rad} + (\frac{d\bar{E}}{dx})_{nuc} \tag{2.11}$$

Electronic stopping power, S_{el}, is the stopping power due to inelastic electronic interactions which results in ionization or excitation of the target material and can be described by the Bethe equation (Eq. 2.1). Radiative stopping power, S_{rad}, is the stopping power due to bremsstrahlung emission in the electric fields of atomic nuclei or electrons. S_{rad} is proportional to the following properties of the projectile and the medium:

$$S_{rad} \propto \frac{Z^2 E}{m^2} \tag{2.12}$$

where Z is the atomic number of the medium and, E and m are the kinetic energy and mass of the projectile, respectively. Since the radiative stopping power decreases quadratically with the mass of the projectile, its contribution is negligible for ions and protons at therapeutic energies [10]. Nuclear stopping power, S_{nuc} is the stopping power resulting from elastic Coulomb interactions with the atomic nuclei, imparting recoil energy to the atoms. The total energy loss from S_{nuc} is small enough that it can be neglected when considering energy loss of heavy ions. However, the elastic collisions with the nuclei are the main cause of scattering of the charged particles [4].

2.3.5 Linear Energy Transfer

Linear Energy Transfer (LET) is a quantity used in radiation dosimetry and radiobiology to describe the radiation quality of ionizing radiation and is defined as the energy imparted locally to the medium per unit length. The restricted linear electronic energy transfer, L_Δ, is defined as the quotient of $d\bar{E_\Delta}$ by dx, where $d\bar{E_\Delta}$ is the mean energy loss of the charged particles from electronic interactions minus the mean of all kinetic energies of electrons released by the charged particles above the energy Δ, and dx is the distance traversed by the charged particles:

$$L_\Delta = \frac{d\bar{E}_\Delta}{dx} \tag{2.13}$$

The unit for LET is J m^{-1}, which can also be expressed in keVμm^{-1}. L_Δ can be expressed in terms of electronic stopping power S_{el} as:

$$L_\Delta = S_{el} - \frac{dE_\Delta}{dx} \tag{2.14}$$

where dE_Δ is the mean of all kinetic energies above Δ. This definition indicates that the energy transferred locally along distance dl equals to the energy lost by the primary particle while interacting with electrons minus the energy taken away by the secondary electrons that have initial kinetic energy above Δ. If there is no energy cutoff, then we have unrestricted linear energy transfer, denoted as L_∞ or simply L, which equals to the electronic stopping power.

The definition of LET as a single quantity is only defined for monoenergetic beams. For a mixed field, such as a position in a SOPB, the LET refers to an average value over the energy spectrum of the particles [5]. There are two different ways to state this average LET value. One way is to state it as a fluence or track averaged LET ($\mathrm{LET_f}$):

$$\mathrm{LET_f} = \frac{\sum_\mathrm{i} \Phi_\mathrm{i} \mathrm{L_i}}{\sum_\mathrm{i} \Phi_\mathrm{i}} \tag{2.15}$$

and the other way is stating it as a dose averaged LET ($\mathrm{LET_d}$):

$$\mathrm{LET_d} = \frac{\sum_\mathrm{i} \mathrm{D_i} \mathrm{L_i}}{\sum_\mathrm{i} \mathrm{D_i}} \tag{2.16}$$

where L_i, Φ_i, and D_i are the LET, fluence, and dose of each individual ion i in the particle spectrum, respectively.

2.3.6 Radial Dose

To completely describe the energy deposition of heavy charged particles, one needs to characterize the track structure of the impinging ion. Unlike photons, the energy distribution of ions are marked by a localized pattern around the ion's trajectory resulting from a dense ionization process (as shown in Figure 2.4).

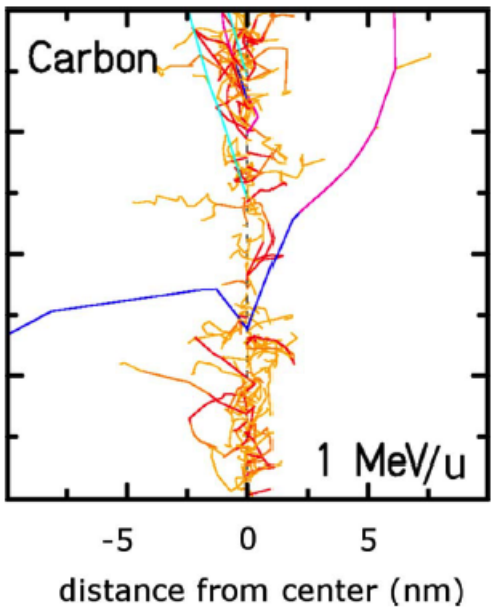

Figure 2.4: Simulation of track structure of a 1 MeV/u carbon ion. The paths of secondary electrons are represented by the colored lines. Reprinted from [17].

When heavy particles interact with matter, they release secondary electrons through Coulomb interactions with the target, which are formed densely around the primary ion track, known as the track core. These released electrons are further scattered by frequent interactions with the target. Most of the secondary electrons have very low energies or have a forward momentum, thus depositing most of their energy in the center of ion tracks. However, the more energetic electrons, that are fast enough to leave the track core, usually undergo many interactions and due to frequent scattering processes, they form a broad angular distribution around the core, known as the "penumbra". The radial dose, $D(r)$, describes the dose deposition as a function of lateral distance, r, from the path of ion. While the entire track structure can be simulated using detailed Monte Carlo simulation of each ionization event [18], to simplify the process and predict the overall shape of the dose distribution around the ion track, amorphous track structure models have been developed [19, 20]. Both Monte Carlo simulations and analytical models show a $1/r^2$ dependence for the radial dose distribution.

2.4 Range

The range is defined as the distance the ionizing radiation travels in matter until it loses it's energy and comes to rest. The range depends on interaction processes that the particle goes through and thus varies with the type, charge and initial energy of the particle. Range can be defined in several ways and it is important to distinguish from the path length. Path length refers to the total distance the particle traverses in its trajectory, while range refers to the path length projected onto the particle's original direction. ICRU has introduced the term continuous slowing down approximation (CSDA) range in order to approximate the average path length traversed by the charged particle as it slows down to rest [11]. The CSDA range assumes continuous energy loss by the particle and that the energy loss rate at each point along the particle's track equals to the total stopping power. The CSDA range (R_{csda}) is calculated as follows:

$$R_{csda} = \int_0^{E_0} \frac{dE}{S_{tot}(E)} \tag{2.17}$$

2.5 Water Equivalent Thickness

The target material, in which ionizing particle traverses, affects how the energy is deposited from the impinging particle. Since in radiation dosimetry, water phantoms are most often used to mimic tissue, one needs to know how the energy loss differs in a different material compared to water. The term water equivalent thickness (WET) is therefore used to specify the thickness of water that causes an ion beam to lose the same amount of energy as the beam would lose in the medium of interest. The WET of a material can be calculated as follows:

$$WET = t_m \frac{S_m}{S_w} \tag{2.18}$$

where t_m is the thickness of the material, and S_m, S_w are the linear stopping powers of the material and water respectively.

2.6 Microdosimetric Quantities

Microdosimetry is the specification of energy deposition and radiation quality at microscopic scales, such as the cell nucleus. This specification allows to overcome the

inadequacies of macroscopic quantities dose and LET in describing the stochastic nature of energy deposition and radiation quality at microscopic scales [21]. The two microdosimetric quantities that relate to macroscopic quantities dose and LET, are lineal energy and specific energy, respectively.

2.6.1 Lineal Energy

Lineal energy y is a stochastic quantity defined as the quotient of ϵ, which is the energy imparted in a volume by a single deposition event, by l, which is the mean chord length of that volume:

$$y = \frac{\epsilon}{l} \tag{2.19}$$

The unit for lineal energy is J m^{-1}, which can also be expressed in keVμm^{-1}.
When considering lineal energy, the probability distribution function of y, $F(y)$ is often used, which is the probability that the y due to a single energy deposition event is equal to or less than y. The probability density of y, $f(y)$ is defined as:

$$f(y) = \frac{dF(y)}{dy} \tag{2.20}$$

The expectation value of the lineal energy distribution is a non-stochastic quantitiy and is called a frequency-mean lineal energy, $\bar{y}_F$, and is obtained as follows:

$$\bar{y}_F = \int_0^\infty y \cdot f(y) dy \tag{2.21}$$

Furthermore, the absorbed dose distribution $D(y)$ with respect to a lineal energy distribution is also often considered. The expectation value of the absorbed dose distribution with a lineal energy is another non-stochastic quantity called dose-mean lineal energy, $\bar{y}_D$, and is obtained as follows:

$$\bar{y}_D = \int_0^\infty y \cdot D(y) dy = \frac{1}{y_F} \int_0^\infty y^2 \cdot f(y) dy \tag{2.22}$$

2.6.2 Specific Energy

Specific energy, z, is defined as the the quotient of ϵ by m, where ϵ is the energy imparted by ionizing radiation in a volume element having mass m:

$$z = \frac{\epsilon}{m} \tag{2.23}$$

The unit for specific energy is J kg^{-1}. The mean value of specific energy, $\bar{z}$ in the limiting case of infinitesimal m is equal to the absorbed dose:

$$D = \lim_{m \to 0} \bar{z} \tag{2.24}$$

Similar to y, it is useful to consider the probability distribution function of z, $F(z)$. That is the probability that z is equal to or less than z. The probability density of z, $f(z)$ is defined as:

$$f(z) = \frac{dF(z)}{dz} \tag{2.25}$$

For a single energy deposition event, the probability distribution function, $F_s(z)$, is used, which is the conditional probability that specific energy less than or equal to z due to only one event is deposited. Therefore, the associated probability density function, $f_s(z)$, is defined as:

$$f_s(z) = \frac{dF_s(z)}{dz} \tag{2.26}$$

Again, similar to y, the non-stochastic quantity frequency-mean specific energy per event is defined as:

$$\bar{z}_{sF} = \int_0^\infty z \cdot f_s(z) dz \tag{2.27}$$

and the non-stochastic quantity dose-mean specific energy per event as:

$$\bar{z}_{sF} = \int_0^\infty z \cdot D_s(z) dz \tag{2.28}$$

where, $D_s(z)$ is the absorbed dose distribution with respect to a z distribution of a single event.

2.7 Stochastic Energy Deposition of Heavy Charged Particles

The energy loss process of ionizing radiation is a stochastic process, which can cause large fluctuations in the amount of energy deposited by the particle traversing the target material. To describe this stochastic process the term straggling is used, which refers to distribution of energy loss about a mean value. The thinner the thickness of the target material, the fewer number of interactions, thus making the fluctuation larger. Conversely, as the target becomes thicker, more interactions occur and straggling becomes

lower, therefore stopping power of ions with same charge and kinetic energy becomes close to the mean quantity. Energy loss straggling calculation is quite complex as it depends on variation of the charge state of the ion as it traverses matter. Furthermore, there are not many experimental studies of straggling that question the accuracy of many different theories describing the straggling. In this thesis, the theories used by CERN in GEANT4 implementation [22] have been used and will be discussed here. In general, energy loss straggling is caused by two sources of variations: the number of low energy transfer collisions and the actual energy loss in each collision. The number of low energy transfer collisions, N_{col}^{Δ}, can be estimated as follows:

$$N_{col}^{\Delta} = 153.4 \frac{z^2}{\beta^2} \frac{Z}{IA} \rho \delta x \tag{2.29}$$

where z is the charge of the impinging particle, Z and A the atomic number and atomic weight of the target material respectively, ρ the density of the material, δx the material thickness, and I is the mean excitation potential of the target material.

If $N_{col}^{\Delta} < 50$, the number of low energy transfer collisions is considered small and thus a detailed atomic structure description is needed. In GEANT4 the Urban Model is used to describe this scenario which can be found in [22]. For large number of collisions ($N_{col}^{\Delta} \geq 50$) 3 different models are used to describe the energy loss straggling and have been used in this thesis with implementation in the Libamtrack software [Section 3.2.1.4]. The significance parameter κ is defined to distinguish which of the models to be used and is defined as :

$$\kappa = \frac{N_{col}^{\Delta} \cdot I}{E_{max}} \tag{2.30}$$

where E_{max} is the maximum energy that can be transferred in a single collision with an atomic electron:

$$E_{max} = \frac{2 m_e \beta^2 \gamma^2}{1 + 2\gamma m_e / m_x + (m_e/m_x)^2} \tag{2.31}$$

where $\gamma = E/m_x$, E is the kinetic energy, m_x is the mass of the incident particle, and $\beta^2 = 1 - \frac{1}{\gamma^2}$.

Depending on the value of κ, three different models for energy loss straggling are used:

1. Landau Theory : $\kappa \leq 0.01$
   The Landau theory is based on two assumptions. First is that the typical energy

loss in a collision is small compared to E_{max} (this assumption is not required by Vavilov theory), and second that the typical energy loss is large compared to the binding energy of the tightly bound electrons in the absorber (if this is not the case, a more sophisticated model is used, such as the Urban model implemented in Geant4, see [22]). In this case the energy loss in the target material with thickness δx can be estimated by the universal Landau probability distribution function [23]:

$$f(\epsilon, \delta x) = \frac{1}{\xi}\phi(\lambda) \tag{2.32}$$

where ξ is the mean energy loss and equals to $N_{col}^{\Delta} \cdot I$.
As the Landau distribution has a very large tail that does not decrease quite early as it goes to infinity, the mean value is infinite. To overcome this limitation, a limit (λ_{max}) has to be introduced to cut the values larger than that from being sampled.

2. Vavilov Theory : $0.01 < \kappa < 10$
   Vavilov theory [24] provides a more accurate energy loss straggling distribution for larger energy losses by introducing a kinematic limit on E_{max}, instead of using $E_{max} = \infty$. As mentioned before, the Vavilov theory also eliminates the restriction of small energy losses from the Landau theory. The Vavilov distribution is given by:

$$f(\epsilon, \delta x) = \frac{1}{\xi}\phi_v(\lambda_v, \kappa, \beta^2) \tag{2.33}$$

   The Vavilov parameter λ_v is related to the Landau parameter, λ_L by the relationship

$$\lambda_L = \frac{\lambda_v}{\kappa} - ln\kappa \tag{2.34}$$

   It can be shown as κ approaches 0, Vavilov distribution approaches the Landau distribution and that for $\kappa \leq 0.01$, the two distributions are almost identical. For $\kappa \geq 10$ the Vavilov distribution takes the form of Gaussian distribution (see below).

3. Gaussian Theory: $\kappa \geq 10$
   As the mean energy loss in the target material becomes larger than than E_{max}, the energy loss distribution takes a Gaussian form and the Vavilov distribution can be replaced with a Gaussian distribution:

$$f(\epsilon, \delta x) \approx \frac{1}{\xi\sqrt{\frac{2\pi}{\kappa}(1-\frac{\beta^2}{2})}} \exp\left[\frac{(\epsilon-\bar{\epsilon})^2}{2}\frac{\kappa}{\xi^2(1-\beta^2/2)}\right] \tag{2.35}$$

with mean $\bar{\epsilon}$ and variance $\sigma^2 = \xi E_{max}(1-\frac{\beta^2}{2})$

Figure 2.5 shows an example of the three different probability distributions discussed as calculated from the Libamtrack software [Section 3.2.1.4].

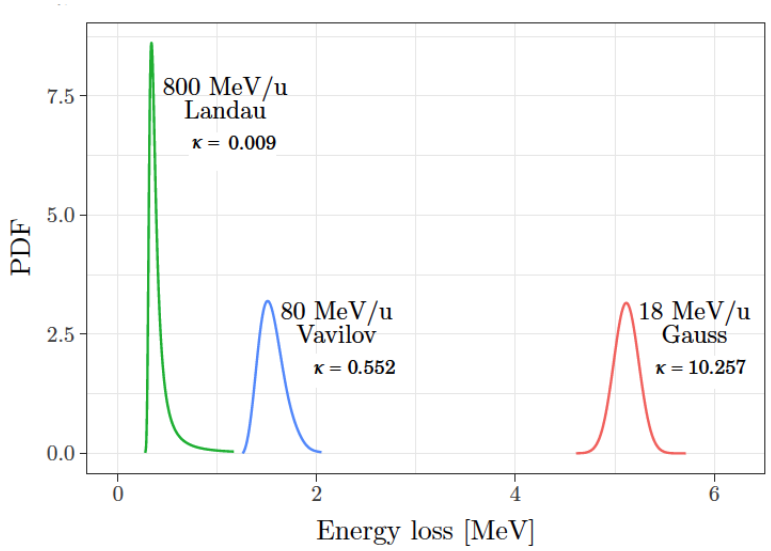

Figure 2.5: Energy loss distributions for carbon ions passing through a water slab of 50 μm for three different energies as calculated by the Libamtrack software [Section 3.2.1.4].

2.8 Relative Biological Effectiveness

Compared to photons, higher LET radiation such as ions are shown experimentally to be more biologically effective when the same absorbed dose is applied. This feature can be quantified using the term relative biological effectiveness (RBE) which is defined as the the ratio of a reference photon dose (such a 250 kV x-rays or Cobalt 60) and the ion dose that render the same biological effect:

$$RBE = \left.\frac{D_{photon}}{D_{ion}}\right|_{isoeffect} \tag{2.36}$$

In treatment planning, the dose prescribed is usually given as the biological dose to reflect the biological effect which is the product of RBE and the absorbed dose:

$$D_{bio} = RBE.D_{phys} \tag{2.37}$$

RBE is a complex quantity and depends on physical parameters and biological factors of the irradiated system including the ion type, the LET of the radiation, dose, dose rate, the biological endpoint, the cell and tissue type, the detection method used, and other intrinsic biological factors. Therefore, the RBE can differ significantly throughout the irradiated volume which should be taken into consideration during treatment planning. For protons a constant RBE of 1.1 is used [25], however for heavier ions such as Helium and Carbon, the RBE varies drastically due to high variation in their LET and therefore more sophisticated models [Section 2.10] are used to estimate their RBE.
Figure 2.7 shows how RBE varies with LET and particle type for V79 hamsters cells [26]. As can be seen from this figure, the RBE values increase with increasing LET until it reaches a peak at around 100-200 keV/μm. After reaching the peak, the RBE values decrease with increasing LET.

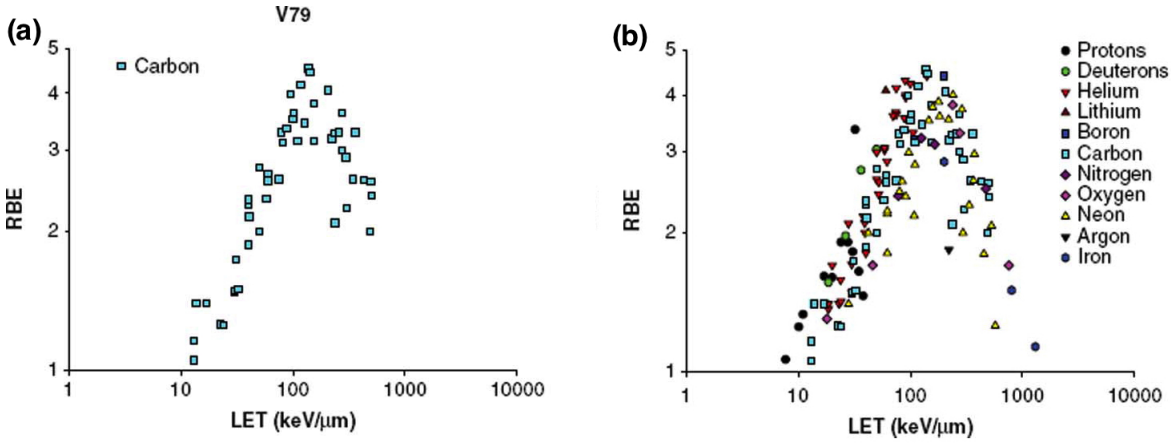

Figure 2.6: Dependency of RBE on LET and ion type for V79 hamster cells. (a) RBE values of carbon ions obtained from 8 different experimental data plotted as function of LET. (b) RBE values of different ions obtained from 11 experimental data plotted as a function of LET. Image reprinted from [26]

The main reason for the enhanced RBE of heavy ions as compared to photons lies in the way they deposit energy on a microscopic scale. As stated previously, heavy ions release a large number of low energy secondary electrons, with most depositing their

energies within a small radius around the primary track (around 156-0.6 μm for 100-1 MeV/u carbon ions). In contrast, the secondary electrons released by photons deposit their energies over large distances from the primary source (with residual range around 1-3 cm). For carbon ions, the maximum track radius decreases with decreasing kinetic energy and thus increasing LET, resulting in the local dose around the ion track to increase strongly towards the Bragg Peak or the distal edge of the SOBP. This increase in the local absorbed dose causes a higher density of direct radiation damage, such as double strand DNA breaks (DSBs). The higher localization of DNA damage (complex DNA damage) has been correlated to lower cell survival probability, and therefore explaining the RBE increase for carbon ions as compared to photons.

2.9 Cell Survival

Cell death is considered as the main biological endpoint to characterize the effect of ionizing radiation and is the main aim for radiation therapy. Use of cell survival curves is the most common way to assess the biological effects of photons and heavy ions. The cell survival curve indicates the fraction of surviving cells as a function of absorbed dose. Figure 2.7 shows a graphical illustration of cell survival curves for photons and carbon ions and indicate how RBE is obtained from these curves. In the standard cell survival protocol [27], cell proliferation is analyzed around one to two weeks after irradiation, and if they have formed a colony (with more than 50 daughter cells) they are counted as survivors. As can be seen from Figure 2.5, at lower doses, most of the DNA damages are repaired, and therefore higher percentage of cells survive. As the dose increases, the survival curve bends downwards over a region of several Grays (referred to the shoulder of the curve), and becomes linear at higher doses. Furthermore, the survival curve becomes more linear with increasing LET and the shoulder region disappears. Different models have been developed in order to predict the cell survival S. The most common model is the linear-quadratic (LQ) model [27] which describes the cell survival S as follows:

$$S(D) = \exp(-\alpha D - \beta D^2) \tag{2.38}$$

where D is the absorbed dose, and α and β are parameters that are experimentally determined and are specific to the tissue. In clinical studies, usually, the parameters are not determined separately, and instead are expressed as an α/β ratio. The α/β ratio determines the shape of the shoulder of the survival curve, and is often used in

conventional radiation therapy as it represents the intrinsic radiosensitivity of the cells.

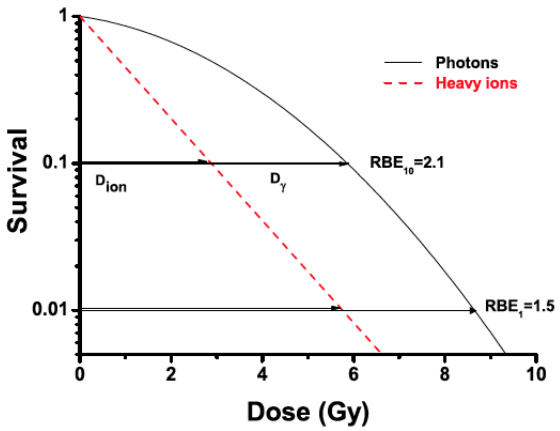

Figure 2.7: Graphical illustration of cell survival curves of cells irradiated with photons (black curve) and with heavy ions (dashed red line). The survival curve becomes more linear with increasing LET. RBE can be determined from these survival curves when the same absorbed dose results in the same survival fraction. RBE for cell survival at 10% and 1% level for a typical carbon ion irradiation is shown. Reprinted from [4].

2.10 Biophysical Modeling

It is crucial for treatment planning with carbon ions to take into account the increased RBE relative to photons and the differential RBE behavior along the depth dose profile. As the RBE of carbon ions depends on complex physical and biological parameters, biophysical modeling is used to describe the RBE and incorporate it into treatment planning. The most common biophysical models used currently in treatment planning are described as below.

2.10.1 Local Effect Model (LEM)

The local effect model (LEM) is one of the main biophysical models for carbon therapy and is currently implemented at Heidelberg Ion Therapy Center [28]. LEM uses the track structure of ions to calculate the RBE [29–31]. One of the basic assumptions of LEM is that the biological effect, such as cell death, is caused by a single lethal event generated by the local dose deposition of the ion and that the probability of lethal events depends only on the amount of the local dose and is independent of the source

of radiation, ie. whether it is coming from photons or ions. Thus the RBE difference between ions and photons only arises from the the dose distribution on the microscopic level. As a result of this assumption, the radiobiological experiments performed with photons can be used to derive the biological effects of ions. Thus, knowing the α and β parameters of the linear-quadratic model for photons for the same tumor or other biological endpoints, the RBE of the ion and its fragments can be calculated given the physical parameters. While the LQ model is incorporated in LEM, LEM sets a threshold D_t, after which the survival curve no longer follows a shouldered form and transforms into a purely exponential part to account for the fact that at high doses a pure LQ model overestimates the radiation effect. To calculate the local dose, an amorphous track structure is used which assumes that the track center has a constant dose up to a minimum radial dose around the center, and for the outer part (for radii larger than the minimum radius) the dose has $1/r^2$ dependency. When the radius is larger than a maximum radius the dose is 0. The LEM calculation is performed for the entire particle spectrum including nuclear fragments, and repeated for statistical accuracy. There are currently 4 different versions of LEM [32–35] with the later versions incorporating DNA damage distribution and other factors to compensate for deviations in RBE predictions.

2.10.2 Modified Microdosimetric Kinetic Model (MMKM)

Another clinically applied biophysical model is the modified Microdosimetric Kinetic Model (MMKM), and is currently used in beam scanning system at HIMAC in Japan at the National Institute of Radiological Sciences (NIRS) [36]. MMKM is a modified version of the original Microdosimetric Kinetic Model (MKM), proposed by Hawkins [37] which is based on microdosimetric principals. In this model the cell nucleus is divided into small volumes called "domains". The number of lethal lesions in the domains is assumed to have a linear-quadratic dependency on the stochastic microdosimetric variable specific energy, z. MKM assumes that the RBE differences are due to the different distributions of specific energy, and that the damage mechanism is independent of radiation type. The deposition events can cause two types of lesions: lethal lesions and sublethal lesions. Sublethal lesions can either spontaneously transform to lethal lesions, interact with another sublethal lesion to create a lethal lesion, spontaneously get repaired, or remain unrepaired until time t_r after which transforms into a lethal lesion. The MKM considers cell death if one of the nuclear domains is dead, which occurs if there is a single lethal lesion in that domain. In the modified version proposed

by Kase et al. [38], the reduction of RBE due to overkill effect in a region of very high specific energy is taken into account by using a corrected dose mean specific energy of the domain to calculate the number of lethal events.

It should be noted that LEM and MMKM are conceptually very similar in that they both use the cell nucleus as the target for lethal events induced by radiation, they both divide the cell nucleus into sub-volumes for the local dosimetric calculations, and they both use the photon cell survival curve to determine the biological effect of each sub-volume [39]. The main difference between the two are the size of the sub-volume considered and the way the dose-effects are determined. MMKM uses the stochastic microdosimetric energy deposition in micron-sized domains, while the LEM uses the macroscopic quantities in terms of local dose in infinitesimally small volumes [39].

Chapter 3

Material and Methods

3.1 Experimental Tools

The experimental methods of this thesis consist of tools to measure the quantities established in the new "Cell Dose" model for characterization of energy deposition by heavy charged particles in the cell nucleus, benchmark the theoretical framework, and showcase its application in radiobiological studies. Current dosimetric measurements used for radiotherapy applications quantify energy deposition in the millimeter scale, which is suitable to obtain macroscopic quantities such as absorbed dose and LET in target volumes at a scale appropriate for tumor size and organs at risk. Such macroscopic measurements are not suitable for a target size in the microscopic scale such as the cell nucleus. Therefore, the dosimetric system to be used for measurement of "Cell Dose" quantities needs to be capable of quantifying energy deposition in the microscopic scale. Another property needed for "Cell Dose" measurements is the ability to be used in a hybrid system such that it could be combined with a biological compartment to have the capability to directly correlate physical properties to biological outcome. Thus, in addition to detecting and measuring radiation, the system should be capable of incorporating a cell imaging technique to image the cells for measurements and monitor the radiation induced biological response, which can be correlated directly to physical parameters. Furthermore, the system needs to be able to detect the majority of the primary particles and their fragments relevant for radiotherapy, ranging from very low LET to high LET and at relevant therapeutic energies (up to 400 MeV/u for carbon ion therapy).

To fulfill all the requirements mentioned for measurements in the "Cell Dose" framework, fluorescent nuclear track detectors (FNTDs) were chosen as the model detectors.

Irradiation of FNTDs in combination with cells and confocal microscopy, to readout both the physical and biological properties, are used as the complete system for this study. FNTDs have the unique ability to detect particles with LETs (in water) ranging from 0.5 keV/μm to 1800 keV/μm [40], are biocompatible, can be used as a substrate for cells [41], and can be directly imaged after irradiation with cell coatings to monitor DNA damage response (DDR) [42]. FNTDs can detect particles in microscopic scales and smaller with an efficiency close to 100% and can provide physical information (discussed below) about different particle tracks in a mixed multi-ion radiation field. Concurrent measurement of radiation and cellular response visualization have been performed mainly with microbeam systems [43], in which a narrow focused beam with micrometer or submicrometer diameter is used for precise irradiation of sub-cellular structures to induce damage and visualized with integrated fluorescence microscopy to image and to investigate the damage mechanism. While such systems provide a suitable tool for direct correlation of physical properties to biological response, they can only deliver low energy radiation (less than 20 MeV/u), thus limiting their application for ion therapy. Moreover, microbeam systems are extremely sophisticated with expensive infrastructure that is technically challenging to construct and operate, which further restricts their accessibility. FNTDs, therefore, are preferred over microbeam systems as they are much simpler, cheaper and can be used with higher energy ions in therapeutic range. FNTDs are also preferred over conventional microdosimetry detectors, as they can be easily used with cells and provide individual track information needed to obtain the quantities discussed in the model. Furthermore, FNTDs are also preferred over other similar track detectors such plastic nuclear track detectors (PNTDs), due to their higher spatial resolution, and wider LET range [44]. The following subsection, describes in detail the experiments and methods used with FNTDs for "Cell Dose" measurement.

3.1.1 Fluorescent Nuclear Track Detectors

Detecting charged particle radiation is crucial in monitoring radiation effects and safety, treatment planning, and experimental measurements. Current standard radiation detectors and dosimeters such as ionizing chambers, while having great advantages in measurement accuracy, are not designed to give a complete and detailed information about the particle tracks. To provide such information, solid state nuclear track detectors have been introduced to complement a wide range of detectors for various purposes. These detectors are made of solid materials (such plastic, glass, or crystal, etc.) and allow measurements of properties of nuclear particles after exposure (neutrons and

charged particles) by microscopic examination. When nuclear particles pass through these structures, they leave a so called track of damage sites that have different properties from the bulk of the material at a microscopic and nanoscale levels, which can provide detailed information about individual particles such as fluence, charge, mass, energy deposition and the particle's trajectory. Traditional solid state nuclear track detectors, such as plastic nuclear track detector (PNTDs) [45], rely on etching. When such nuclear particles pass through these detectors they leave a track in the detector which is etched faster than the rest of the solid state. Other changes in the solid's property, such as fluorescence properties can also be used to store track information and be examined with a microscope, which is the property of Fluorescent Nuclear Track Detectors (FNTDs), as used in thesis and subject of this section.

The FNTDs used in this thesis were all manufactured by Landauer Inc. (Stillwater, Oklahoma, USA). These detectors consist of single crystals of Aluminum Oxide doped with Carbon and Magnesium ($Al_2O_3 : C, Mg$) [46]. The crystals contain a high concentration of aggregate defects known as complex color centers that, after exposure to ionizing radiation, trap the secondary electrons produced by the traversing ion and undergo radiochromatic transformation. The transformed color centers show fast (lifetime of 75 ± 5 ns) fluorescence at 750 nm when excited with wavelengths of around 620 nm. This can be captured with Confocal Laser Scanning Microscopy, as performed in the work of this thesis, allowing for detection of single ion tracks, assessment of their energy loss and 3D reconstruction of the tracks. In this thesis, FNTDs were used in 2 different forms. The first forms were FNTDs cut in a rectangular shape along the optical z-axis with dimensions of (4 x 8 x 0.5 mm^3). The FNTDs were polished on one side for optical quality. The other set of FNTDs were cut in shape of circular wafers with diameter of of 25 mm and thickness of 112 μm. These FNTDs are polished on both sides and can be used as cover slips for cells and be imaged from either side. Figure 3.1 illustrates the two FNTD forms used in this thesis.

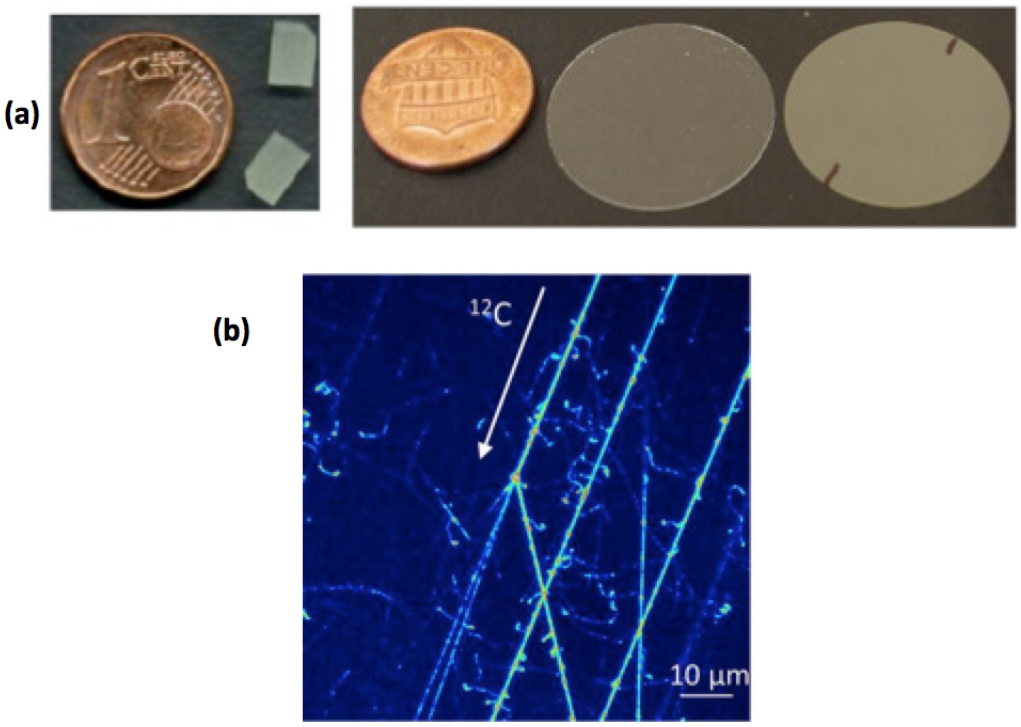

Figure 3.1: FNTDs in different forms used in this thesis next to a coin for size comparison (a). On the left two FNTDs cut in rectangular form (4 x 8 x 0.5 mm^3), polished on one side next to a 1 cent coin. On the right two circular FNTDs (diameter: 25 mm; thickness: 112 μm) polished on both sides next to a penny. The trajectory of carbon ion tracks imaged from an FNTD are shown on the bottom (b).

3.1.1.1 Crystal Structure and Photoluminescence

FNTDs are made of α-Al_2O_3 crystals which have a lattice structure in which O^{2-} ions form a hexagonal sublattice with Al^{3+} ions occupying two out of every three octahedral interstices [46, 47] as shown in Figure 3.2. In order to store dosimetric information, point defects need to be created in the crystal in the form of oxygen vacancies (F-centers). These defects are often called color centers since they become colored after photon absorption. To create such oxygen vacancies, the crystals are grown in a highly reducing atmosphere with a low oxygen partial pressure. If two electrons occupy the oxygen vacancy, a neutral F center is formed, while occupancy by a single electron forms a positively charged F^+ center. Doping the aluminum oxide with carbon significantly increases the F^+ center concentration. The F and F^+ centers trap holes and electrons,

respectively, that are generated by irradiation. Furthermore, doping the crystals with magnesium creates an even higher concentration of F^+ centers as they compensate for the charge compensation of Mg^{2+} ions. Additionally, Mg^{2+} ions can surround two F^+ centers that are in close proximity, forming a $F_2^{2+}(2Mg)$ color center. The different color centers exhibit different excitation and emission spectra. Figure 3.2 illustrates the crystal structure of FNTD with its color center aggregates.

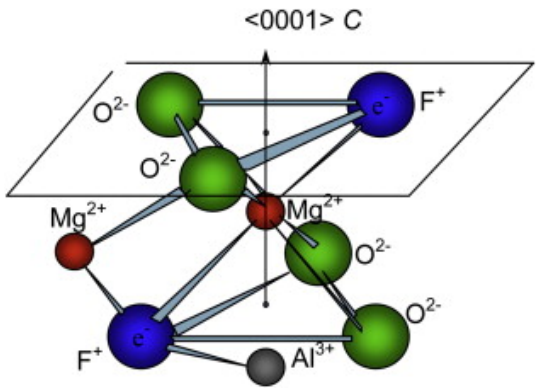

Figure 3.2: Crystal structure of $Al_2O_3 : C, Mg$ with $F_2^{2+}(2Mg)$ color center. Reprinted from [46]

The physics of FNTDs can be described as radio-photoluminescence. That is radiation, through radiochromic transformation, converts existing color centers to new stable luminescent centers, which can be discovered with light through an excitation-emission process. Due to their several unique properties, $F_2^{2+}(2Mg)$ color centers are what make FNTDs particularly useful in radiation detection. These color centers, in their untransformed form before irradiation, have one absorption band centered at 435 nm (in the blue) and emit 520 nm photons, which are responsible for the green coloration of the crystals. When heavy charged particles penetrate through the FNTD, they release secondary electrons along their tracks which create numerous electron-hole pairs in the crystal. The $F_2^{2+}(2Mg)$ centers capture these free electrons and transform into a three-electron state, forming $F_2^{+}(2Mg)$ centers. The new transformed color centers have an excitation band centered at 620 nm with emission at 750 nm with a high quantum yield. They have a very short lifetime of 75 ± 5 ns, which make them suitable for fast readout with scanning microscopes. Figure 3.3 shows this process in a schematic form. Furthermore, they are both thermally and optically stable, which enables multiple readouts to improve the signal-to-noise ratio [46, 47].

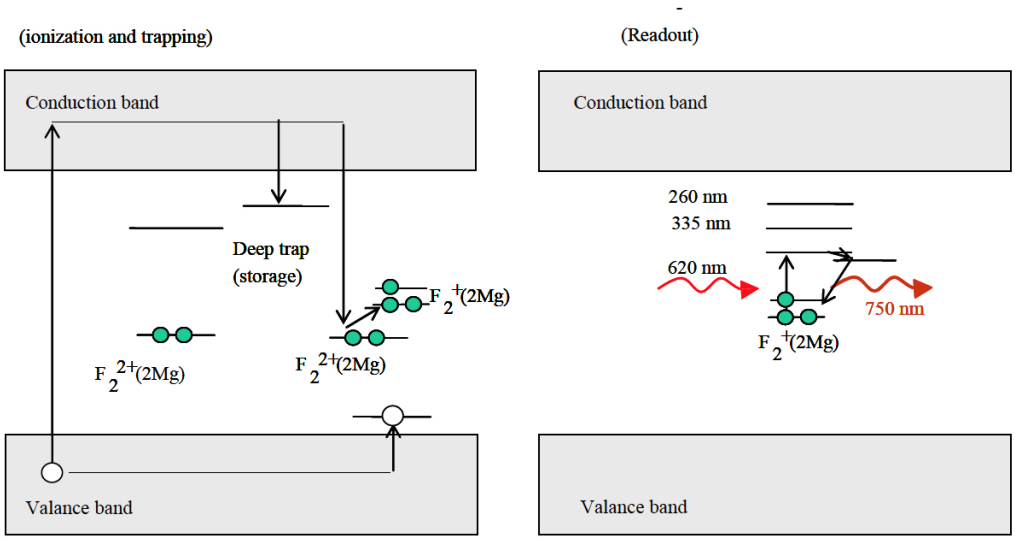

Figure 3.3: Radiochromic transformation of a $F_2^{2+}(2Mg)$ color center into a $F_2^{+}(2Mg)$ defect (left) and fluorescent behavior of the transformed color center (right), reprinted from [46]

3.1.2 Microscopy

Two confocal laser scanning microscopes (CSLMs) were used to acquire cell and FNTD images. CSLMs (illustrated in Figure 3.4) use a spatial pinhole in front of a sensitive detector to filter out-of-focus light in forming an image, resulting in an enhanced optical resolution [48]. While this filtering increases resolution, it also causes a decrease in the signal intensity. To compensate for this effect, long exposure time is needed, and often a photomultiplier tube (PMT) or an avalanche photodiode is used to transform the light signals into electric signals. In CSLM, the specimen is imaged by scanning the focused beam over a rectangular raster, since the illumination is performed point by point. Oscillating mirrors are used to scan the beam across the specimen in the horizontal plane by tilting the beam in the x and y direction in a raster fashion. The speed of the scanning can be adjusted, as a slower scan results in a better signal-to-noise ratio for better contrast. Likewise, multiple rescans can be performed. CSLMs also allow for optical sectioning of the specimen imaged, a process in which multiple 2D images of the sample are captured at different depths (forming a so-called "z-stack") to construct the sample in 3D. A main beam splitter (MBS), usually a dichroic mirror, is used to reflect the excited light onto the sample, thus allowing the emitted light from the specimen (which has a lower frequency than the excitation frequency) to go through and reach the sensitive detector.

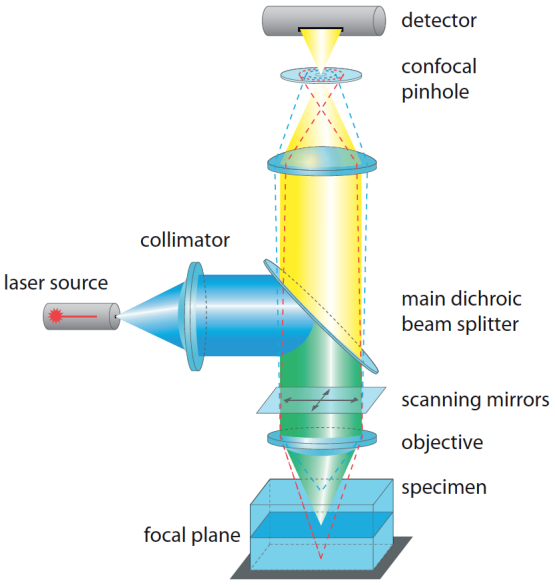

Figure 3.4: Components of confocal laser scanning microscopes. Reprinted from [49]

To achieve a point-like illumination, an additional pinhole is placed in a conjugate plane to the emission pinhole below the excitation source. To describe the 3D intensity distribution of a single point in the image space, which due to demagnification of the optical system, appears blurred or spread, an intensity point spread function (PSF) is used. The PSF of a confocal microscope, assuming an infinitesimally small pinhole, is given by:

$$\mathrm{PSF}_{conf} = \mathrm{PSF}_{ill} \times \mathrm{PSF}_{det} \tag{3.1}$$

Where, PSF_{conf}, PSF_{ill} and PSF_{det} represent the point spread functions for the confocal imaging, the illumination and detection paths, respectively. The properties of the point spread function in both the imaging plane and the axial direction determine the spatial resolution of the microscope. The resolution of an optical microscope is defined as the shortest distance between two small objects on a specimen that can still be observed as separate entities. The lateral and axial resolutions of the microscope are related to the numerical aperture (NA) of the microscope and wavelength of light, λ, that is used for imaging the specimen. NA is the measure of the microscope's objective ability to gather light and is defined as follows:

$$NA = n \sin \alpha \tag{3.2}$$

where n is the refractive index, and α is the half-angle of the objective's aperture. There are several equations for the resolution of a microscope, but the most famous one is the formula introduced by Ernst Abbe which defines the resolution as follows for lateral (xy) and axial(z) resolutions:

$$Resolution_{xy} = \frac{\lambda}{2n \sin \alpha} = \frac{\lambda}{2NA} \tag{3.3}$$

and

$$Resolution_{z} = \frac{2\lambda}{(n \sin \alpha)^2} = \frac{2\lambda}{(NA)^2} \tag{3.4}$$

In addition to confocal microscopy, widefield microscopy was also used to acquire cell images for one of the experiments. In widefield microscopy, the entire specimen is exposed to the light source either from above (in an inverted configuration), or below (in a standard upright configuration). The resulting image is viewed either by the observer or a camera. Widefield microscopes are usually less complex than confocal microscopes consisting of white and fluorescence light source and can image larger fields. However, it has a decreased resolution compared to confocal microscopy, and a higher signal to noise ratio.

3.1.2.1 Zeiss LSM710, Confocor 3

The ZEISS LSM 710 ConfoCor 3 (Carl Zeiss AG, Germany), which is a CSLM provided by DKFZ's core facility, was used in this study to readout some of the FNTD samples and image the cells used. This microscope is equipped with seven different lasers ranging from 405 nm to 633 nm, a motorized scanning stage (DC 120 x 100), a PIEZO objective focus with a PIEZO stage, several detectors, MBSs, different filters, two phtomultipliers (PMTs), one transmission photomultiplier (T-PMT) and two avalanche-photodiodes (APDs) [49]. Table 3.1 lists the important components of this microscope and Figure 3.4 illustrates a general schematic of the system.

Table 3.1: Components of ZEISS LSM 710 ConfoCor 3 microscope

Feature	Components available
Excitation source	diode laser 405 nm
	Ar laser 458/488/514 nm
	HeNe laser 633 nm
	Mercury lamp
Objective	Plan Apochromat 63x / 1.4 Oil
	Plan Neofluar 40x / 1.3 Oil
	C-Apochromat 10x, 20x, 63x dry
Main dichroic beam splitter (MBS)	488/562/633
	405
	488
	458/562
Detectors	2 APDs operating in Geiger (photon counting)mode
	2 PMTs operating in current mode
	1 T-MPT
Longpass filters	LP 655
	LP 590
	LP 397
Other	Z motor
	Piezo Objective focus
	Z-Piezo stage
	2 galvanometric scanners

The 633 nm helium-neon laser is used for excitation of radiation induced F_2^{2+} color centers, while the 405 nm diode laser and 488 nm Ar-laser are used to excite the markers for cell nuclei and DSBs, respectively. Scanning mirrors attached to piezoelectric crystals (scanning stage DC 120x100) are used to deflect the beam, which in turn is focused onto the the specimen by one of the objectives. A motorized Piezo driven stage, with a maximum travel range of 250 μm and a 5 nm resolution, is used to adjust the focal point and allows for 3D imaging. The different main beam splitters and longpass emission filters are used to separate the fluorescence signals emitted from the sample from the reflected excitation light. The pinhole in front of the detector reduces the fluorescent signal originating from images planes that are further from the focal plane,

thus reducing the detection depth. While reducing the pinhole size results in decreasing the amount of unwanted fluorescence signal for a better depth discrimination, it also causes a decrease in the signal intensity. Setting the pinhole size to 1 Airy unit (43.6 μm) gives an optimized trade-off between lateral resolution and intensity. The two fiber-coupled, actively quenched APDs, operating in Geiger (photon counting) mode, and PMTs, operating in current modes, are used to detect the fluorescence signal emitted the samples. The ADPs are used to detect FNTD fluorescence signals, while PMTs are used for the cell layer, because the ADPs have a much higher quantum efficiency for the red light than the PMTs. Additionally, T-PMTs are used to detect laser light transmitted by the sample (for both FNTDs and cells). The microscope is controlled by the interface ZEISS Efficient Navigation (ZEN) software (different versions). The important control parameters, which were set by the ZEN software, are listed in Table 3.2.

Table 3.2: Important control parameters for Zeiss 710 Confocor 3

Parameter	Description
Relative laser power p (%)	Relative power of excitation laser during image readout
number of rescans R	Averaging or summation over images (by line or image)
dwell time τ (μs)	The duration in which the scanned beam remain on a single pixel in the image
frame size	lateral (x, y) image dimension in pixels
Pixel size (μm)	Size of a single scan position
Step size Δz (μm)	axial distance between two images in a z-stack
Pinhole diameter (AU)	The diameter was chosen as 1 Airy unit (AU)=43.6 μm as a compromise for intensity efficiency and depth discrimination

3.1.2.2 Portable Fluorescence Confocal Laser-Scanning Microscope (FCLSM) for Beamline Imaging

The irradiation samples performed as part of the collaboration project with MD Anderson Colleagues (Experiment SINF described in next chapter) were read out using a custom made open-frame portable fluorescent confocal laser-scanning microscope, developed by the colleagues at MDAnderson [50]. This microscope is unique as it can be placed directly in the beamline for direct measurements of cell response after irradiation and allow for a better registration of FNTD and cell positions, as FNTDS/cells don't

have to be moved. The main components and beam path of this beamline FCLSM system, along with positioning of FNTD cell chamber, are shown in diagrammatic form in Figure 3.5.

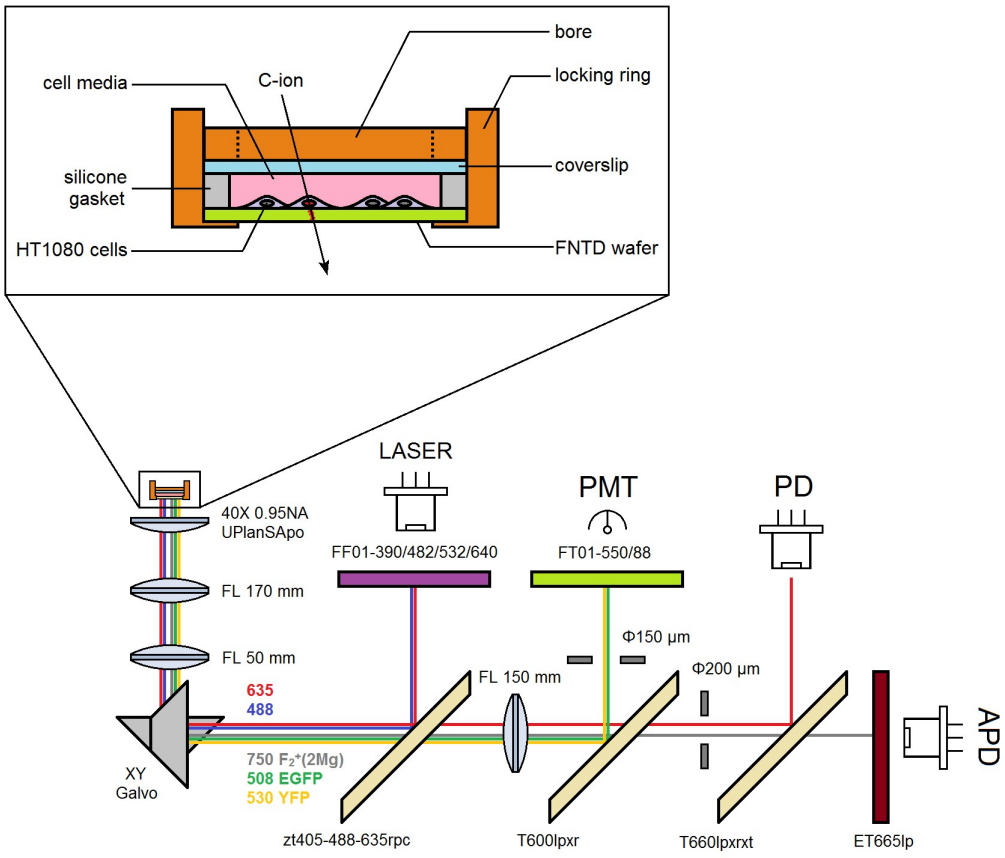

Figure 3.5: Components of beamline pCLSM. Reprinted from [51]

For excitation of samples, this microscope is equipped with three laser diodes (405, 488, and 635 nm) that are combined with a fiber-coupled laser combiner (SpectraTec X, Blue Sky Research). The blue 488 nm laser is used for excitation of DDR proteins including the yellow fluorescence protein (eYFP) used in this study [Section 3.1.4.3], while the red 635 nm laser is used for excitation of the radiation-induced color centers in FNTDs. A 60x oil immersion objective (UPLSAPO60XO; NA 1.35) is placed in front of the detector to focus the excitation beam and collect fluorescence light emitted from the FNTD and DDR proteins. A pair of galvanometer mirrors are used to scan the laser beams along the focal plane (x-y direction). For scanning in the axial direction (z direction) a stepper motor stage is used. Moreover, the microscope contains three photodetectors

including an avalanche photodiode for the detection of near-infrared fluorescence from the F_2^{2+} color centers in FNTDs, a photodiode for detection of back-reflected 635 nm light, and a photomultiplier tube to detect the fluorescence light emitted from the eYFP protein. Several dichroic mirrors are used to filter fluorescence emission from excitation emission, with the addition of a 450/88 nm bandpass filter for eYFP fluorescence and 650 nm long-pass filter for FNTDs. Data-acquisition cards (National Instruments) and custom-designed in-house software written in LabVIEW are used to digitalize signals and control the system. The scanning parameters are similar to the parameters listed in Table 3.1 for the Zeiss system.

3.1.2.3 Olympus Inverted Microscope CellR

The motorized and inverted widefield microscope CellR (Olympus, Japan), provided by DKFZ's core facility, was used in one of the experiments (MN81000/MN12000 [Section 4.4]) to acquire image of the cells [52]. This microscope is equipped with a dry objective (UPlanSApo 20x/0.75), the illumination system MT20 arc burner 150W Xe/Hg, a grayscale CCD Hamamatsu Orca-ER camera, HCRed filter-set and an incubation chamber for the cells with humidified atmosphere of 37° and 5% CO_2.

3.1.3 Cell Experiment Protocols and Materials

For the benchmarking of the "Cell Dose" model, 3 cell experimental data with FNTDs were analyzed which will be discussed in the next chapter. In this section the materials and general protocols for the cell experiments will be explained.

3.1.3.1 Cell Lines

Three different cell lines were used in this thesis which are described as follows:

A431 epidermoid carcinoma cell line
A431 cell line was developed from an epidermoid carcinoma in the skin. A431 cells are commonly used in studies of cancer cell signaling pathways since they express abnormally high levels of the Epidermal Growth Factor Receptor (EGFR). They were studied in this thesis as they can grow well on FNTDS and be assessed for radiation induced apoptosis [53].

A549 human lung cancer cell line
The A549 human Non-Small-Cell-Lung-Carcinoma (NSCLC) cell line is one of the most

commonly used cell lines for study of lung cancer. The cells are made of adenocarcinomic human alveolar basal epithelial cells. The cell line was developed in 1972 by culturing cancerous tissue from a lung tumor [54]. A549 cells can grow adherently on FNTDs forming a tightly packed monolayer and thus were chosen for the hybrid experiments [41, 53, 55].

HT1080 human fibrosarcoma cell line

HT1080 is a fibrosarcoma cell line developed from a tissue biopsy. These cell are easy to be transfected with fluorescent proteins, and as they have been extensively used for DDR markers and proved viable on FNTDS, they were chosen for the hybrid experiments [50].

3.1.3.2 Cell Culture Protocols

All the cells studied in this thesis were cultured under standard conditions of humidified atmosphere in culture flasks and incubated under standard conditions of 37° and 5% CO_2 [51–53]. Cell culture was performed under sterile conditions using a laminar hood. The cells were cultured in fresh medium and supplemented with 10% fetal bovine serum and 1% penicillinestreptomycin. The media used were Roswell Park Memorial Institute 1640 medium (Biochrom AG, Berlin, Germany, Cat. No. FG 1215) for A43 cells, Dulbecco's Modified Eagle's Medium (DMEM) for A549 cells, and MEM Alpha Modified medium with 2 mM L-glutamine for the HT1080 cells. At confluence of about 80%, cells were split and seeded into new flasks. For this purpose cells were washed with PBS and trypsin was added before seeding into new flasks.

3.1.3.3 Description of Fluorescent Markers for Live-Cell Imaging

In order to visualize the cell nucleus and monitor the DNA damage induction and repair and other biological responses via live cell imaging, fluorescent markers, which are molecules such as proteins or enzymes that selectively bind to the target molecules, are used. By exciting these molecules using appropriate light sources, they will emit a light with higher wavelength which can be used to detect the target of interest. The following gives a brief description of the fluorescent markers used:

Draq5

Draq5 is a far-red emitting anthraquinone compound that intercalates in the DNA and can be used to stain the nuclei in live cells. 488 mm, 568 nm, 633 nm, and 647nm

lasers are used to excite Draq5, and 695LP, 715LP, and 780LP filters are used for the detection [56].

DEVD-NucView488,
DEVD-NucView488 is an enzyme substrate that is used in live-cell imaging for the detection of caspase-3 which is an enzyme active in cell apoptosis [57]. DEVD is the caspase-3 recognition motif which binds to the nucleus-staining fluorogenic dye NucView488.

eYFP
Yellow fluorescent protein (eYFP) is a genetic mutant of the green fluorescent protein (GFP) which was developed from the jellyfish Aequorea victoria [58]. It has a excitation peak at 514 nm and an emission peak at 527 nm and is often used for fluorescent imaging of cells. The HT1080 human fibrosarcoma cells were transfected to express eYFP tagged to 53BP1 (p53 binding protein 1). That is the 53BP1 protein which is a signaling protein in the DNA Damage Response (DDR) of cells, forming radiation induced foci (RIF), were fused to the eYFP protein in order to visualize these foci during live cell imaging and monitor RIFs.

mCherry Protein
mCherry is a bright red fluorescent protein developed from DsRed [59]. mCherry has a rapid maturation which makes it possible to obtain results soon after transfection. It is also very optically stable and resistant to photobleaching which makes it a good candidate for cell experiments. mCheery absorbs light between 540-590 nm and emits light between of 550-650 nm. A549 cells were transduced retrovirally with a construct coding for the N-terminus of 53BP1 fused to the sequence coding for fluorescent mCherry-protein and were selected with puromycin.

3.1.4 Irradiation

All irradiations were performed at the Heidelberg Ion Therapy (HIT) center. HIT is a therapeutic facility at Heidelberg University Hospital that started clinical treatment as of November 2009, and is the first combined treatment facility in Europe that offers both protons and heavier ions for radiotherapy [28]. Four types of ions, including protons, helium, carbon and oxygen are used for irradiation at HIT, with protons and carbon currently being clinically used, while helium and oxygen are being used for

experimental purposes at therapeutic energies. There are four beam lines available at HIT, including three treatment rooms and an additional room for experimental research and quality assurance (QA beam line). Three of these beam lines, including the QA beam line, are fixed horizontal lines, while one of the treatment rooms includes a carbon ion gantry that allows 360 degree rotation. The ion sources in their gaseous state (hydrogen gas for protons and carbon dioxide for carbon ions) are injected into a two-stage linear accelerator to pre-accelerate the ions (up to 12% of speed of light) and get fully ionized after passing through a carbon stripper foil. Afterwards, they get injected into a synchrotron, which allows for the ions to be accelerated to the desired energy (up to 75% of speed of light). Afterwards, through dipole and quadrupole magnets the ions are guided to the treatment rooms (or the QA room) in vacuum tubes where the beam is focused. Before entering the rooms, the beam passes through scanners and is precisely guided by raster scanning method in order to shape the field and control the intensity within. For each particle type there are 255 energies available consisting of 48-221 MeV for protons, and 89-430 MeV/u for carbon ions, corresponding to depths of 2-31 cm in water.

3.2 Computational Tools

3.2.1 Analysis Software

3.2.1.1 R

R is a statistical software with programming capabilities [60]. Most of the data analysis, such as dosimetric calculations, analysis of the intensity and trajectory information obtained from FNTDs and their extrapolation into the cell layer, were performed in R (versions 3.3.1-3.3.5). Additionally, computational simulation of the "Cell Dose" framework in this thesis was carried out with R, using its built-in statistical functions and parallel computing capabilities. Furthermore, some of the software used in this thesis, including Libamtrack, HITXML, and FNTD package, were installed as packages that can be installed and ran in R. RStudio (versions 0.98.1087-1.2.5019-6) [61] was used as an integrated development environment for R.

3.2.1.2 Matlab

Matlab (versions 9.1-9.4) [62] is another computational software with programming capabilities that was used for some parts of the data analysis. In particular the imaging

toolbox of Matlab was used for overlaying segmented cell nuclei image onto the extrapolated FNTD track information, from which the "Cell Dose" quantities were computed for the cell experiments.

3.2.1.3 Fiji

Fiji [63] is an extended distribution of ImageJ [64], which is a Java based image processing software. Fiji offers multitude of plugins for image analysis. Fiji was used to import the images of FNTD and cells obtained from the microscope for further analysis needed for "Cell Dose" measurements. Fiji has the capability to convert the microscope raw images obtained from the LSM into tagged image file format (TIFF). The FNTD package (described below) was installed as a plugin in Fiji in order to analyze the FNTD images. Furthermore, different plugins and tools in Fiji were used for image segmentation of the cell layer for "Cell Dose" calculations.

3.2.1.4 Libamtrack

Libamtrack [65] is an in-house developed software with routines used for calculation needed in heavy ion therapy and is available as a package in different platforms such as R, which was the case for this thesis. Many of the physics calculations performed in this thesis, including computation of stopping power of different particles, calculation of Landau and Vavilov distribution for energy loss straggling, range of particles in matter, RBE, and radial dose distribution were carried out using Libamtrack.

3.2.1.5 HITXML

HITXML [66] is another in-house developed software with a set of routines that was installed as a package in R. HITXML was used to create irradiation plans in a format that can be used for irradiation at HIT. HITXML was also used to create both physically and biologically optimized spread out Bragg Peak (SOBP) plans when given the dose and depths needed. Furthermore, this software was used for obtaining particle spectrum from treatment planning data that is used in HIT.

3.2.1.6 FNTD package

FNTD package [67] is an in-house written software package for the image analysis of FNTDs and obtaining pertinent information about particle tracks. The main components of this software package is written in Java programming language and uses

ImageJ/Fiji as one of its main libraries, including the MOSAIC suit for identification particle tracks [68, 69]. The FNTD package can be installed as an ImageJ/Fiji plugin or ran as a stand-alone Jar file. Additionally, an R distribution is also available which allows for the software to be ran in the R environment and provides additional tools for statistical analysis and graphical representation of the obtained data. The program requires two input files including the raw image of FNTD obtained from the microscope and an option file in a special XML format for the parameters needed for FNTD image processing and track reconstruction. The raw FNTD image needs to be provided as a 4D hyper-stack TIFF file. The first two dimension are the pixel coordinates of the 2D $x - y$ plane and the third dimension is the depth position z, which together make up a 3D "image stack". The forth dimension of the hyper-stack is the "t frame" that denotes the readout position, as image stacks can be read from multiple locations on the same FNTD. After image analysis, the information on identified ion trajectories are outputted as data tables. The details of how the ion tracks are identified and evaluated are explained in Section 3.2.2.

3.2.2 Analysis of Particle Tracks Acquired from FNTDs

The FNTD package [Section 3.2.1.6] was used for identification of ion track signature ("track spots") in each image slice of the FNTD (referred in the software as "tracking") and their assignment to ion tracks (referred in the software as "linking"). Track identification and evaluation by the FNTD package is divided into four phases: processing of the raw FNTD image, identification of "track spots", linking of track spots to different ion tracks, and evaluation of the ion tracks. Figure 4.2 shows a flow chart of this process. The parameters required for each of these four steps are contained in the XML format option file, which can be specified manually or through the graphical user interface (GUI) of the FNTD software [67]. The four steps are described as follows:

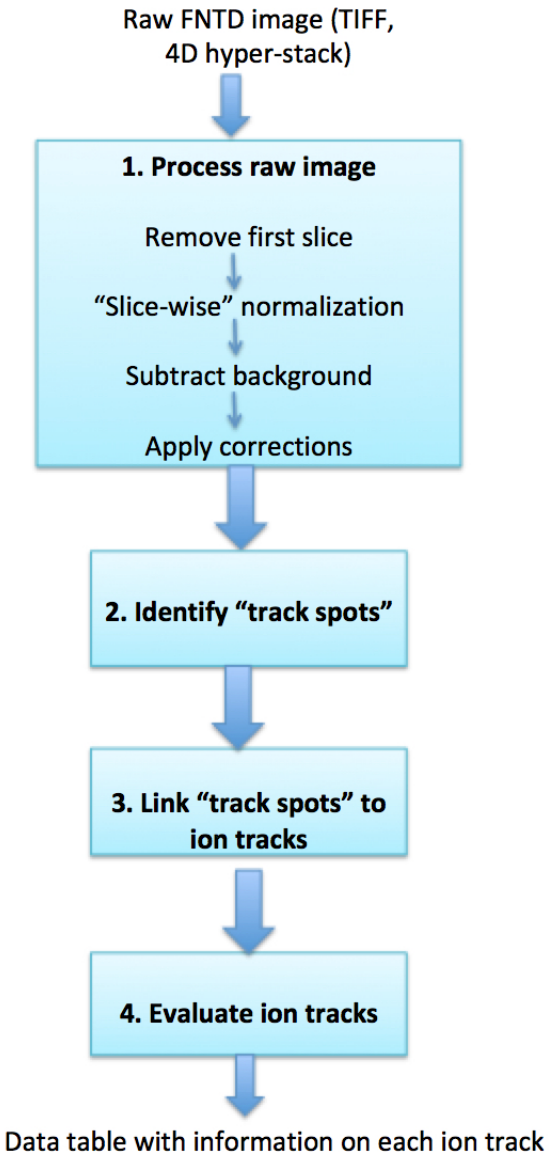

Figure 3.6: Flowchart of FNTD image processing

Step 1: Processing of the raw FNTD image

In the image processing step, usually the first slice in the image stack is removed upon request since the artifacts from the FNTD surface are excluded. The next step in this process is "slice-wise" normalization of total intensity using the intensity sum of all pixels. A reference slice can be specified in options, to which the intensity sum of each slice is normalized to. If a reference slice is not specified, then the average over all slices is used. This normalization is applied to account for the decrease of fluorescence

intensity with depth, and is used for better visualization of the images. After these steps, the background is subtracted from the FNTD image. While there are three methods available in the FNTD software, in this thesis the default option, which is the Mosaic subtraction [68], was used for all the samples analyzed. This background subtraction tool from the Mosaic tool suit uses a histogram based algorithm by moving a sliding window (with window size specified in pixel) across the image, taking the most probable intensity value as the background. This method is suitable for removing background intensities that are higher than the track intensities. For optimal results, the window size needs be set large enough to reduce noise, while small enough to reproduce the signal trends in the FNTD. In this thesis, sliding window size of 30 pixels was chosen for all samples to get optimal results. After background subtraction, different corrections are applied to the image to account for sensitivity fluctuation across the FNTD, spherical aberration, field-of-view non-uniformity, and angular dependence of the fluorescence signal as described in detail in [70].

Step 2: Identification of "track spots"

After preprocessing the image and applying all the mentioned corrections, the next step is the identification of track spots, which uses the "particle tracker" functionality of the Mosaic tool suit, which contains the "feature point tracking" algorithm that is applied independently to each image slice (described in detail by Sbalzarini and Koumoutsakos [69]). The "tracking" options in the option file (which can also be adjusted via the GUI) is used to set the parameters for this step. The two main parameters for this process are the approximate particle radius in pixels and the intensity threshold for identification of a pixel in the center of a track spot. These parameters are chosen individually for each sample and fine-tuned based on a trial and error process to optimize the identification of most valid track spots. Figure 3.7 shows the track spot identification process for one of the samples analyzed.

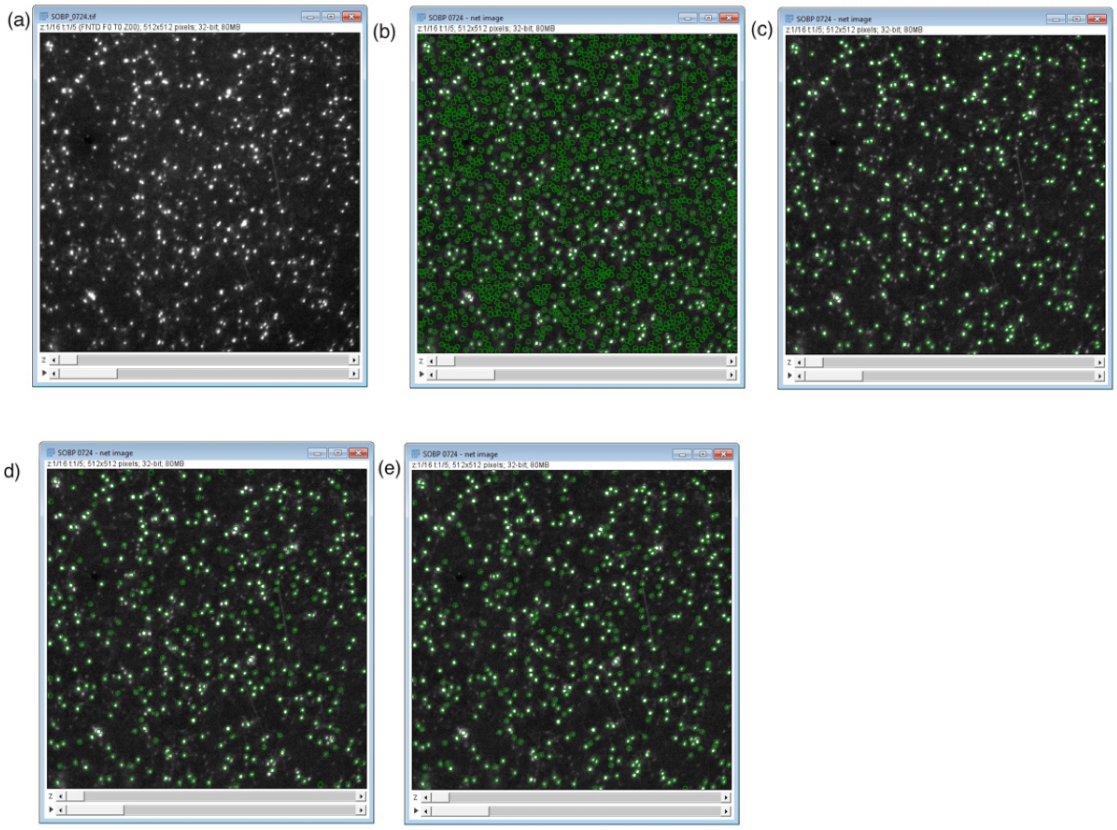

Figure 3.7: Identification process of track spots in an example sample. (a) Original unprocessed image. (b) Using a low intensity threshold for track spot identification resulting in over-estimation actual track-spots (too many false positives). (c) Track spots found using a high intensity threshold resulting in missing existing particle track spots. (d) Using an intermediate intensity threshold value, but with a higher radius size resulting in missing some adjacent track spots. (e) The final settings used for this sample with both intermediate intensity threshold and radius size, resulting in the optimum number of particles found while minimizing false track spots.

Step 3: Linking of track spots to different ion tracks

After the identification of track spots, they can be linked to a particle track trajectory in the linking process based on a 3D point tracking algorithm described in detail in [71]. Similar to the track spot identification, this process is also an interactive and iterative process that requires modifying the linking parameters and going back to track spot identification if necessary to find the optimal number of tracks that are visible while minimizing the false tracks arising from background noise or delta electrons. This is best performed using the maximum intensity projection of the image stacks in order to

see the particle trajectories and overlaying the tracks found onto the image. In addition to tweaking the linking parameters, to exclude delta electrons and other spurious tracks, a limit is set to the minimum number of track spots that can be present in a track or the number of image slices a track can be included in. These criteria are set in the "processing" option, which mark these excluded tracks as invalid tracks that can be visualized with the GUI.

The list of all parameters used for the linking process are shown in Table 3.3

Table 3.3: Important parameters for track identification in the linking stage of the FNTD package

Parameter	Description
Link range	Number of adjacent slices considered for potential linking partners. Link range of > 2 allows for skipping of slices within tracks
Displacement	Maximum distance in pixels per slice allowed between linking partners
Radius	Maximum radius of the track spots. Angle restriction can be ignored in tracks when the linking distance between two linking partners is smaller than half of the radius.
Distance weight	Weight used in the cost function for the distance between linking partners
Intensity weight	Weight used in the cost function for the difference in average intensity between the potential linking partner and the existing track
Velocity weight	Weight used in the cost function for the difference in velocity between the potential linking partner and the existing track
Maximum angle	Weight used in the cost function for the difference in angle between the potential linking partner and the existing track
Angle history	The number of track spots in the track, starting from the end of the track
Relinking	True or false value. If true, small tracks that appear to be parts of a common large track are joined together.
Relink cost factor	Maximum cost allowed for relinking which is multiplied by a general cost calculation function.
Relink displacement	Maximum allowed distance between the endpoints of tracks when relinking

Figure 3.8 shows the linking procedure for the example sample. As seen in the figure, some dimmer trajectories (corresponding to light fragments) were not linked. However, choosing parameters to include those tracks resulted in over-linking of other tracks and spurious (false-positive) tracks. Thus, the optimal settings were chosen to minimize this effect while including as many valid trajectories as possible.

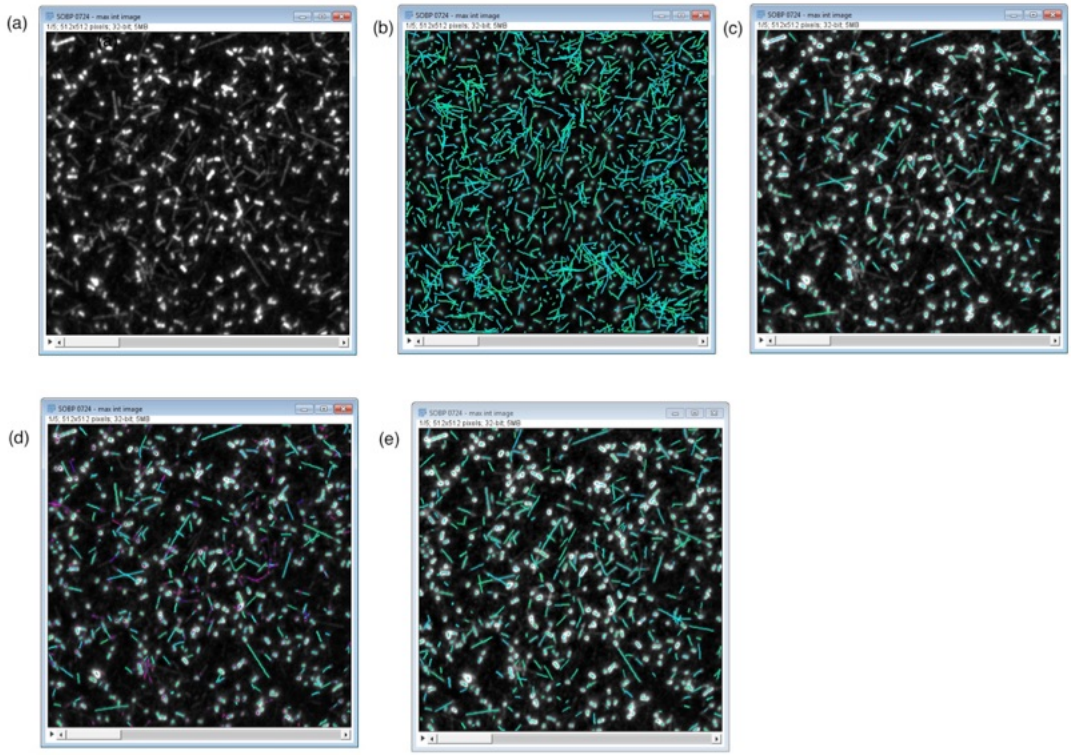

Figure 3.8: Linking track trajectories for sample SINF-SOBP-0724. (a) The maximum intensity projection image without overlay of tracks. (b) Using linking parameters to include all trajectories found resulted in too many false tracks. (c) Using a strict setting to minimize false-positives resulted in missing many dimmer trajectories. (d-e) The final optimal settings used to find the most trajectories visible while minimizing false tracks, with invalid tracks shown in (d) and filtered in (e).

Step 4: Track evaluation

The fluoresence signal is evaluated in terms of "track spot" intensity averaged along a particle trajectory, which can be used to estimate the LET. The FNTD software provides a number of estimators for the fluorescence intensity [67]. In this thesis the "amplitude" method was used. In this method, the maximum value (amplitude) within a certain radius (in pixels) around the "track spot" center is used as the intensity of the "track spot". This method is very robust against the overlapping of tracks, as tracks closer than a critical distance are excluded from analysis. After determination of intensity of each "track spot", they are averaged along each individual ion track. Additionally, geometrical track data are evaluated and reported by the software which include the start and end coordinates in x, y and z (both nominal and corrected for

refractive index), and the azimuth and polar angles. Additionally, these values are corrected for a potential tilt of the sample during irradiation and read-out [67]. The output from the FNTD image analysis, which includes information about track position, intensity and fluence for each individual track, was exported as a .txt file, and further analyzed with R and Matlab.

3.2.3 Monte Carlo Simulations

The Monte Carlo code FLUKA (versions 2011.2c.3 and later) [72] was used to simulate the radiation transport of the ions produced in the irradiation plans used and studied in this thesis in order to obtain the particle spectra with their respective atomic number, kinetic energies, direction cosines, energy loss and LET, and calculate dose and fluence at depths of interest. The simulations provide reference data that are used to compare the physical parameters obtained from FNTDs and perform LET calibration for the intensity spectra obtained from FNTDs, and carry out the simulation of the "Cell Dose" model for theoretical calculation of energy deposition in cell nuclei. For monoenergetic particles, energy and full width at half maximum (FWHM) of the beam were specified in the input card, while for the SOBP plans the Source card was used to incorporate multiple ions with different ion energies and fluence. The HADROTHE defaults for heavy ions were used and the DMJET-III and RQMD libraries were enabled. The irradiation settings used at HIT [Chapter 4] were incorporated in the geometry of the input file, using the appropriate material, and a simplified geometry of the ripple filter at HIT [73], which was shown to produce the correct depth dose profiles. The beam application and monitoring system (BAMS) and the air gap were also modeled using a simple geometry with water and air to give the WET for these structures. For obtaining the phase space of all individual particles crossing the boundaries of interest (specified by planes in the geometry of input) the user routine MGDRAW was used.

Chapter 4

Experiments

In this thesis, 4 irradiation experiments with FNTDs were conducted that were all performed at HIT's QA experimental room. Three of the experiments had cell coating on the FNTD, while one of the experiments was performed without any cells. Table 4.1 lists the experiments performed. The following describes the experimental setup for each of these experiments including irradiation setup, cell experiments and image acquisition using one of the two confocal laser scanning microscopes described in the previous chapter.

Table 4.1: Irradiation experiments performed

Experimental ID	Irradiation	Cell Line	Reference to setup
MN1000	270.55 MeV/u ^{12}C	A431	Section 4.1
SR308	Biologically Optimized ^{12}C SOBP	None	Section 4.2
SINF	Physically optimized ^{12}C SOBP	HT1080	Section 4.3
MN12000	Physically optimized ^{12}C SOBP	A539	Section 4.4
MN81000	Physically optimized ^{12}C SOBP	A539	Section 4.4

4.1 MN1000 Experiment

The first irradiation (sample MN1000) was selected from the previous work of Martin Niklas in our group [53]. The aim of this experiment was to validate the usability of FNTDS coated with cells irradiated with a common therapeutic carbon monoenergetic beam, and assess apoptosis of cells as a function of "Cell Dose" quantities.

4.1.1 Irradiation Setup

FNTDs coated with cells were irradiated perpendicularly with carbon ions having an initial kinetic energy of 270.55 MeV/u. The fluence was set to 10^7cm^{-2} and homogeneous across a field area of 8 x 8 cm^2. In order to achieve elevated LET inside the cells, the cells were positioned upstream of the Bragg Peak, corresponding to a water equivalent thickness (WET) of 14.26 cm. The cell-FNTD samples were placed in a 24 multiwell plate. 11.6 cm of PMMA (WET = 13.51 cm) was placed in front of the multiwell plate. The side of the FNTDs (WET= 1.645 mm) without cell coating were facing the incident beam and were attached to the bottom of the multiwell plate (polystyrene with WET = 1.2 mm) by agarose droplets. The additional materials in front of the beam isocenter, including the beam application monitoring systems, air gap, and a 3 mm ripple filter, resulting in a total WET of 2.89 mm, also contribute to the entire calculated WET. Figure 4.1 shows the irradiation set up.

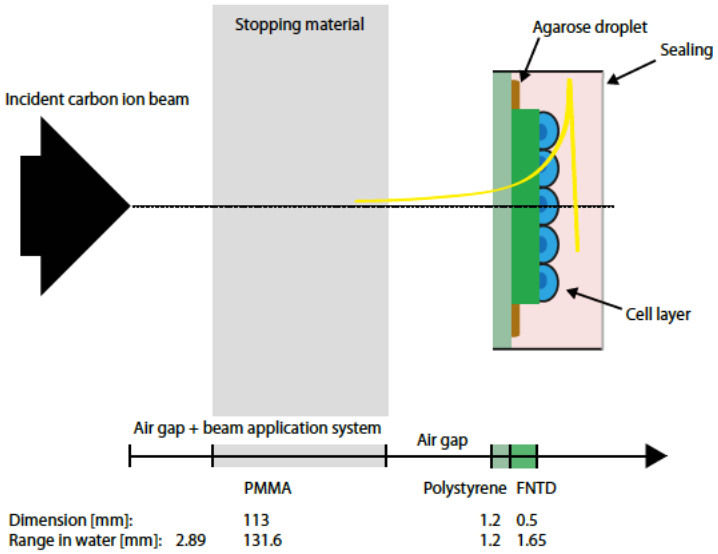

Figure 4.1: Irradiation Setup for sample MN1000. Reprinted from [53]

4.1.2 Cell Experiment

In this experiment, human epidermoid carcinoma (A431) cells were cultured and used to coat FNTDs as part of a FNTD-cell hybrid system, described in detail in [53]. The

chromatins were stained with 1.2 μm of Draq5 for nuclear delineation, and for live cell imaging, 1 μm of fluorescent caspase-3 substrate were added.

4.1.3 Image Acquisition

The readout of this sample, both the FNTD and the cell compartment, was done with the Zeiss LSM710 Confocor 3, confocal microscope. At first the FNTDs were read out with 633 nm HeNe laser line with relative laser power of 100 %. The pixel dwell time (τ) was set to 12.90 μs, line scanning repetition (R) set to 4, and pinhole to 1 AU. The main beam splitter MBS 488/561/633 was placed in the optical path. Furthermore, a 655 nm long-pass filter was placed in the fluorescent emission path and the Avalanche Photo Diode (APD) for emission detection was used in photon counting mode. An imaging plane of 224 x 224 μm^2 (2000 x 2000 pixels) measured at 30 μm below the FNTD surface was recorded. After recording the FNTD plane, time series (25 time points at 45 minute intervals) of the cell compartment were recorded up to 19 hours after irradiation. The acquired cell layer stack covered a range of about 20 μm with a z-interval of 2 μm (pixel settings were equal to FNTD read-out). The cell layer was imaged with the 633 nm HeNe laser line (p= 1% transmission) for Draq5 and with a 488 nm Argon laser line (p= 2% transmission) for NucView 488 (caspase-3 substrate). For Draq5 a MBS of 488/561/633 nm and APD detection with 655 nm long-pass filter were used. For NucView 488 a MBS of 488 nm and photomultiplier detection were used. For both channels the imaging parameters of: τ = 1.61 μs, R= 2, and pinhole=1 AU were used.

4.2 SR308 Experiment

The second set of irradiations (done as one of the main parts of this thesis work [74]) was performed with FNTDs without any cell layer. The aim of this experiment was to assess how the "Cell Dose" quantities and their variation compare at different depths of a biologically optimized SOBP, when the RBE-weighted dose is constant.

4.2.1 Irradiation Setup

For this irradiation experiment, 18 different ^{12}C iso-energy slices ranging from 219 MeV/u to 280 MeV/u were used to create a SOBP optimized for a biological dose of 2 Gy (RBE from Chordoma cells) for the plateau depth in water situated at 10-15

cm. The irradiation field size was set to 10x10 cm^2 to achieve homogenous irradiation across the FNTDs. The FNTDs were attached to slabs of RW3 water-equivalent plastic phantoms (manufactured by PTW at Freiburg) at 7 different positions corresponding to WETs of 0.75, 1.75, 8.75, 10.75, 12.75, 14.75 and 17.75 cm. As in the previous irradiation, a WET of 2.89 mm was included to account for the materials between the exit window of the beam line and the isocenter, in addition to a WET of 1.65 mm to account for 0.5 mm of FNTD (as the FNTDs were attached to the phantom slabs on their non-transparent sides).
Figure 4.2 shows the irradiation setup for this experiment.

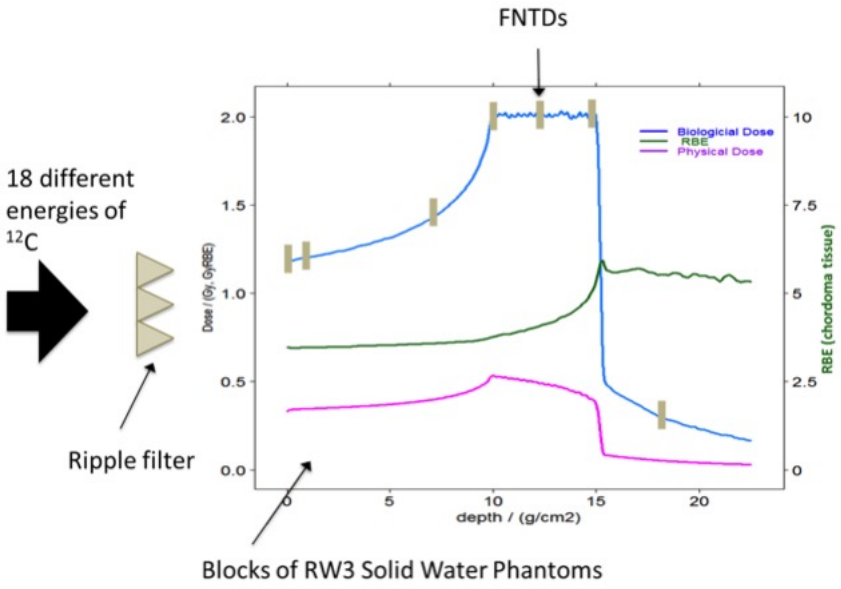

Figure 4.2: Irradiation Setup for SR308 samples

4.2.2 Image Acquisition

After irradiation, the FNTDs were imaged with the Zeiss LSM710 Confocor 3, using 63x/1.40 NA oil objective. 633 nm HeNe laser line with relative laser power of p=7 % and pixel dwell time $\tau = 40$ μs was used to readout the detectors. The main dichroic beam splitter (MBS488/561/633) and 655 nm long-pass emission filter were used to separate the fluorescence signal from the emission signal. Avalanche Photo Diodes (APDs) were used in photon counting mode to detect the emission signal. Image planes with dimension of 134.8 x 134.8 μm2 (1280 x 1280 $pixels^2$) were recorded starting 30

μm below the surface of the FNTDs for a total of 21 z-stacks with an axial spacing of z=3 μm.

4.3 SINF Experiment

The third set of irradiations were performed in collaboration with MD Anderson colleagues, as part of a Sister Institute Network Fund (SINF) project [51]. The aim of these experiments was to assess the DNA damage response (DDR) in mixed radiation fields and correlate it with microscopic energy deposition in cells using beam line microscopy [Section 3.1.3.2], which allows to observe the biological response directly after irradiation.

4.3.1 Irradiation Setup

These irradiations were performed with placing the FNTD-cell samples in a custom designed beam-line microscope [50] [Section 3.1.3.2] . Fifteen different ^{12}C iso-energy slices ranging from 132 to 196 MeV/u were used to create a SOBP with plateau depth in water of 4-8 cm and optimized for a physical dose of 0.5 Gy in the SOBP. The irradiation field size was set to 3 x 3 cm^2. The FNTD-cell samples were positioned at two different positions, either in the entrance region (WET of 0.7 cm) or in the distal end of the SOBP (WET of 7.2 cm). These two depth positions were achieved by placing either 0.6 cm or 7.1 cm of RW3 slabs, that have same WET as water, between the microscope and the beam nozzle. The additional WET of 0.1 cm was added to account for volume of cell medium that is located in front of the cell monolayer. The slab surfaces were positioned at the isocenter, and a small air-gap existed between the slab exit and the sample to allow the microscope z-stage to move freely. Similar to the other irradiation setups the WET of 0.289 cm was included for the beam nozzle, the beam application and monitoring system (BAMS), and the air gap from the iso-center. Figure 4.3 shows the actual irradiation setup with the in-beam microscope used at HIT.

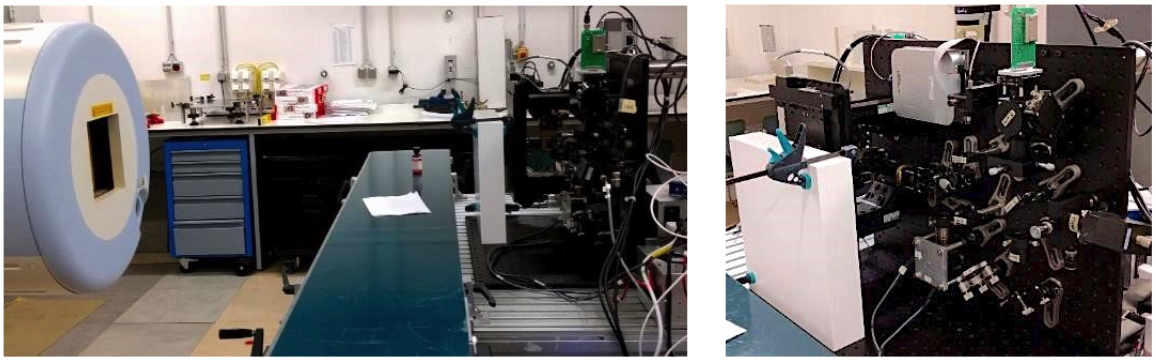

Figure 4.3: Irradiation Setup for SINF samples at HIT

4.3.2 Cell Experiment

In these experiments HT1080 human fibrosarcoma cell line was used, which was transfected to express eYFP tagged to 53BP1 in order to visualize radiation induced foci in the cell nucleus that arise from the DNA-damage response. For cell-FNTD hybrid experiments, the cells were placed in cell-chambers designed for horizontal irradiation [51]. These cell chambers consist of circular FNTD wafers (as described in Section 3.1.1), a 1 mm thick silicone gasket and a #1.5 glass coverslip. For holding the cell chamber together, a locking-ring brass holder was used, creating a liquid-tight seal. Detailed description of the cell culture and sample preparation can be found in the published manuscript [51]. The samples were placed in a beam-line microscope for live-cell imaging pre and post irradiation.

4.3.3 Image Acquisition

The images for these experiments were acquired by scanning an imaging filed of 100 μm x 100 μm with a pixel size of 0.195 μm (512 x 512 pixels^2). The pixel dwell time was set to 10 μs/pixel with a sample averaging of 2 per pixel. 488 nm laser was used for the excitation source with a voltage of 0.4 V. The same field size was used to image cells and FNTDs. Time-lapse z-stacks were acquired for five fields per irradiation. Cell volumes were recorded starting just below the cell nucleus by scanning10-μm z-stacks with a step size of 1 μm. Two control scans were obtained per field before irradiation, spaced about 5 minutes apart in order to distinguish between endogenous and radiation induced foci. A fast single slice scan of only 256 x 256 pixels was obtained for each field to reference the position of the cells right after irradiation in order to later correct

for cell migration. After irradiation, fields were scanned by using a time course of 5 minute/frame for 30 minutes then 10 min/frame for another 30 minutes in order to monitor the foci development. After imaging the cells, the FNTD volume was imaged. To ensure proper co-registration of the FNTD tracks and nuclei positions, the xy-stage position was repositioned to the original coordinates of the reference positions. For FNTDs, a dwell time of 75 μs/pixel was used with a 15 sample/pixel average. The 635 nm laser was used for the excitation source with a voltage of 4.5 V. FNTDs were scanned from 5 μm to 35 μm relative to the bottom slice of the cell nucleus with a z-step of 2 μm.

4.4 MN81000/MN12000 Experiments

The fourth set of experiments were performed by Dr. Martin Niklas and colleagues from Clinical Cooperation Unit Translational Radiation Oncology at DKFZ [52]. The aim of these experiments was to investigate the biological response of a larger number of cells to heterogeneous energy deposition of radiation from a carbon mid-SOBP. The experiments MN81000 and MN12000 are part of one experimental set up, with the difference being that in MN12000 the FNTD coated with cells was placed in a carbon mid-SOBP optimized to 0.5 Gy absorbed dose, while for MN81000, the mid-SOBP was optimized to 1 Gy.

4.4.1 Irradiation Setup

For these experiments, 6 different ^{12}C iso-energy slices ranging from 122 MeV/u to 139 MeV/u were used to create a 1 cm wide SOBP optimized for a physical dose of 1 Gy (MN81000) and 0.5Gy (MN12000). The FNTD covered with cell layer was positioned in the middle of the SOBP with a WET of approximately 3.5 cm (Figure 4.4). Similar to MN1000, the sides of the FNTDs without cell coating were facing the incident beam and were attached to the bottom of the multiwell plate. PMMA of 3 cm thickness was used as blocking material in front of the FNTD.

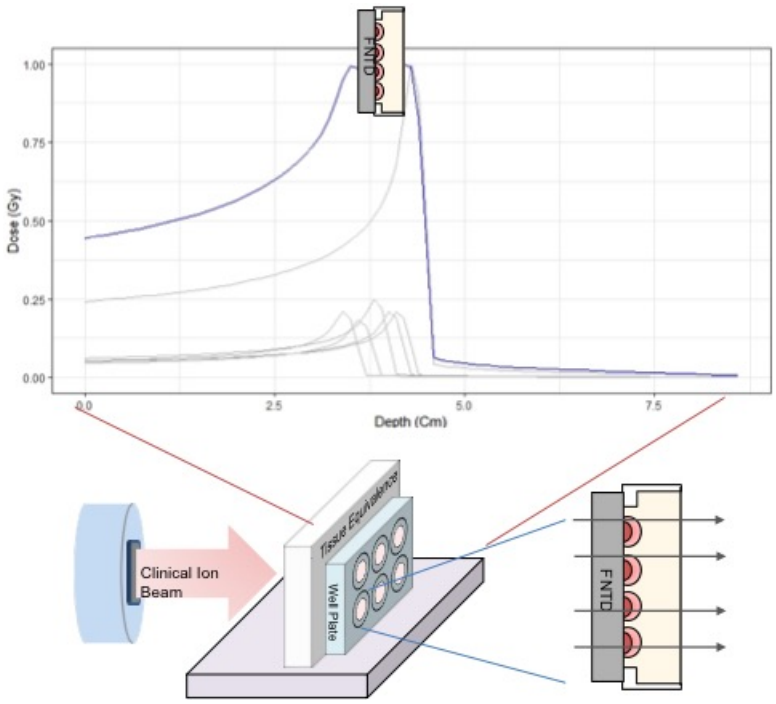

Figure 4.4: Irradiation Setup for MN81000/MN12000 experiments. Image partially reproduced from [52]

4.4.2 Cell Experiment

For these experiments A549 human Non-Small-Cell-Lung-Carcinoma (NSCLC) cells were cultured for FNTD coating. Respective medium lacking phenol-red was used for live cell imaging. The cells were retrovirally transduced with a construct coding for the N-terminus of 53BP1 fused to the sequence coding for fluorescent mCherry-protein and selected with puromycin.

4.4.3 Image Acquisition

After irradiation, the FNTDs were imaged with the Zeiss LSM710, Confocor 3 using 40x oil objective objective. The zoom was set to 1.1, number of rescans set to 2, and dwell time set to 6.3 μs. Image planes with a dimension of 1024 x 1024 pixels^2 (1 pixel=0.189 μm) were recorded for a total of 21 z-stacks with an axial spacing of z=5 μm, starting at 5 umm below the FNTD surface. Transmission photomultiplier tubes (T-PMTs) were used to record the spinels in the transmitted-light channel. Spinels are defects in the crystal structure of FNTDs that were used to register the images. Avalanche photo

diodes (APDs) with long-pass filter (detection window > 650 nm) were used to image the FNTD "track spots". The cell layer recorded by inverted widefield microscopy (XL7, Olympus) using 20x/0.8 air objective with illumination system MT20 arc burner 150W Xe/Hg, grayscale CCD Hamamatsu Orca-ER camera. The exposure time of 4 ms and 200 ms were used for bright field channel and fluorescence channel, respectively. Image stacks containing 3 planes of dimensions 2048 x 2048 pixels^2 (1 pixel = 0.325 μm) with axial spacing of 1.5 μm were obtained.

Chapter 5

Development of the New Framework for Single Cell Dosimetry

5.1 Theoretical Basis

The theoretical framework is a novel framework that was developed as the main focus of this work. A description of this novel framework was published in [74].

5.1.1 Defining New Quantities

In order to create a computational model to calculate energy deposition inside the cell nucleus and its variation across the cell population, it is necessary to first define new quantities relevant at a microscopic cellular scale that is analogous to macroscopic quantities absorbed dose and LET. Absorbed dose and LET are important beam parameters that can be obtained from treatment planning data and conventional dosimetric measurements. They are suitable for quantifying and characterizing energy deposition in larger volumes appropriate for tumors and organs at risk and can be used as a measure to compare energy deposition between such volumes. Likewise, the new quantities defined for the new "Cell Dose" model should have the same criteria of energy deposition specification, but for microdosimetric volumes appropriate for cellular and sub-cellular scales such as the cell nucleus. The microdosimetric quantities specific energy and lineal energy give a more tailored surrogate for dose and LET for volumes at the DNA level. However, they do not fulfill the criteria of using a single quantity for comparison across the cells of the same population and require a comparison of their distributions [Chapter 2]. Furthermore, these quantities are not easily measurable with current cell-hybrid

detectors. So according to the aim of this thesis, quantities that can be an intermediate step between the two (macroscopic quantities and microdosimetric quantities) that can directly be measured experimentally and correlated to single cell biological outcome is needed. To fulfill these criteria the quantities "specific dose", denoted as $\widetilde{D}$, and "specific LET", denoted as $\widetilde{L}$, were introduced in this thesis and defined as follows:

Specific dose is a quantity that can potentially be measured with cell-hybrid detectors such as FNTDs and is defined as the total amount of energy deposited in microscopic volume such as the cell nucleus ($\widetilde{D}_{nuc}$). This definition was adopted from microdosimetry and modified as an alternative and an intermediate quantity between specific energy and dose, which measures energy imparted to the microscopic volume per unit mass. Similarly, the new quantity "specific LET" is introduced in this thesis as a surrogate and intermediate quantity between LET and lineal energy and is defined as the total energy imparted to the microscopic volume divided by the sum of all chord lengths of particles inside that volume using the same sources of variations as specific dose. It is to be noted that the volume of these microscopic quantities can be specified in scales smaller or larger than the cell nucleus depending on the purpose of the measurement and measurement capabilities of the cell-hybrid detector. These volumes can be reduced to smaller volumes that, for example, are used for biological models such as nuclear domains and local dose as for benchmarking those models. For the main application of this thesis the cell nucleus was selected as the main target of energy deposition and therefore $\widetilde{D}_{nuc}$ and $\widetilde{L}_{nuc}$ are defined as follows:

$$\widetilde{D}_{nuc} = \frac{\epsilon_{nuc}}{m_{nuc}} \tag{5.1}$$

where ϵ_{nuc} is the energy imparted to the nucleus and m_{nuc} is the mass of the nucleus. and,

$$\widetilde{L}_{nuc} = \frac{\epsilon_{nuc}}{\sum x} \tag{5.2}$$

again ϵ_{nuc} is the energy imparted to the nucleus and $\sum x$ is the sum of the chord length of all primary ions and fragments crossing the nucleus.

It should be noted that these quantities are of stochastic nature (like the microdosimetric quantities) and not averaged over particles (like dosimetric quantities).

With a cell population of n cells, one can have a mean specific dose:

$$\mu(\widetilde{D}_{nuc}) = \frac{\sum_{i=1}^{n} \widetilde{D_i}}{n} \tag{5.3}$$

with its variation $\hat{\sigma}$ as:

$$\hat{\sigma}(\widetilde{D}_{nuc}) = \frac{\sigma(\widetilde{D}_{nuc})}{\mu(\widetilde{D}_{nuc})} \tag{5.4}$$

where $\sigma(\widetilde{D}_{nuc})$ is the standard deviation, and similarly a mean specific LET:

$$\mu(\widetilde{L}_{nuc}) = \frac{\sum_{i=1}^{n} \widetilde{L}_i}{n} \tag{5.5}$$

with its variation $\hat{\sigma}$ as :

$$\hat{\sigma}(\widetilde{L}) = \frac{\sigma(\widetilde{L})}{\mu(\widetilde{L})} \tag{5.6}$$

when the number of cells gets larger, the mean specific dose approaches the macroscopic dose (D), while the mean specific LET approaches the quantity LET_f:

$$\lim_{n\to\infty} \frac{\sum_{i=1}^{n} \widetilde{D_i}}{n} = D \tag{5.7}$$

and

$$\lim_{n\to\infty} \frac{\sum_{i=1}^{n} \widetilde{L}_i}{n} = LET_f \tag{5.8}$$

This approximation is specific for the situation investigated, where dose is relatively low (few hits per cell), but the number of cells is relatively high (few 1000).

5.1.2 Identifying Sources of Variation

Based on the way that specific dose and specific LET are defined, they can be derived by incorporating all relevant sources that contribute to the total energy imparted to the cell nucleus and cause variation in the cell-wide population. While there are different sources that can contribute to this energy deposition and cause variation, only sources that have the most significant impact were chosen. The rationale behind choosing the sources of variation were based on the factors discussed in the interaction of heavy ions with matter [Section 2.2], the stochastic nature of energy deposition [Section 2.7], and a cursory statistical evaluation of these sources at an exemplary mid-SOBP condition pertinent to the cases studied in this thesis. Furthermore, some simplifying assumptions had to be made that will be discussed. Assuming a homogeneous cell density and homogenous biological and chemical environment across different cell nuclei in the population, one

can say that the variation in energy deposition is caused by the different particles crossing the cell nucleus and the way and amount each particle deposits energy in the cell nucleus. As the definitions of specific dose and specific LET require calculating the mass of the cell nucleus, nucleus size is one of the sources of variation to consider. To see how much variation is seen in the cell nuclei size the variation in the cross-sectional area of the cells studies were analyzed. Figure 5.1 shows the distribution of the maximum intensity projection of nuclei area of 2430 cells that were studied in this thesis. As seen from the figure, nucleus size distribution shows a gaussian distribution with mean area of 183.2 μm^2 and standard deviation of 93.7 μm^2. This results in the calculated variation in nuclei area ($\hat{\sigma}(A_{nuc})$) of 51 %, and therefore nucleus area was included as one of the sources of variation in the "Cell Dose" model.

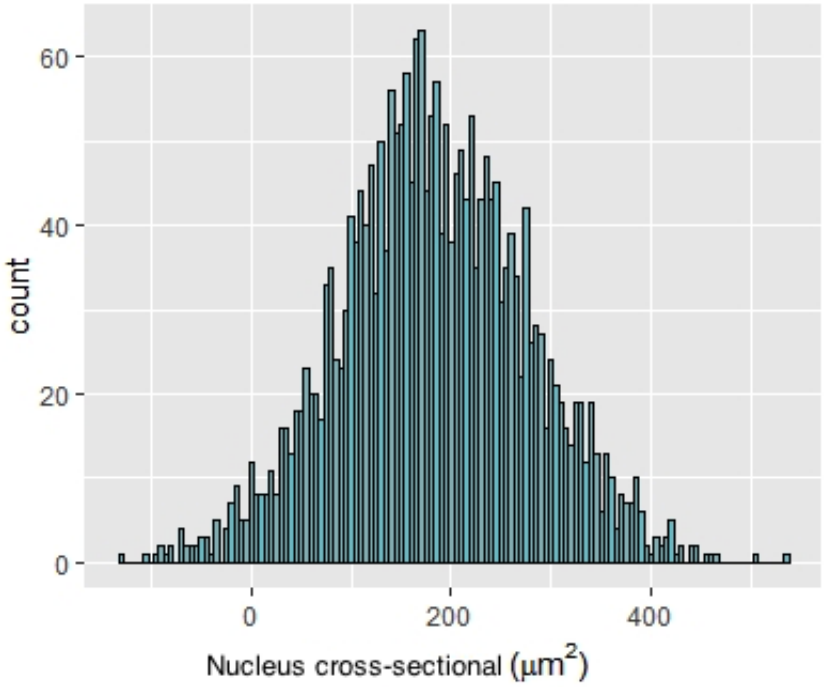

Figure 5.1: Distribution of the cross-sectional area of 2430 cells analyzed in this thesis

The next step in calculating the amount of energy imparted to the nucleus is finding the the number of particles that cross the cell nucleus. To explore the significance of nuclear hits, the carbon ion mid-SOBP plan optimized to 1 Gy physical dose from the MN81000 experiment [Section 4.1] was used as an example case. Figure 5.2 shows the distribution of particles crossing the nucleus (nuclear hits) for the mentioned experiment. The distribution has a mean of 28 nuclear hits and a standard deviation of 5.5, resulting in

a nuclear hit variation ($\hat{\sigma}(N_{hits})$) of 19.6 %. Due to this relatively high variation, the number of nuclear hits was also considered as a significant source of variation.

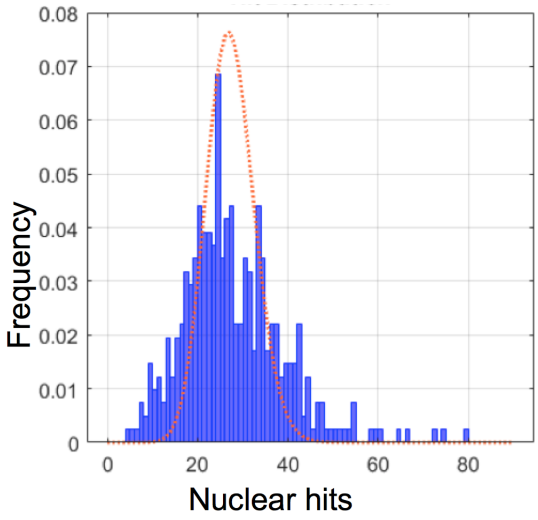

Figure 5.2: Distribution of nuclear hits for the MN8100 experiments. Image courtesy of Martin Niklas.

After identifying the number of nuclear hits one needs to calculate the energy deposition of each particle crossing the cell nucleus. While one can perform detailed Monte Carlo simulations following each ionization interaction, one can simplify this process by first knowing the average energy deposition of the ion along its path and then considering the variation for each individual case. This can be calculated by knowing the LET of the impinging ion and its cord length in the nucleus. Afterwards, since the actual deposition by each individual ion varies from the average energy deposited due to energy loss straggling [Section 2.7], one needs to account for that as well. By sampling this distribution, Figure 5.3 shows the LET distribution of the particle spectrum of the mentioned MN81000 experiment. As can be seen from the figure, the LET varies greatly, with a mean and standard deviation of 32.3 keV/μm and 25.8 keV/μm, respectively, resulting in a variation ($\hat{\sigma}(LET)$) of 87 %.

To consider the effect of energy loss straggling, Monte Carlo simulation of energy loss for various particles with different energies spanning the energies found in the range of particle spectrum of the MN81000 mid-SOBP case was performed using the MC code FLUKA [Section 3.2.3]. For each particle chosen, the energy loss was simulated in a cube phantom of 10 μm thickness (to represent cellular scale) for a total of 10^6 times,

and the mean and standard deviation of the energy loss were calculated. Figure 5.3 illustrates the variation in energy loss for different particle types of different LETs, which represent energy loss straggling. As can be seen from the figure the variation reaches up to around 400 % for protons and around 50 % for carbon ions, therefore making straggling a significant source of variation for specific does and LET.

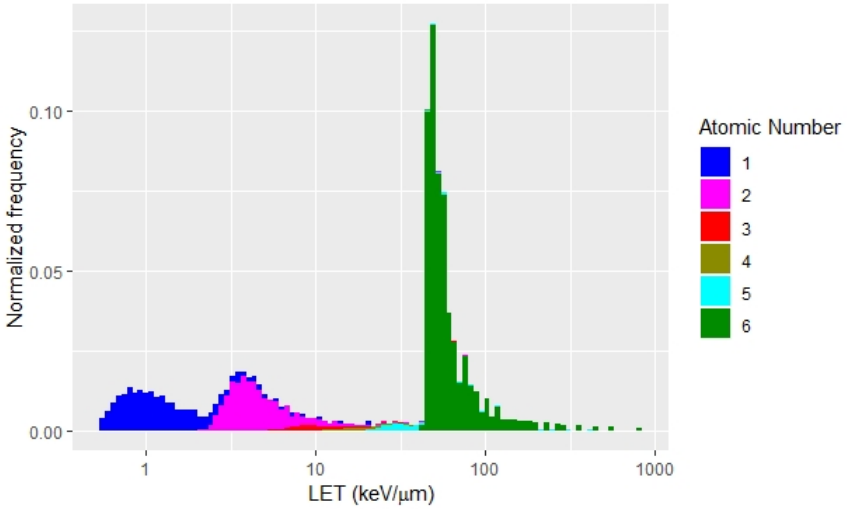

Figure 5.3: LET distribution of particle spectrum corresponding to MN81000 experiment for carbon mid-SOBP plan

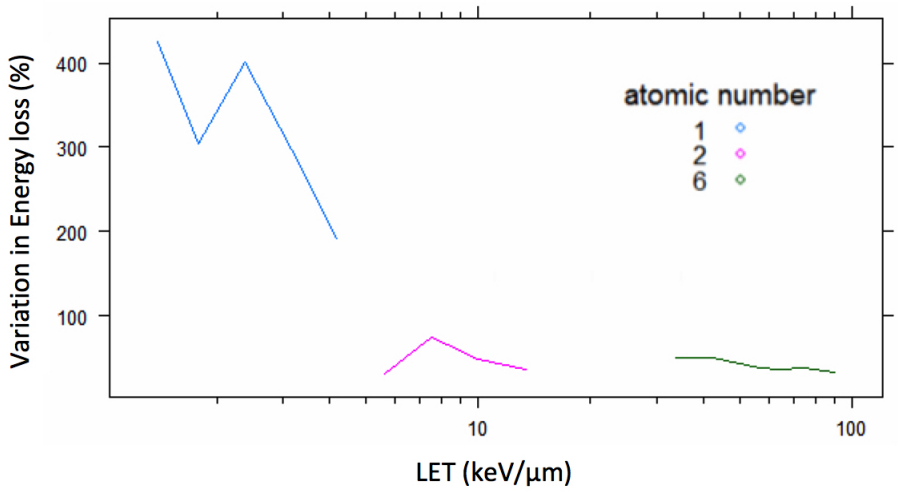

Figure 5.4: Energy loss straggling for different ions found in the particle spectrum

The next source that was evaluated for consideration was the shape of the track structure with regards to the distribution of secondary electrons around the track as estimated by the radial dose distribution (RDD) [Section 2.3.6]. To evaluate the effect of radial dose distribution, the Libamtrack library [Section 3.2.1.4] was used, by choosing the built-in RDD model based on the extended target RDD model proposed by Cucinotta *et al.* [75]. Again several particles in the particle spectrum range of the mid-SOBP case were chosen to perform a preliminary evaluation. The calculation showed that within 1 μm from the particle almost 100% of the dose (with 1E-6 % accuracy) are deposited for all the particles chosen in the range. For this reason, RDD was not considered a significant source of variation for the current "Cell Dose" model, as the target size is in the micrometer scale.
The other sources that were also considered but not included in the current model were the range and range straggling of the impinging particles, as they also did not have a significant effect within the micrometer scale.

In summary, the set of identified sources of energy deposition variation for the "Cell Dose" mode include: size of the nucleus, number of nuclear hits, LET of the particles, energy loss straggling of the particles, and chord length of the crossing particles. Radial dose, range and range straggling and other potential sources were excluded due to their low significance in the cellular scale and the computational cost of including such

parameters in the current model.

After identifying the relevant sources for calculating specific dose and specific LET, a sampling model based on the probability distribution of each of the sources was constructed to evaluate these quantities, which will be discussed in detail below. If the distribution of the sources is known and can be modeled with a well known analytical distribution, then the analytical distribution was used. Otherwise, the probability distribution was obtained from available experiments or simulation data. As with any sampling method, first a probability density function (*pdf*) is identified, from which the cumulative density function (*cdf*) is derived. Subsequently, a random variable from the *cdf* was sampled, which can be done using the built in functions of most numerical programs, such as R, as used in this thesis.

The sampling is done in n iterations (where n is very large) and repeated for m to avoid non-stochastic correlation. In this thesis n was set to 10^6 and m set to 100, with the sampling performed via a straight forward sampling method implemented in R. When testing to see how fixing one of the sources as constant will affect the "Cell Dose" quantities (as discussed later), the expected value of the distribution for the corresponding variable was used in the simulation. Figure 5.4 shows the schematic diagram of the sampling method, which will be discussed as follows.

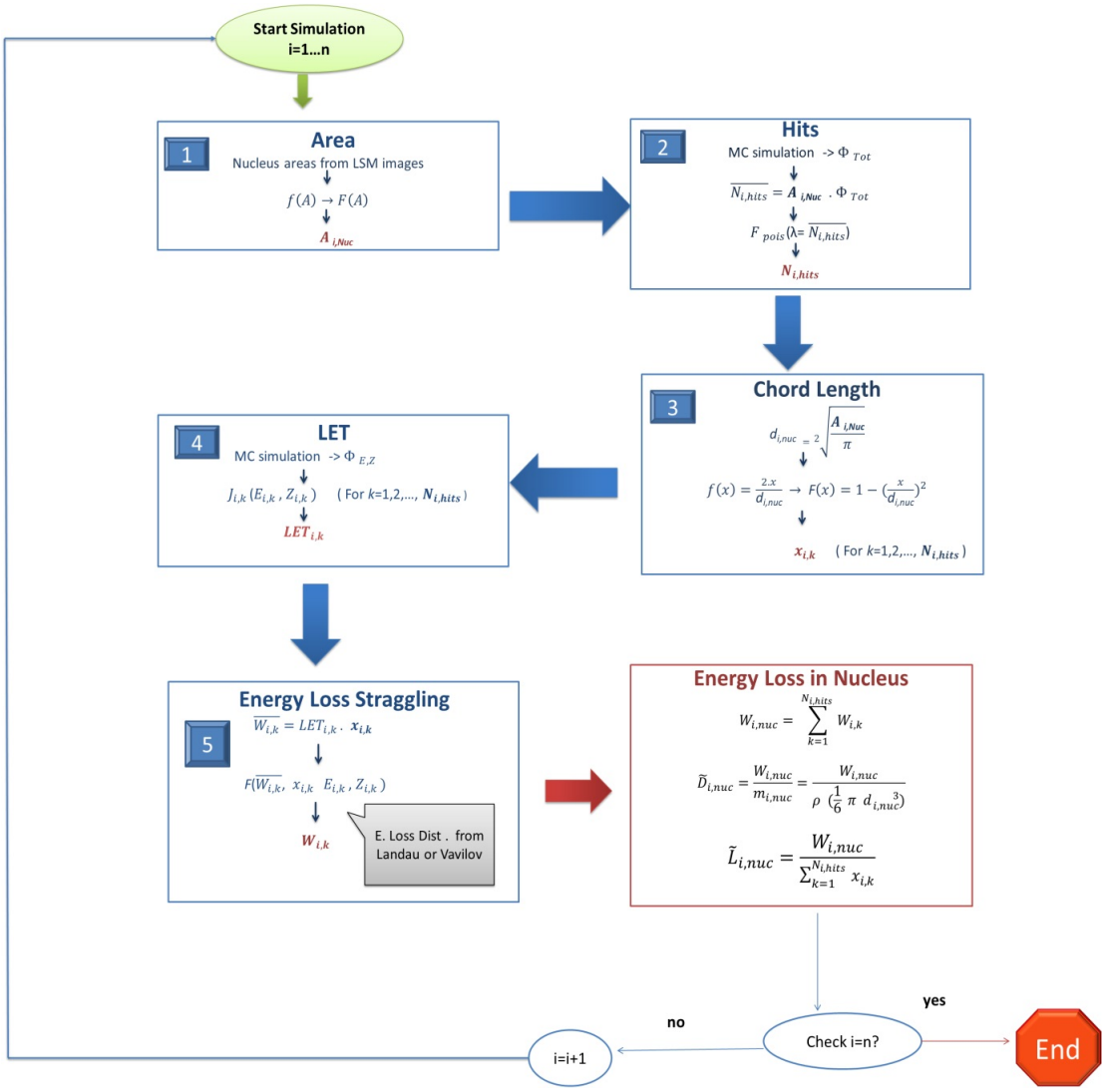

Figure 5.5: Simulation diagram for the sampling method of "Cell Dose" model

Step 0: Obtaining the particle spectrum at the depth of interest:
Most of the sampling steps in the computational model require the particle spectrum which can be either obtained from Monte Carlo simulations or from the treatment planning data. Therefore, before performing the sampling simulation, the phase space of particles for the desired depth was obtained. As sampling from the entire phase space can be computationally expensive, the phase space at boundary conditions of the depths of interest containing the total fluence (Φ_{tot}), direction cosines of each particle, the atomic number (Z), kinetic energy (E), and the LET (or energy deposited) was converted to a frequency spectrum with respect to the kinetic energy, thus creating a

pdf to sample particles (in which the frequency of the particles provide the probability).

Step 1: Sampling the nucleus cross-sectional area:
The nucleus size affects the number of hits, the chord length distribution, and the volume of energy deposition. One can obtain distribution of nucleus size for the cell line of interest, and if the sample size is large enough, it can be used to directly sample from the available data. Alternatively, if the distribution shows a Gaussian distribution (as expected), the mean and standard deviation of the nucleus size data can be obtained in order to generate a random number using the Gaussian distribution. In principle, any shape of the nucleus can be used for a generalized model. For the simplified version (for faster computation), as used in this thesis, the nucleus was assumed to be a sphere. Therefore, the distribution of nuclei cross-sectional area was obtained from the images of 2430 cell nuclei analyzed in this thesis (Figure 5.1) by assuming the maximum intensity image of the cell layers to be the circular cross-sectional area of the nuclei sphere, thus providing a *pdf* from these images to sample the nuclei size. Thus, for each each iteration i ($i = 1, ...n$), a nucleus area $A_{i,nuc}$ was obtained from the *pdf*. In the case that the area needs to be set as constant, $A_{i,nuc}$ is set to mean of the area distribution ($\overline{A_{i,nuc}}$).

Step 2: Sampling of the particles hitting the nucleus:
For this step, it is assumed that the number of particles hitting the cell nucleus follows a poisson distribution, which has a known analytical *pdf* and *cdf*. Therefore, by knowing the mean, one can sample from a built-in program (as provided in R) that generates random number based on poisson distribution. The *pdf* of the poisson distribution with mean λ, in which N (0,1,2..) is the number of hits, in this situation is:

$$p(N;\lambda) = \frac{e^{-\lambda}\lambda^N}{N!} \tag{5.9}$$

and consequently one can have a Poisson *cdf* of

$$F(N;\lambda) = \sum_{i=0}^{N} \frac{e^{-\lambda}\lambda^i}{i!} \tag{5.10}$$

Here λ is the expected number of hits to the nucleus, denoted as $\overline{N_{i,hits}}$. Given the macroscopic total fluence ϕ_{tot}, which was obtained from step 0, and the nuclear area of interest $A_{i,nuc}$ (obtained from step 1), one obtains $\overline{N_{i,hits}}$:

$$\overline{N_{i,hits}} = \phi_{tot}.A_{i,nuc} \tag{5.11}$$

For each iteration i, the $N_{i,hits}$ was sampled using the poisson distribution described. For the case of switching off the variation in number of hits, $N_{i,hits}$ was set to the mean number of hits $\overline{N_{i,hits}}$.

Step 3: Sampling the chord length:
As discussed previously, in order to calculate how much energy a particle deposits in a volume, one needs to know the path length of the particle transversal across the volume, which is a complicated process. One can simplify the process assuming the path length to be a straight line from the point of entry to the point of exit, thus using the chord length across the volume as the path length. As discussed in step 1, the nucleus was simplified as a sphere, and spherical volumes have an analytical distribution of chord lengths [76]. For each sampling iteration i, the diameter $d_{i,nuc}$ of the cross-sectional nucleus area $A_{i,nuc}$ obtained from step1 is:

$$d_{i,nuc} = 2\sqrt{\frac{A_{i,nuc}}{\pi}} \tag{5.12}$$

The *pdf* of chord length x is given by the following function:

$$f(x) = \frac{2x_i}{d_{i,nuc}^2} \tag{5.13}$$

Likewise, the *cdf* for chord length x can be calculated by the following:

$$F(x_i) = 1 - \int_{l0}^{d_{i,nuc}} f(x_i) \tag{5.14}$$

$$F(x_i) = 1 - (\frac{x_i}{d_{i,nuc}})^2 \tag{5.15}$$

Subsequently, using the *cdf* from equation 4.15, for each iteration i and nuclear hit k (obtained from step 2), a chord length ($x_{i,k}$) was sampled. In the case of holding the chord length constant, $x_{i,k}$ was set to the average of the chord length distribution, which is $\frac{2.d_{i,nuc}}{3}$.

Step 4: Sampling the particle LET:
After finding the number of nuclear hits, for each iteration i, a particle was sampled based on the spectrum distribution of the particles that was obtained from step 0. Therefore, for each nuclear hit k, where $k = 1, 2, ..., N_{i,hit}$, a particle ($J_{i,k}(E_{i,k}, Z_{i,k})$ was sampled from the particle spectrum. The $LET_{i,k}$ of the sampled particle was determined from its charge ($Z_{i,k}$) and kinetic energy ($E_{i,k}$) using the Libamtrack library.

Step 5: Sampling of the energy loss for each particle:
If the path length of the particle traversal is very small it can be assumed that the LET of the particle remains constant over the volume of interest [77, 78], which is the case for microscopic size of the cell nucleus. Subsequently, for each of the particles $J_{i,k}(E_{i,k}, Z_{i,k})$ sampled in step 4, the average loss per particle, $\overline{W_{i,k}}$, can be calculated by multiplying the chord length $x_{i,k}$ (from step 3) by the LET (obtained from step 4):

$$\overline{W_{i,k}} = x_{i,k}.LET_{i,k} \tag{5.16}$$

As mentioned previously, due to statistical nature of ionization process, the energy loss in thin targets are subject to straggling. Knowing the $Z_{i,k}$, $E_{i,k}$, $x_{i,k}$, which was obtained from previous step, one can obtain the *pdf* and *cdf* of energy loss using the well-known theories discussed such as Landau and Valvilov as discussed in Chapter 2 [Section 2.7]. These *cdf*s have been implemented in the Libamtrack library, and were used in this thesis to sample the energy loss, $W_{i,k}$, for each of the particles.

Step 6: Obtaining the total energy imparted to the nucleus and the quantities specific energy and specific LET:
For each iteration i, the total energy imparted to the nucleus $W_{i,nuc}$ is the sum of the energy loss for alls tracks crossing the nucleus i:

$$W_{i,nuc} = \sum_{k=1}^{N_{i,hits}} W_{i,k} \tag{5.17}$$

Referring back to the definition of specific dose and specific LET for each iteration i we have:

$$\widetilde{D}_{i,nuc} = \frac{W_{i,nuc}}{m_{i,nuc}} = \frac{W_{i,nuc}}{\rho_{nuc}(\frac{1}{6}\pi {d_{i,nuc}}^3)} \tag{5.18}$$

and

$$\widetilde{L}_{i,nuc} = \frac{W_{i,nuc}}{\sum_{k=1}^{N_{i,hits}} x_{i,k}} \tag{5.19}$$

where ρ_{nuc} is the density of nuclei, which for this thesis is assumed to be the density of water.

5.1.3 Specifying Cases to Study

One of the aims of thesis was to apply the new "Cell Dose" model to test the applicability and benefit of cell-hybrid detectors. To accomplish this goal, 5 different conditions

were chosen that shows how adding different components of a cell-hybrid detection system eliminates uncertainty from the measured quantity and also showing which sources of variation plays the most significant part in the cell-wide population. This will illustrate which quantities need to be accurately measured and also shows if measuring these quantities with the mentioned system adds additional value to quantities that can be obtained from the beam parameters alone. Table 5.1 describes the five different conditions that were studied in this thesis with the chosen variables varied and provides a labeling system for easier visualization.

Table 5.1: Different Variation Conditions

Condition	Variable	Description
A	LET,x,W,N_{hits},A_{nuc}	All variables were varied. Only the physical beam parameters are known
B	LET,x,W,N_{hits}	Using 2 D microscopy for elimination of uncertainty in the area
C	LET,x,W	Addition of fluence measurement with FNTDs to eliminate uncertainty in nuclear hits
D	LET,W	Addition of 3D microscopy to eliminate uncertainty from chord length
E	W	Addition of perfect LET measurement with FNTDs. The case when energy loss straggling is the only unknown factor in the hybrid system

5.2 Experimental Basis

The experimental component of the "Cell Dose" model sets a framework for measuring the quantities specific dose and specific LET inside the cell nucleus using FNTDs as the model detector. Using the FTND track reconstruction method described in Section 3.2.2, the ion trajectories are fitted into a line in the 3D space using linear regression. The slope of the trajectory are obtained in both xz and yz directions. If z is the distance from the surface of FNTD to the cell layer and x_0 and y_0 are the positions of the ion trajectory at the surface, then the trajectory can be extrapolated to cell layer using the slopes x/z and y/z as follows:

$$x(z) = x_0 + \frac{x}{z} \cdot z \tag{5.20}$$

$$y(z) = x_0 + \frac{y}{z} \cdot z \tag{5.21}$$

After extrapolating each of the trajectories from FNTD into the cell layer, the LET of the tracks needs to be calculated. It has been previously been shown that the intensity of particle tracks is related to the LET of the track by a logarithmic function [79,80]. In

a recent version the following relationship between intensity I and the LET was used to convert the average intensity of each ion trajectory to an LET value:

$$LET_{track} = b \cdot (10^{\frac{I}{a}} - 1) \tag{5.22}$$

The parameters a and b, are chosen for each FNTD sample separately due to the sensitivity fluctuation of FNTDs. For each FNTD sample a Monte Carlo simulation of the irradiation condition at the the depth of study was performed. In a mixed particle field, the frequency distribution of the FNTD track intensities, when plotted as a histogram (Figure 5.6), usually exhibit two prominent peaks, one in a high intensity region and one in the low intensity region, representing primary ions and secondary fragments, respectively. A histogram of particle LET distribution also shows a similar distribution (Figure 5.6). The parameters a and b from equation 5.22 were chosen by matching the peaks of the primary ions and fragments with the peaks from Monte Carlo simulation, while optimizing for total dose and $\mathrm{LET_f}$ and $\mathrm{LET_d}$ of the primary particles.

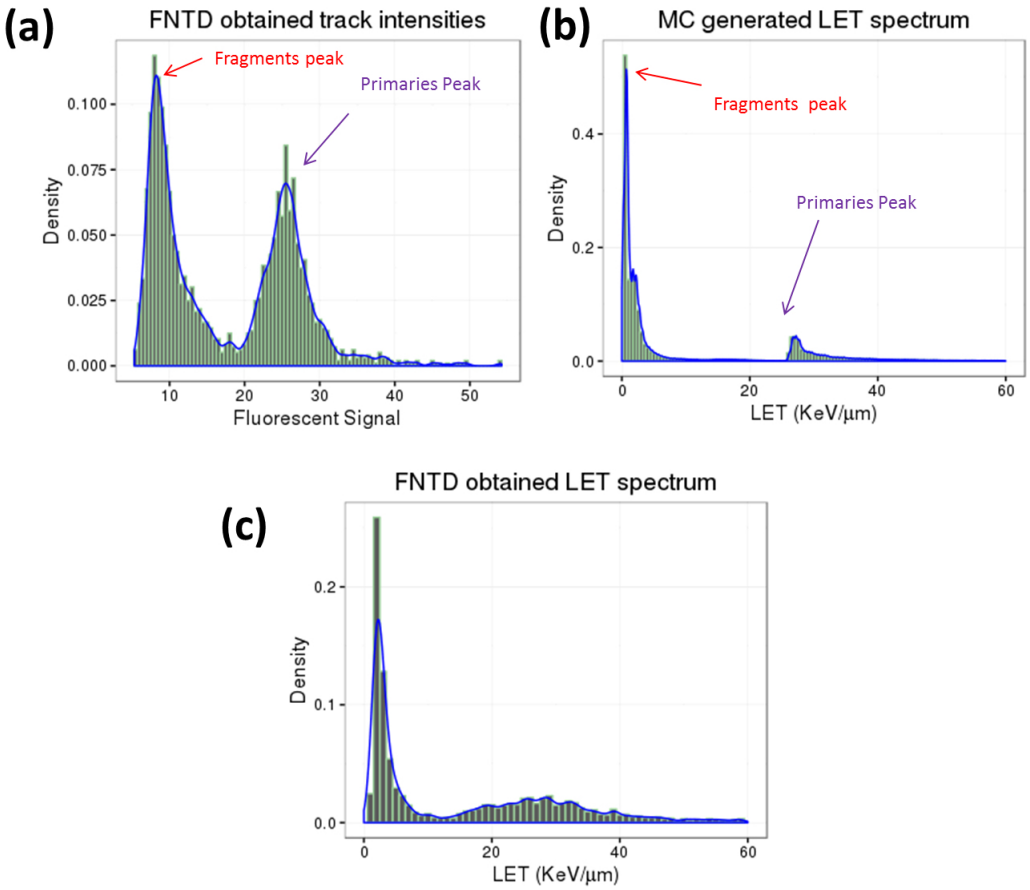

Figure 5.6: Process of converting intensity spectrum from FNTDs to a LET spectrum. In a mixed particle field, such as a mid-SOBP displayed here (sample SR308-8), the track intensities show two distinct distributions (a). The prominent peaks of these distributions can be matched to the peaks from MC generated spectra by optimizing the parameters a and b from equation 5.22 (b). Using equation 5.22, the intensity spectrum can be converted to a LET spectrum (C).

After converting each track intensity to an LET value and extrapolating the track to the cell layer, specific dose and specific LET can be calculated inside individual nuclei according to equations 5.18 and 5.19, respectively.

Chapter 6

Application of the New "Cell Dose" Framework

In this chapter, the application of the "Cell Dose" framework is presented. First, the results from the computational simulation are presented for carbon ion pristine Bragg peaks and physically and biologically optimized SOBPs in order to obtain information on different sources of variations. In specific, the cell dose quantities specific dose ($\tilde{D}_{nuc}$) and specific LET ($\tilde{L}_{nuc}$), along with their variation ($\hat{\sigma}$) are shown, including their variation on ion type, energy, depth and absorbed dose. Furthermore, contributions of different sources of variation are presented along with experimental measurements aiming for reduced uncertainty. Next, the results from experiments with FNTDs and cells are presented and compared with the simulation data to see how these values compare and in order to benchmark the framework.

6.1 Simulation Results Obtained from the "Cell Dose" Model with Carbon Ions

6.1.1 Pristine Bragg Peaks

Thee different monoenergetic carbon ion beams (with pristine Bragg peaks) were chosen to represent the therapeutic carbon ion beams available at HIT. They were simulated with the "Cell Dose" model to obtain the microscopic quantities and their variation at different depths (ranging from entrance to the tail region). The first energy chosen was 270.55 MeV/u corresponding to the experiment MN1000 and representing the mid range therapeutic energy at HIT. For comparison, two other energies were also simu-

lated including 91.1 MeV/u, representing the lower energy region, and 430.14 MeV/u, representing the high energy region. All three beams were simulated at 7-10 different depths, with absorbed dose optimized to 1 Gy at the Bragg peak. The 5 different variation conditions shown in Table 5.1 were also simulated for all the three energies. Furthermore, simulation of the Bragg peak position for variation in specific dose and specific LET were performed at different doses ranging from 0.5 Gy to 10 Gy to show the variability as a function of dose .

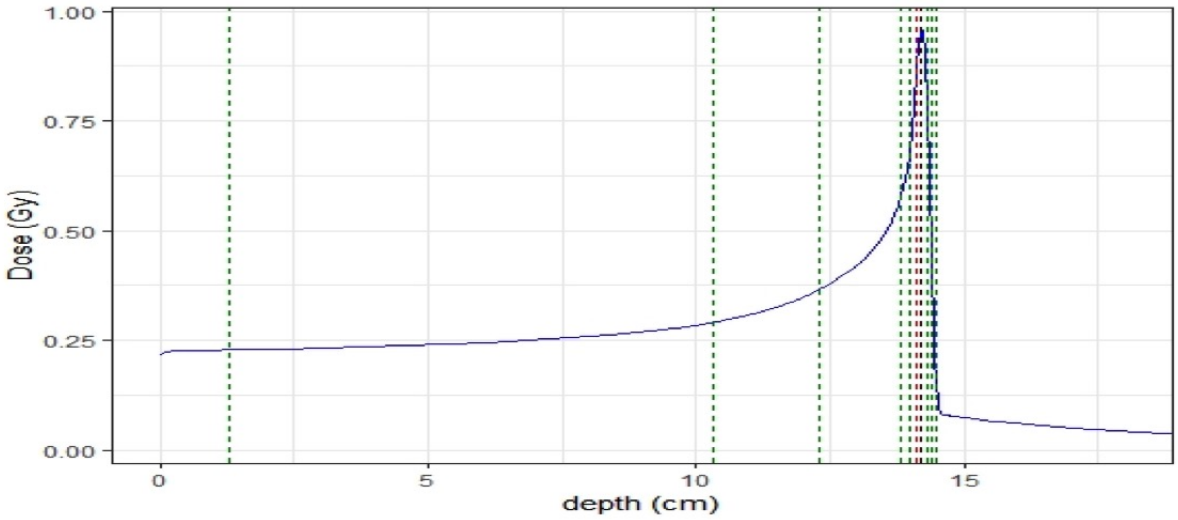

Figure 6.1: Depth-dose profile for the 270.55 MeV/u carbon ion. The vertical dashed lines represent the positions that were simulated.

Figure 6.1 shows the depth-dose profile for the 270.55 MeV/u carbon beam. The vertical dashed lines show the depth positions that were simulated. The vertical black dash line (at 14.2 cm) corresponds to the Bragg peak position, while the red dashed line (at 14.1 cm) represents the position used in the MN1000 experiment. As can be seen, multiple positions within 1 mm of the Bragg peak and the experimental position were also simulated to compare how positioning of the sample with a positioning error of 1 mm affects the measured values for specific dose and specific LET. Tables 6.1 and 6.2 summarize the results of the simulations using the "Cell Dose" model described in chapter 5 (as depicted in Figure 5.4) for all the 10 different positions shown in Figure 6.1 and for the 5 different variation conditions. Table 6.1 displays the results for specific dose, while Table 6.2 represents the results for specific LET. Figure 6.2 illustrates these results in a graphical representation in order to show the individual contribution of each source of variation to the overall variation in specific dose and specific LET.

Table 6.1: Comparison of variation in specific dose for 5 different variation conditions of a 270 MeV/u Carbon ion beam at different depths

Depth (cm)	Condition	Specific Dose variation (%)					$\overline{\tilde{D}_{nuc}}$ (Gy)	D_{phys}(Gy)
		A	B	C	D	E		
1.3		29.7 ± 0.8	26.6 ± 0.6	14.1 ± 0.4	11.3 ± 0.3	10.3 ± 0.4	0.23± 0.01	0.23
10.3		31.5 ± 1.0	28.0 ± 0.6	18.5 ± 0.4	16.1 ± 0.3	7.2 ± 0.3	0.28± 0.04	0.29
12.3		32.6 ± 1.1	29.1 ± 0.8	21.3 ± 0.8	19.3 ± 0.6	6.3 ± 0.6	0.36± 0.01	0.37
13.8		34.3 ± 1.1	30.7 ± 0.7	23.1 ± 0.6	20.8 ± 0.5	5.5 ± 1.4	0.55 ± 0.10	0.57
14.0		35.6 ± 1.1	32.0 ± 0.8	24.6 ± 0.7	22.1 ± 0.5	5.3 ± 0.6	0.66 ± 0.20	0.68
14.1		38.2 ± 1.1	34.4 ± 0.9	27.7 ± 0.7	25.1 ± 0.6	5.2 ± 0.8	0.84 ± 0.20	0.87
14.2		44.8 ± 1.2	40.1 ±1.0	34.3 ± 0.9	31.5 ± 0.8	6.2 ± 2.3	0.96 ± 0.20	1.0
14.3		54.6 ± 1.6	48.6 ± 1.3	43.2 ± 1.0	39.9 ± 1.0	9.0 ± 6.4	0.84 ± 0.03	0.87
14.4		84.5 ± 3.0	75.8 ± 1.7	71.0 ± 1.7	66.4 ± 1.7	15.5 ± 10.9	0.39 ± 0.20	0.44
14.5		117.5 ± 7.4	104.0 ± 3.4	100.8 ±3.3	94.3 ±2.5	16.2 ± 24.2	0.11 ± 0.10	0.12

Table 6.2: Comparison of variation in specific LET for 5 different variation conditions of a 270 MeV/u Carbon ion beam at different depths

Depth (cm)	Condition	Specific LET variation (%)					$\overline{\tilde{L}_{nuc}}$ (Gy)	LET_f ($keV/\mu m$)	LET_d ($keV/\mu m$)
		A	B	C	D	E			
1.3		13.8 ± 0.8	11.9 ± 0.3	11.5 ± 0.3	11.3 ± 0.3	10.3 ± 0.4	13.1± 0.2	13.3	14.1
10.3		20.3 ± 0.7	17.4 ± 0.4	17.0 ± 0.4	16.1 ± 0.3	7.2 ± 0.3	14.1± 0.2	14.6	22.0
12.3		23.4 ± 1.3	20.5 ± 0.9	20.1 ± 0.8	19.3 ± 0.6	6.3 ± 0.6	16.2± 0.01	16.5	31.1
13.8		25.8 ± 1.2	22.6 ± 0.5	22.0 ± 0.6	20.8 ± 0.5	5.5 ± 1.4	25.9 ± 0.2	26.5	57.9
14.0		27.0 ± 0.8	24.1 ± 0.7	23.5 ± 0.6	22.1 ± 0.5	5.3 ± 0.6	31.8 ± 0.3	32.5	75.3
14.1		30.5 ± 1.4	27.0± 0.7	26.6 ± 0.7	25.1 ± 0.6	5.2 ± 0.8	39.0 ± 0.4	40.1	103.2
14.2		38.3 ± 1.6	33.9 ± 0.8	33.5 ± 0.8	31.5 ± 0.8	6.2 ± 2.3	48.1 ± 0.6	50.8	173.6
14.3		48.7 ± 1.9	43.3 ± 1.1	42.5 ± 1.1	39.9 ± 1.0	9.0 ± 6.4	44.3 ± 0.4	48.3	219.3
14.4		82.4 ± 2.7	73.2 ± 1.9	70.3 ± 1.7	66.4 ± 1.7	15.5 ± 10.9	31.5 ± 1.0	35.9	286.2
14.5		116.7 ± 9.2	103.6 ± 3.7	100.4 ±3.3	94.3 ±2.5	16.2 ± 24.2	7.0 ± 0.2	8.2	219.7

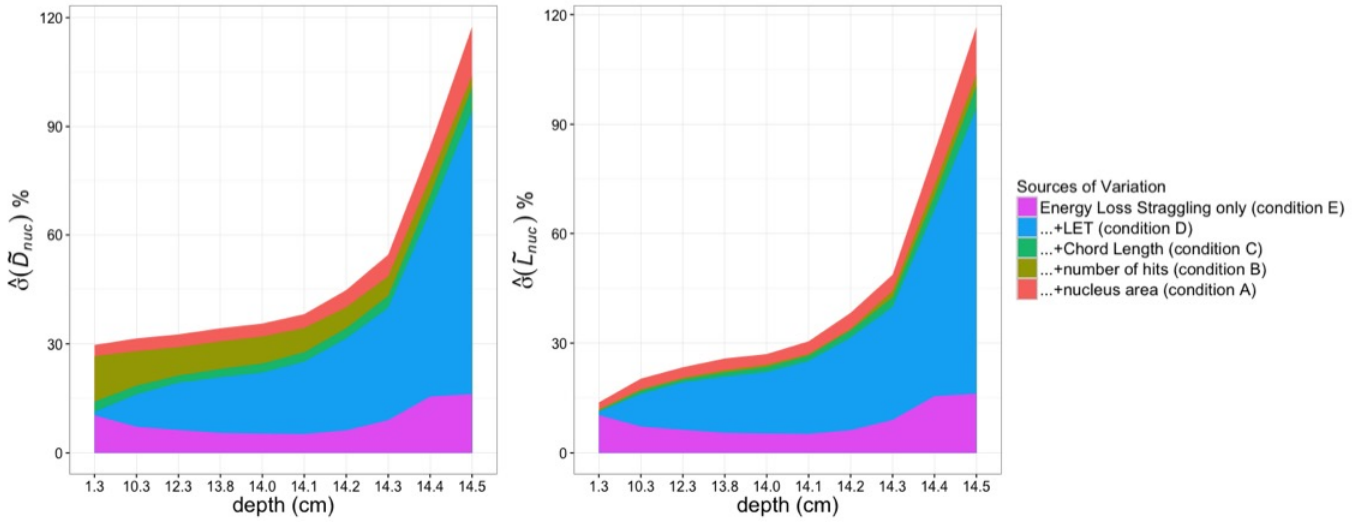

Figure 6.2: Contribution of different sources of variation to D_{nuc} and L_{nuc} for 270.55 MeV/u carbon ion at different depths.

As can be seen from Table 6.1 and Figure 6.2, for the case that all sources are varied (condition A), the variation in specific dose in the entrance region is around 30% and rises up to 44.8% at the Bragg peak. Just 1 mm before the Bragg peak in the rising flank (where the MN1000 experiment was conducted) this variation is around 6 percentage points lower, with specific dose being 0.12 Gy lower. At just 1 mm after the Brag peak the variation increases to around 55% , with a decrease of 0.12 Gy in the specific dose. A significant increase in specific dose variation is observed right after the dose fall off, reaching as high as 84.5% and 117.5% in the tail region. Table 6.1 also shows that specific dose follows the absorbed dose throughout the depth-dose profile, while being slightly lower than the absorbed dose at further depths.
As for $\tilde{L}_{nuc}$ (as shown in Table 6.2 and Figure 6.2), a similar pattern of increased variation form the entrance region to the Bragg peak and finally to the tail region is observed. However, $\hat{\sigma}(\tilde{L}_{nuc})$ is about half of $\hat{\sigma}(\tilde{D}_{nuc})$ in the entrance region (13.8% as compared to 29.7%), and reaches comparable magnitudes to $\hat{\sigma}(\tilde{D}_{nuc})$ around the Bragg Peak region and further in the tail region.

In addition to showing the variation in specific dose and specific LET in a large cell population, Tables 6.1 and 6.2 demonstrate how addition of microscopy and FNTD measurements can reduce uncertainty in measuring individual "Cell Dose" values in each cell at different depths, and how each source of variation contributes to the overall

variation. As can be seen from these tables, addition of 2D microscopy to reduce the uncertainty in the nuclear area reduces the measured variation in specific dose and LET about 2-3 percentage points in the entrance region and around 4-6 percentage points around the Bragg peak region, and up to 10-13 percentage points in the dose fall off and tail regions. Measuring additionally the number of hits to the nucleus using FNTDs (condition C), significantly reduces $\hat{\sigma}(\tilde{D}_{nuc})$ from 29.7% to 14.1% in the entrance. However, with further depths in water and around the Bragg peak this reduction is less significant and $\hat{\sigma}(\tilde{D}_{nuc})$ is reduced by around 7 percentage points in the Bragg region and to around 4 percentage points in the tail region. For condition C, $\hat{\sigma}(\tilde{L}_{nuc})$ reduction is not very significant and is less than 1 percentage point at all depths. Further addition of 3D cell microscopy to reduce uncertainty arising from chord lengths of particles inside the cell nucleus (condition D) reduces the uncertainty by 2-6 percentage points in $\hat{\sigma}(\tilde{D}_{nuc})$ and 0.2-6 percentage points in $\hat{\sigma}(\tilde{L}_{nuc})$.
The most significant decrease in $\hat{\sigma}(\tilde{D}_{nuc})$ and $\hat{\sigma}(\tilde{L}_{nuc})$ is achieved when information about track LET is provided from FNTD measurements (going from condition D to E) in the Bragg peak region and the tail area. When this condition is realized, the only uncertainty in energy deposition measurement arises from energy loss straggling, and is the same uncertainty obtained for both specific dose and specific LET which is in the range of 5.2-16.2%. As can be seen from Figure 6.2, as the depth increases, LET variation contributes more and more to the total variation in specific dose and specific LET, and dominating the uncertainty in the tail region.

As mentioned previously, to compare the "Cell Dose" quantities for different ion beam energies, 91.1 MeV/u and 430.14 MeV/u carbon ion beams were also simulated. The depth-dose profiles indicating the simulated position and the corresponding results tables for variation in specific dose and specific LET are shown in Appendix A. For visualization and comparison, the graphical representation of the results, are shown here in Figures 6.3 and 6.4. As can be seen in Figure 6.3, the contribution of different sources at relative depths compared to the Bragg peak is very similar for 91.1 MeV/u and 270.55 MeV/u carbon ions. The total variations are also within similar range, with each source contributing a similar value to the total variation; that is with the chord length contributing the least at all depths and number of hits contributing the most in the entrance region and the LET dominating the variation at Bragg peak and the tail region. While a similar pattern and comparable values are also observed with 430.1 MeV/u carbon ions (Figure 6.4) , there is a significant difference towards the tail region behind the Bragg peak, where the overall variation in specific dose and specific LET

slightly decreases.

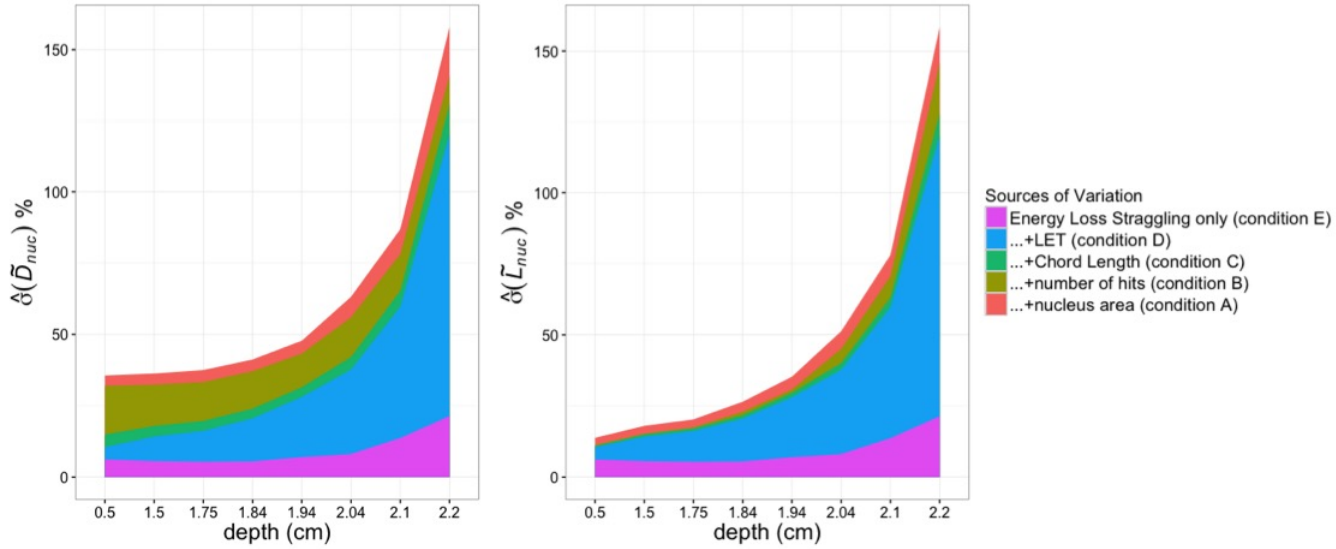

Figure 6.3: Contribution of different sources of variation to D_{nuc} and L_{nuc} for 91.1 MeV/u carbon ion at different depths.

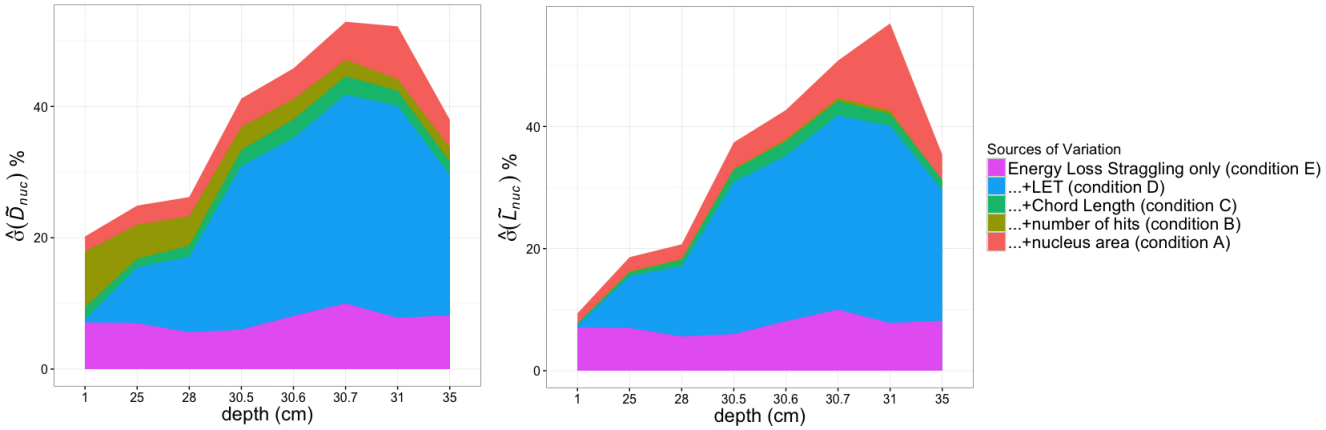

Figure 6.4: Contribution of different sources of variation to $\tilde{D}_{nuc}$ and $\tilde{L}_{nuc}$ for 430.14 MeV/u carbon ion at different depths.

To show how the overall variation varies with absorbed dose, specific dose and specific LET variation were simulated from 0.5 Gy to 10 Gy for the three different energies at the Bragg peak position. The results are shown in Figure 6.5 . As can be seen from this figure, the variation in specific dose is almost the same for all three energies (error bars not shown). The variation in specific dose at 0.5 Gy is about 65% and decreases down to around 15% at 10 Gy. As for specific LET, while the variations are close, there is

a slight difference, with higher energies exhibiting a variation, a few percentage points higher as compared to lower energies, but follows the same trend as the variation in specific dose.

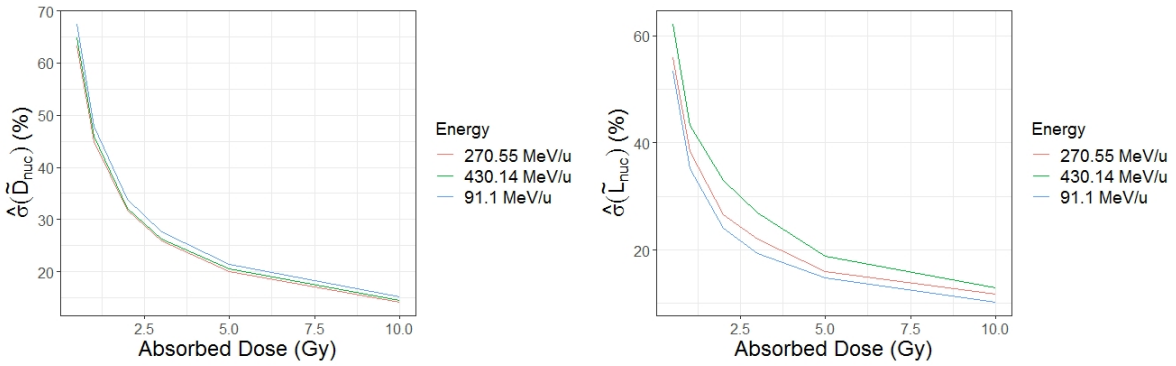

Figure 6.5: Comparison of specific dose and specific dose variation as a function of dose at the Bragg Peak for three different carbon ion energies.

6.1.2 Physically Optimized Spread out Bragg Peak

As was shown in the previous section, a slight (1 mm) positioning variation around the Bragg Peak can result in a difference of around 15% decrease in absorbed dose and specific dose values. Therefore, to eliminate this significant error in D and D_{nuc} measurements, it is preferred to use a SOBP plan as the maximum dose is nearly constant in a wider range. To compare the specific dose and specific LET variation for carbon ion SOBPs, the SOBP plans for the two experiments of SINF and MN81000/MN12000 were used. The positions chosen, represent the entrance channel, different positions of the SOBP (proximal, mid and distal points) to see how the values vary within the same absorbed dose, and the tail region. The plans are shown for the SOBP plateau optimized to 1 Gy absorbed dose. As before, the vertical dashed lines show the depths, where the simulations were carried out. Here, the red dashed lines shows the mid-SOBP, while the black dashed lines show the positions of the FNTDs in the experiments.

Figure 6.6 shows the SOBP plan for MN81000 experiment, which is optimized for 1 Gy at SOBP. The same plan was also used for MN12000 experiment, but optimized for 0.5 Gy at SOBP. Tables 6.3 and 6.4 show the results of simulations for specific dose and specific LET, respectively. Figure 6.7 shows these results graphically, showing individual contributions of sources of variations in different colors. As can be seen, the variation in specific dose is about 25% at the entrance channel and increases slightly to

about 28% at the beginning of the SOBP, 30% at mid-SOBP (where the measurements were done), and 38% at the distal edge of the SOBP. Therefore, from the proximal end to the distal end of SOBP there is 10 percentage points increase in the specific dose variation. The highest variation in $\tilde{D}_{nuc}$ is observed at the tail of the SOBP with a variation of close to 100%. As for specific LET, a similar pattern of increased variation is observed. However, as similar to the case of pristine Bragg peaks, in the entrance region $\hat{\sigma}(\tilde{L}_{nuc})$ is around half of what is observed from $\hat{\sigma}(\tilde{D}_{nuc})$ at around 10% and reaches comparable magnitudes at the end of the SOBP and the tail region.
Figure 6.7 shows how each source contributes to total variation. As observed, the number of hits dominates the variation in the entrance channel and its effect decreases in depth. In the SOBP plateau and the tail region, LET dominates the variation for specific dose. However, for specific LET, the number of hits only contributes a few percentage points and straggling and LET are dominant in the entrance, with LET dominating as the depth increases.

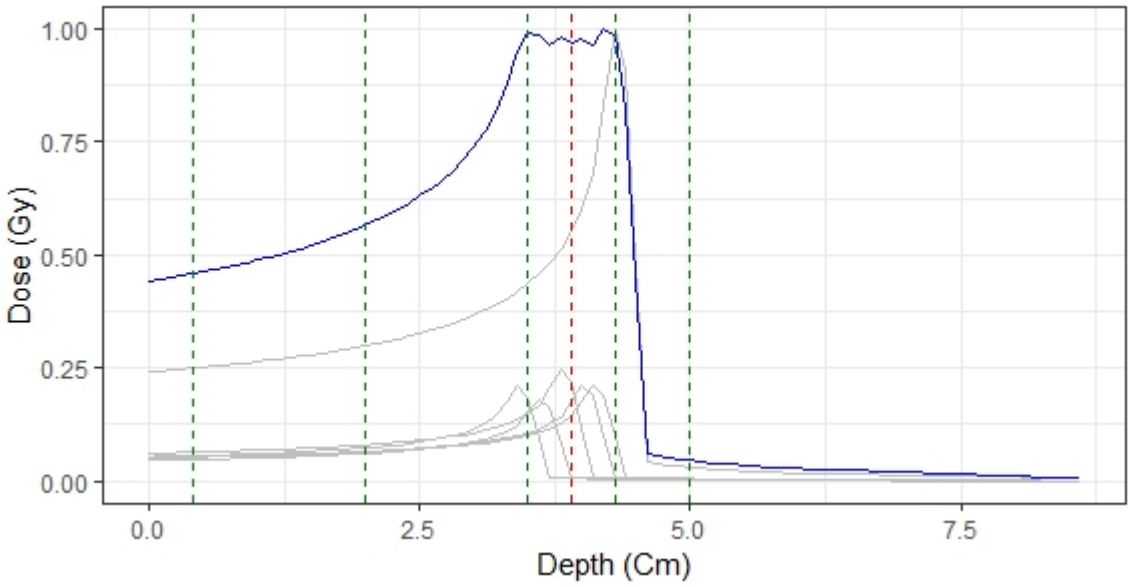

Figure 6.6: Depth-dose profile for SOBP plan corresponding to MN81000 experiment. The vertical dashed lines represent the positions that were simulated.

Table 6.3: Comparison of variation in specific dose for 5 different variation conditions at different position of a SOBP plan corresponding to MN81000 experiment

		Specific Dose variation (%)						
Depth (cm)	Condition	A	B	C	D	E	$\overline{\tilde{D}_{nuc}}$ (Gy)	D_{phys}(Gy)
0.4		25.8 ± 0.7	23.0 ± 0.5	11.0 ± 0.3	8.0 ± 0.2	5.5 ± 0.2	0.45 ± 0.01	0.46
2.0		25.2 ± 0.7	22.6 ± 0.4	13.6 ± 0.3	10.8 ± 0.3	5.0 ± 0.3	0.56 ± 0.01	0.57
3.5		27.9 ± 0.8	24.8 ± 0.6	17.7 ± 0.4	15.7 ± 0.4	4.1 ± 0.3	0.98 ± 0.01	1.0
3.9		30.7 ± 0.9	27.2 ± 0.6	19.9 ± 0.4	17.7 ± 0.4	4.6 ± 0.5	0.95 ± 0.02	0.97
4.3		37.8 ± 1.2	34.0 ± 0.9	29.1 ± 0.7	26.7 ± 0.7	6.3 ± 3.9	0.95 ± 0.02	0.99
5.0		99.9 ± 9.2	87.2 ± 6.2	80.4 ± 6.1	75.9 ± 4.1	15.1 ± 8.9	0.04 ± 0.01	0.05

Table 6.4: Comparison of variation in specific LET for 5 different variation conditions at different position of a SOBP plan corresponding to MN81000 experiment

		Radiation quality variation (%)							
Depth (cm)	Condition	A	B	C	D	E	$\overline{\tilde{L}_{nuc}}$ (Gy)	LET_f ($keV/\mu m$)	LET_d ($keV/\mu m$)
0.4		10.2 ± 0.6	8.4 ± 0.2	8.3 ± 0.2	8.0 ± 0.2	5.5 ± 0.2	21.1 ± 0.1	21.6	23.4
2.0		13.4 ± 0.5	11.5 ± 0.2	11.4 ± 0.3	10.8 ± 0.3	5.0 ± 0.3	21.7 ± 0.1	22.1	29.0
3.5		19.1 ± 0.7	16.9 ± 0.4	16.5 ± 0.4	15.7 ± 0.4	4.1 ± 0.3	33.8 ± 0.2	34.4	62.3
3.9		21.8 ± 0.7	19.2 ± 0.4	18.8 ± 0.4	17.7 ± 0.4	4.6 ± 0.5	37.5 ± 0.3	38.6	79.2
4.3		32.2 ± 1.2	28.8 ± 0.8	28.3 ± 0.7	26.7 ± 0.7	6.3 ± 3.9	32.4 ± 0.3	35.5	141.5
5.0		99.5 ± 17.5	86.5 ± 8.9	79.6 ± 6.1	75.9 ± 4.1	15.1 ± 8.9	4.8 ± 0.1	5.4	80.4

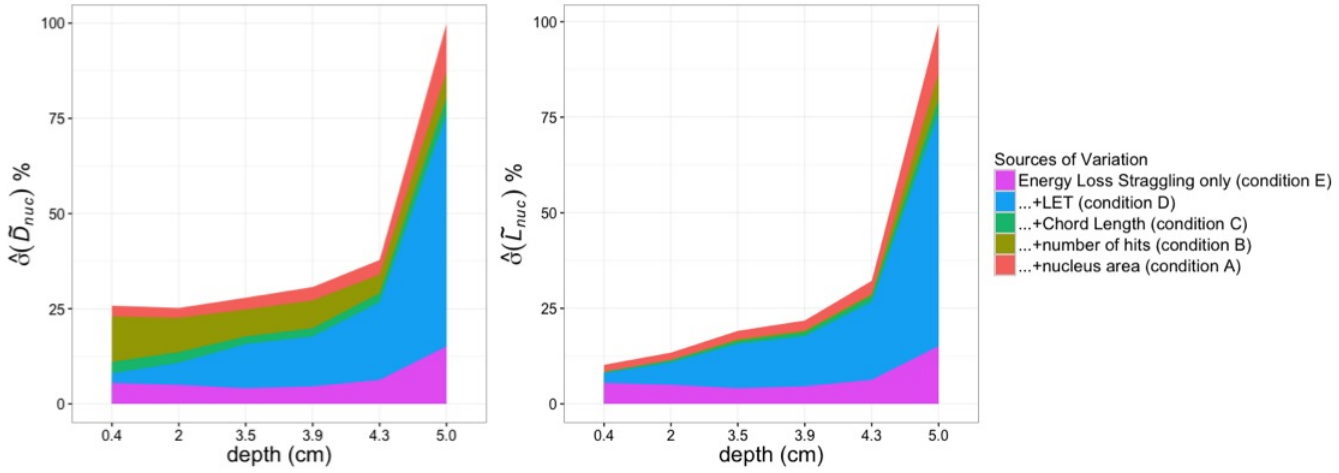

Figure 6.7: Contribution of different sources of variation to $\tilde{D}_{nuc}$ and $\tilde{L}_{nuc}$ for different position of a SOBP plan corresponding to MN81000 experiment

Since this plan was used at both 0.5 Gy and 1 Gy at mid-SOBP, the contribution of

the sources to the total variation are shown for mid-SOBP (3.9 cm) in Figure 6.8 for the two different doses. As can be seen from this figure, total variation in specific dose increases about 15 percentage points when going from 1 Gy to 0.5 Gy and about 10 percentage points for variation in specific LET. As can be seen seen at mid-SOBP for both doses, the LET contributes the most to $\hat{\sigma}(\tilde{D}_{nuc})$, followed by number of hits and then straggling, and the area and chord lengths only contribute a few percentage points. For $\hat{\sigma}(\tilde{L}_{nuc})$, LET contributes the most, while the number of hits has the least significance and contributing less than 1 percentage point. In the condition when FNTDs and 3D microscopy are used to eliminate all possible source of uncertainty (condition E), the uncertainty in the measurement arising from energy loss straggling which can not be measured inside the cell with current experimental equipment equals to around 6.3% for 0.5 Gy and 4.6% for 1 Gy at mid-SOBP for both $\hat{\sigma}(\tilde{D}_{nuc})$ and $\hat{\sigma}(\tilde{L}_{nuc})$.

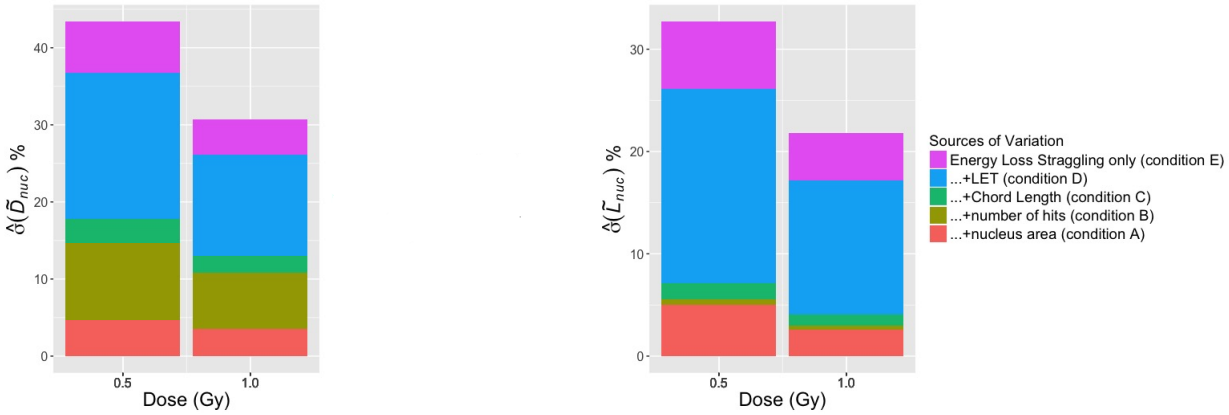

Figure 6.8: Contribution of different sources of variation to $\tilde{D}_{nuc}$ and $\tilde{L}_{nuc}$ at mid-SOBP, corresponding to MN12000 (O.5 Gy) and MN81000 (1 Gy) experiments

The other SOBP plan that was simulated with the "Cell Dose" model is the SOBP plan used for the SINF experiment. The SOBP plan optimized at 1 Gy SOBP in the plateau depths of 4-8 cm is shown in figure 6.9. Again, the vertical red dashed lines show the depths that the experiments were carried out and the black dashed line shows the mid-SOBP position. The results for specific dose and specific LET are shown in Tables 6.5 and 6.6, respectively. Figure 6.10 illustrates the results in a graphical representation showing the individual contributions of each source of variation. The values for $\hat{\sigma}(\tilde{D}_{nuc})$ from the proximal to mid-SOBP to distal edge resembles the same values as the MN81000 experiments, with similar values of individual sources of variation. However, the tail the $\hat{\sigma}(\tilde{D}_{nuc})$ is around 55%, which is about half the value of the tail

region of the MN81000 experiment. $\hat{\sigma}(\tilde{L}_{nuc})$ also follows a similar pattern.

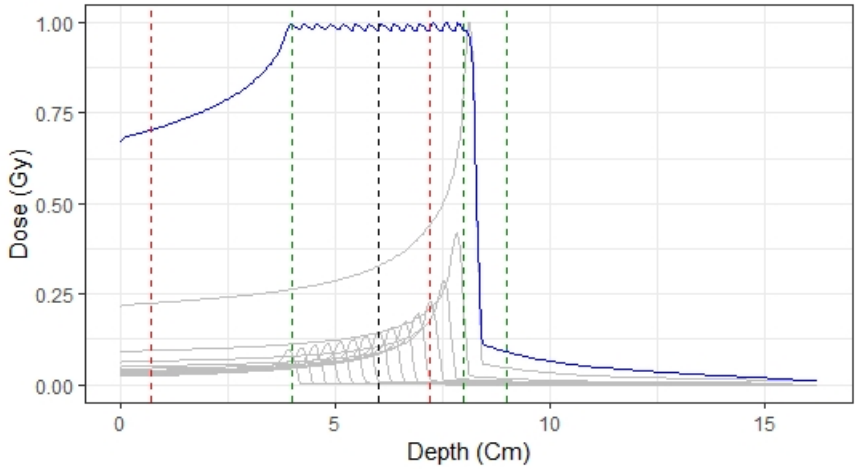

Figure 6.9: Depth-dose profile for SOBP plan corresponding to the SINF experiment. The vertical dashed lines represent the positions that were simulated.

Table 6.5: Comparison of variation in specific dose for 5 different variation conditions at different position of a SOBP plan corresponding to the SINF experiments

		Specific Dose variation (%)						
Depth (cm)	Condition	A	B	C	D	E	$\overline{\tilde{D}_{nuc}}$ (Gy)	D_{phys}(Gy)
0.7		19.3 ± 0.6	17.2 ± 0.4	8.2 ± 0.2	6.3 ± 0.1	5.4 ± 0.2	0.70 ± 0.01	0.70
4.0		23.3 ± 0.7	21.0 ± 0.5	16.1 ± 0.5	14.6 ± 0.5	4.2 ± 0.3	0.97 ± 0.01	1.0
6.0		25.4 ± 0.8	22.9 ± 0.6	18.2 ± 0.6	16.6 ± 0.5	4.1 ± 0.4	0.97 ± 0.01	0.98
7.2		28.2 ± 1.0	25.2 ± 0.7	20.7 ± 0.4	18.8 ± 0.5	4.1 ± 0.3	0.96 ± 0.02	0.98
8.0		38.5 ± 1.4	34.5 ± 0.8	29.9 ± 0.7	27.6 ± 0.6	5.6 ± 2.1	0.95 ± 0.02	0.98
9.0		58.4 ± 3.8	51.7 ± 2.1	47.7 ± 2.0	44.3 ± 1.8	10.3 ± 2.4	0.08 ± 0.01	0.09

Table 6.6: Comparison of variation in specific LET for 5 different variation conditions at different position of a SOBP plan corresponding to the SINF experiments

Depth (cm)	Condition	Radiation quality variation (%)					$\overline{\tilde{L}_{nuc}}$ (Gy)	LET_f ($keV/\mu m$)	LET_d ($keV/\mu m$)
		A	B	C	D	E			
0.7		7.7 ± 0.3	6.4 ± 0.2	6.3 ± 0.2	6.3 ± 0.1	5.4 ± 0.2	17.7 ± 0.1	18.0	19.0
4.0		17.3 ± 1.0	15.6 ± 0.5	15.4 ± 0.5	14.6 ± 0.5	4.2 ± 0.3	19.7 ± 0.1	20.3	44.4
6.0		20.0 ± 1.1	18.0 ± 0.6	17.6 ± 0.6	16.6 ± 0.5	4.1 ± 0.4	20.6 ± 0.1	20.9	53.0
7.2		22.5 ± 0.9	20.1 ± 0.6	20.0 ± 0.5	18.8 ± 0.5	4.1 ± 0.3	23.7 ± 0.2	24.2	64.6
8.0		33.5 ± 1.2	29.7 ± 0.7	29.3 ± 0.7	27.6 ± 0.6	5.6 ± 2.1	31.0 ± 0.3	32.2	129.7
9.0		54.7 ± 4.0	47.8 ± 2.5	47.2 ± 2.0	44.3 ± 1.8	10.3 ± 2.4	4.1 ± 0.1	4.5	64.1

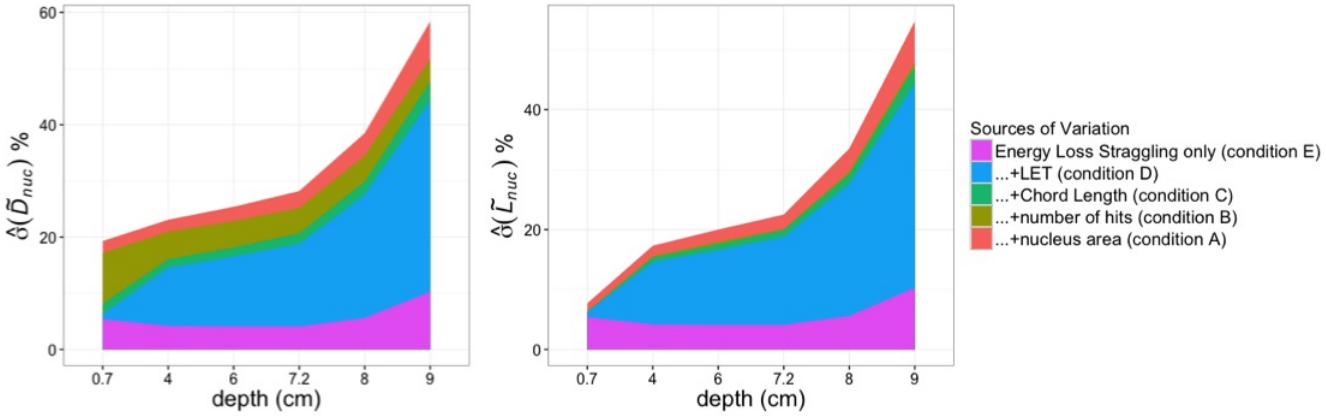

Figure 6.10: Contribution of different sources of variation to $\tilde{D}_{nuc}$ and $\tilde{L}_{nuc}$ for SINF SOBP plan.

6.1.3 Biologically Optimized Spread out Bragg Peak

The biologically optimized spread out Bragg peak condition is the case, that was published [74], resulting from the work of this thesis. For this case, the irradiation with FNTDs (experiment SR308) was done for all the depths simulated in order to have a complete measurement and simulation data. The purpose of choosing a biologically optimized SOBP was to see, how the "Cell Dose" quantities and their variation compare when the RBE-weighted dose is constant. For this purpose a RBE-weighted dose of 2 Gy(RBE) for the SOBP plateau was chosen, and the plan was optimized accordingly. Figure 6.11 shows the plan for this biologically optimized SOBP. As can be seen from the figure the absorbed dose in the SOBP plateau is about 0.5 Gy at the proximal end and decreases slightly toward the distal end. Tables 6.7 and 6.8 show the results for specific dose and specific LET, respectively. For this case, the variation in specific dose

is around 24-25% in the entrance region, increases to 30.3% at the beginning of the SOBP at 10.75 cm depth and further increases to 53.5% at the distal edge of the SOBP at 14.75 cm. Thus, an increase of 20 percentage points is observed from the proximal end to the distal end. The highest $\hat{\sigma}(\tilde{D}_{nuc})$ of 58.2% is observed at the tail region at 17.75 cm. Similar to the other SOBP cases, $\hat{\sigma}(\tilde{D}_{nuc})$ shows similar pattern of increase with depth, starting about half of the $\hat{\sigma}(\tilde{D}_{nuc})$ at entrance channel (12.7% as compared to 24.3%), then reaching comparable magnitudes around mid-SOBP and tail regions. Figure 6.12 depicts the result graphically, showing how individual sources contribute to overall variation. The contribution of the individual sources are similar to the cases of the physical SOBP, again with LET dominating the variation for both $\tilde{D}_{nuc}$ and $\tilde{L}_{nuc}$ at SOBP and tail region.

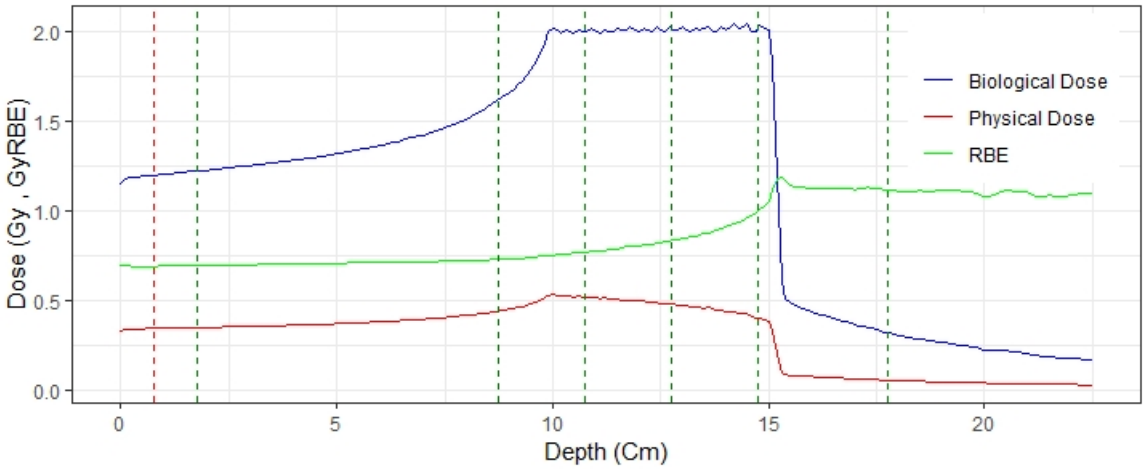

Figure 6.11: Biologically optimized SOBP corresponding to SR308 experiment

Table 6.7: Comparison of variation in specific dose for 5 different variation conditions at different positions for 2 Gy biologically optimized C-12 SOBP

		Specific Dose variation (%)						
Depth (cm)	Condition	A	B	C	D	E	$\overline{\tilde{D}_{nuc}}$ (Gy)	D_{phys}(Gy)
0.75		24.2 ± 0.7	21.7 ± 0.5	12.7 ± 0.3	10.6 ± 0.3	7.6 ± 0.3	0.34 ± 0.01	0.35
1.75		24.3 ± 0.6	21.7 ± 0.6	14.3 ± 0.3	12.4 ± 0.3	7.8 ± 0.4	0.35 ± 0.01	0.35
8.75		25.0 ± 0.8	22.4 ± 0.6	18.3 ± 0.5	16.9 ± 0.4	6.4 ± 0.5	0.43 ± 0.01	0.44
10.75		30.3 ± 1.2	27.3 ± 0.7	23.8 ± 0.7	22.1 ± 0.6	5.8 ± 1.2	0.52 ± 0.01	0.53
12.75		36.9 ± 1.8	33 ± 1.0	30.1 ± 1.0	28.1 ± 0.7	6.6 ± 3.1	0.47 ± 0.01	0.48
14.75		53.3 ± 1.9	48.2 ± 1.3	45.7 ± 1.3	42.8 ± 1.1	7.6 ± 2.6	0.39 ± 0.01	0.40
17.75		57.8 ± 6.2	50.9 ± 3.4	48.5 ± 3.8	44.9 ± 3.1	11.5 ± 1.4	0.06 ± 0.01	0.06

Table 6.8: Comparison of variation in specific dose for 5 different variation conditions at different positions for 2 Gy biologically optimized C-12 SOBP

Depth (cm)	Condition	Specific LET variation (%)					$\overline{\tilde{L}_{nuc}}$ (Gy)	LET_f ($keV/\mu m$)	LET_d ($keV/\mu m$)
		A	B	C	D	E			
0.75		12.7 ± 0.7	11.1 ± 0.3	10.9 ± 0.3	10.6 ± 0.3	7.6 ± 0.3	12.2 ± 0.2	12.3	14.0
1.75		15.1 ± 0.7	13.1 ± 0.4	12.9 ± 0.4	12.4 ± 0.3	7.8 ± 0.4	10.7 ± 0.2	10.8	14.3
8.75		20.2 ± 0.9	17.8 ± 0.7	17.7 ± 0.5	16.9 ± 0.4	6.4 ± 0.5	8.5 ± 0.2	8.6	20.7
10.75		28.7 ± 1.0	25.6 ± 0.7	25.3 ± 0.7	22.1 ± 0.6	5.8 ± 1.2	9.9 ± 0.2	10.0	44.4
12.75		33.4 ± 1.2	29.9 ± 1.0	29.7 ± 1.0	28.1 ± 0.7	6.6 ± 3.1	10.1 ± 0.3	10.3	54.8
14.75		51.4 ± 1.8	45.7 ± 1.3	45.3 ± 1.2	42.8 ± 1.1	7.6 ± 2.6	10.5 ± 0.2	10.5	98.5
17.75		55.8 ± 3.2	48.7 ± 3.4	47.9 ± 3.1	44.9 ± 3.1	11.5 ± 1.4	2.13 ± 0.2	2.21	15.1

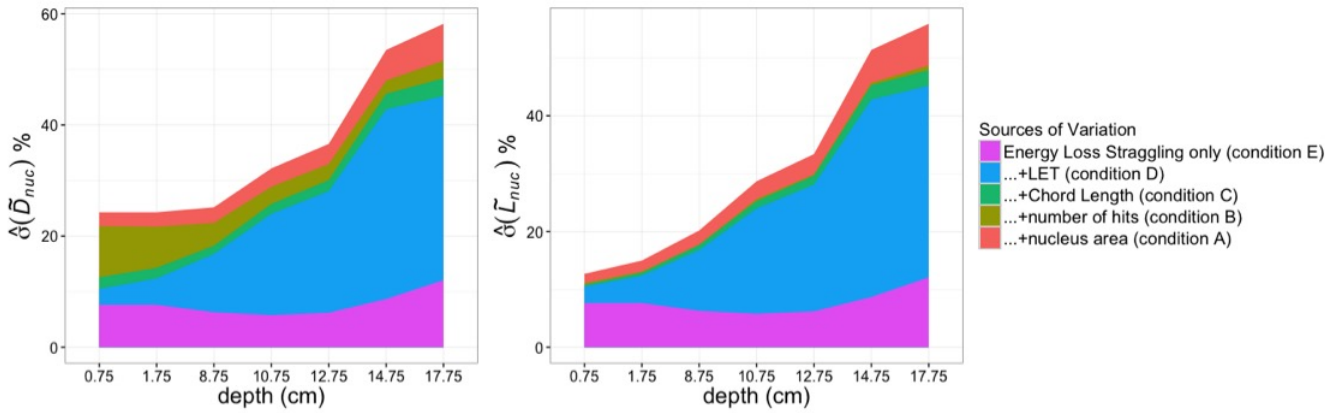

Figure 6.12: Contribution of different sources of variation to $\tilde{D}_{nuc}$ and $\tilde{L}_{nuc}$ for 2 Gy biologically optimized SOBP plan

6.1.4 Comparison of "Cell Dose" Quantities of Different Ion Types

In order to compare different ion types in terms of "Cell Dose" variation, three different SOBPs (optimized to 1 Gy absorbed dose) including proton, helium and carbon were simulated at the entrance region, mid-SOBP and the tail region. The result of this comparison is shown in Table 6.9. As can be seen from this table, $\hat{\sigma}(\tilde{D}_{nuc})$ for the proton SOBP is significantly less than carbon ion at all depths (around 1/4 less in the entrance and SOBP and 1/6 less in the tail), while helium has values between carbon and proton (around half of carbon ions). A similar increase from proton to helium to carbon ions is also seen with $\hat{\sigma}(\tilde{L}_{nuc})$. However, the significance is lower in the entrance region, and becomes prominent in the mid-SOBP and the tail region.

Table 6.9: Comparison of different ion types for variation in specific dose and specific LET

	Entrance Channel		mid-SOBP		tail	
Primary ion	$\hat{\sigma}(\tilde{D}_{nuc})$ [%]	$\hat{\sigma}(\tilde{L}_{nuc})$ [%]	$\hat{\sigma}(\tilde{D}_{nuc})$ [%]	$\hat{\sigma}(\tilde{L}_{nuc})$ [%]	$\hat{\sigma}(\tilde{D}_{nuc})$ [%]	$\hat{\sigma}(\tilde{L}_{nuc})$ [%]
Proton	5.2	3.9	7.3	4.2	10.3	7.5
Helium	9.2	5.5	12.2	8.2	19.4	17.3
Carbon	19.3	7.7	25.4	22.5	58.4	54.7

Furthermore, the variation in specific dose was compared for mid-SOBP position of 2 Gy(RBE) biologically optimized SOBP plans for proton and carbon ions. Figure 6.13 shows the distribution of specific dose for these two mid-SOBPs. As can can be seen, the variation in D_{nuc} is 34.1% for carbon ions while for the proton irradiation it is only 4.1%. This difference can be attributed to the fact that larger proton fluence is required to achieve the same absorbed dose, let alone the same biological dose which is around four times higher.

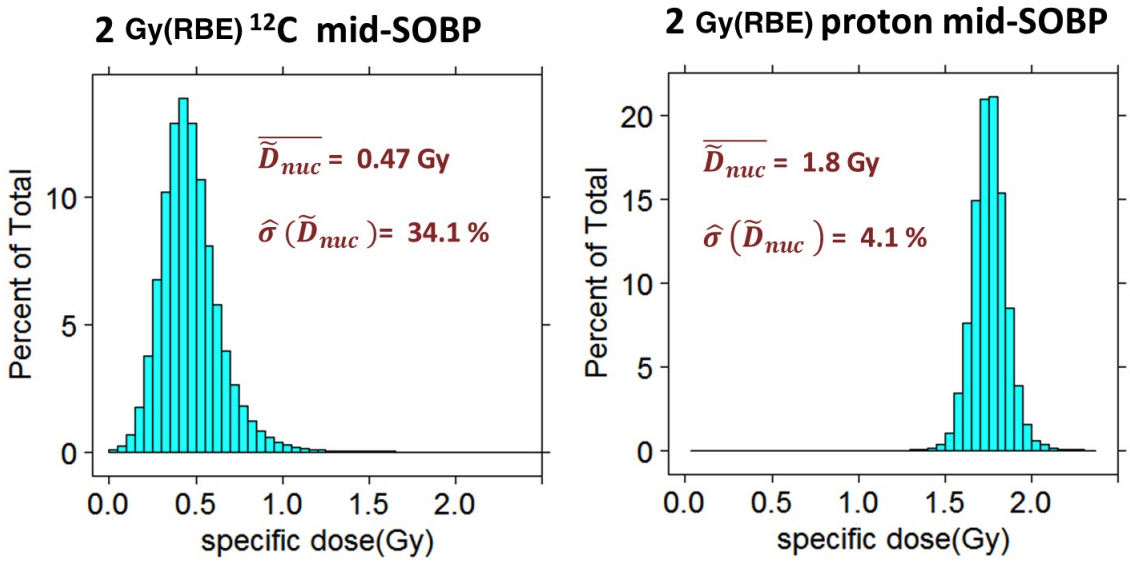

Figure 6.13: Comparison of specific dose distribution at mid-SOBP for carbon ions (left) and protons (right)

6.2 Experimental Results

6.2.1 Pristine Bragg Peak

MN1000 Experiment Experiment MN1000 represents the experiment with carbon ion beam of 270.55 MeV/u energy. Only one FNTD sample was used for this experiment, with the FNTD positioned just behind the Bragg peak in the rising flank (at 14.1 cm), as shown by the vertical dashed red line in the depth-dose profile in Figure 6.1 (absorbed dose = 0.83 Gy). The LET spectra from the FNTD measurements and from Monte Carlo simulations for this experiment, which was used to obtain the dosimetric and "Cell Dose" quantities, are shown in Appendix B (Figure B.1). Table 6.10 summarizes the macroscopic quantities measured by FNTD and compares them to the expected quantities from the Monte Carlo (MC) simulated values. As can be seen from this table, the FNTD measured dose (both the total and from primaries) compares relatively well with the simulation values, being a few percentages higher. The total fluence is about 1/3 less, while the fluence from primaries agrees. This discrepancy is due to the detection efficiency of the fragments, which is discussed in the next chapter [Section 7.2: Comparison of macroscopic values]. This discrepancy also appears in the LET_f values, as the LET_f values for all particles is around 20% higher for FNTD measured values, but matches the simulations when only the primary ions are considered.

Table 6.10: Comparison of MC simulated values with FNTD measured values for experiment MN1000

Value	MC prediction	FNTD measurement
Absorbed dose (Gy)	0.83	0.86
Dose from primaries (Gy)	0.75	0.80
Total fluence (cm^{-2})	$1.27 \cdot 10^7$	$1.0 \cdot 10^7$
Fluence from primaries (cm^{-2})	$2.8 \cdot 10^6$	$2.8 \cdot 10^6$
LET_f(keV/μm)	40.1	49.2
LET_f primaries (keV/μm)	89.0	90.0
LET_d(keV/μm)	103.1	110.3

Table 6.11 compares the results of the simulation from the "Cell Dose" model to the "Cell Dose" quantities along with their variations and the sources of variation as measured with the FNTD/Cell system. As can be seen from this table, the values are fairly consistent with the simulation values, although a higher variation is seen in $\tilde{D}_{nuc}$ and

$\tilde{L}_{nuc}$, which can be attributed to the sample size of ony 137 cells. The variation in area, number of hits and LET compare very well between the two. The chord length was not measured in the experiments as only the 2D area of the cell was used for this experiment. It should be noted that measured $\tilde{D}_{nuc}$ and $\tilde{L}_{nuc}$ are subject to measurements uncertainty, which needs to be quantified. This uncertainty with current settings is measured to be around 25% and will be discussed in the next chapter [Section 7.2: Comparison of "Cell Dose" quantities].

Table 6.11: Comparison of simulation vs measurement for MN1000 for variation in "cell dose quantities" and sources of variation

Value	Simulation	FNTD/Cell measurement
$\tilde{D}_{nuc}$ (Gy)	0.83	0.86
$\hat{\sigma}(\tilde{N}_{nuc})$ (%)	38.2	52.1
$\tilde{L}_{nuc}$(keV/μm)	39.0	48.4
$\hat{\sigma}(\tilde{L}_{nuc})$ (%)	30.5	41.2
$\bar{n}_{\text{hits}}$	23.4	18.2
$\hat{\sigma}(n_{\text{hits}})$ (%)	55.1	54.2
$\overline{\text{LET}}$(keV/μm)	40.1	65.1
$\hat{\sigma}$(LET) (%)	125.6	130.8
$\bar{x}(\mu m)$	11.1	-
$\hat{\sigma}(x)$ (%)	44.4	-
$\bar{A}(\mu m^2)$	183.5	183.4
$\hat{\sigma}(A)$ (%)	50.9	51.2

Figure 6.14 shows the distribution of $\tilde{D}_{nuc}$ and $\tilde{L}_{nuc}$ obtained from the computational model and as measured with cell/FTND experiment. This figure also shows the map of $\tilde{D}_{nuc}$ and $\tilde{L}_{nuc}$, which allows to visualize the result and correlate biological endpoints directly with the map.

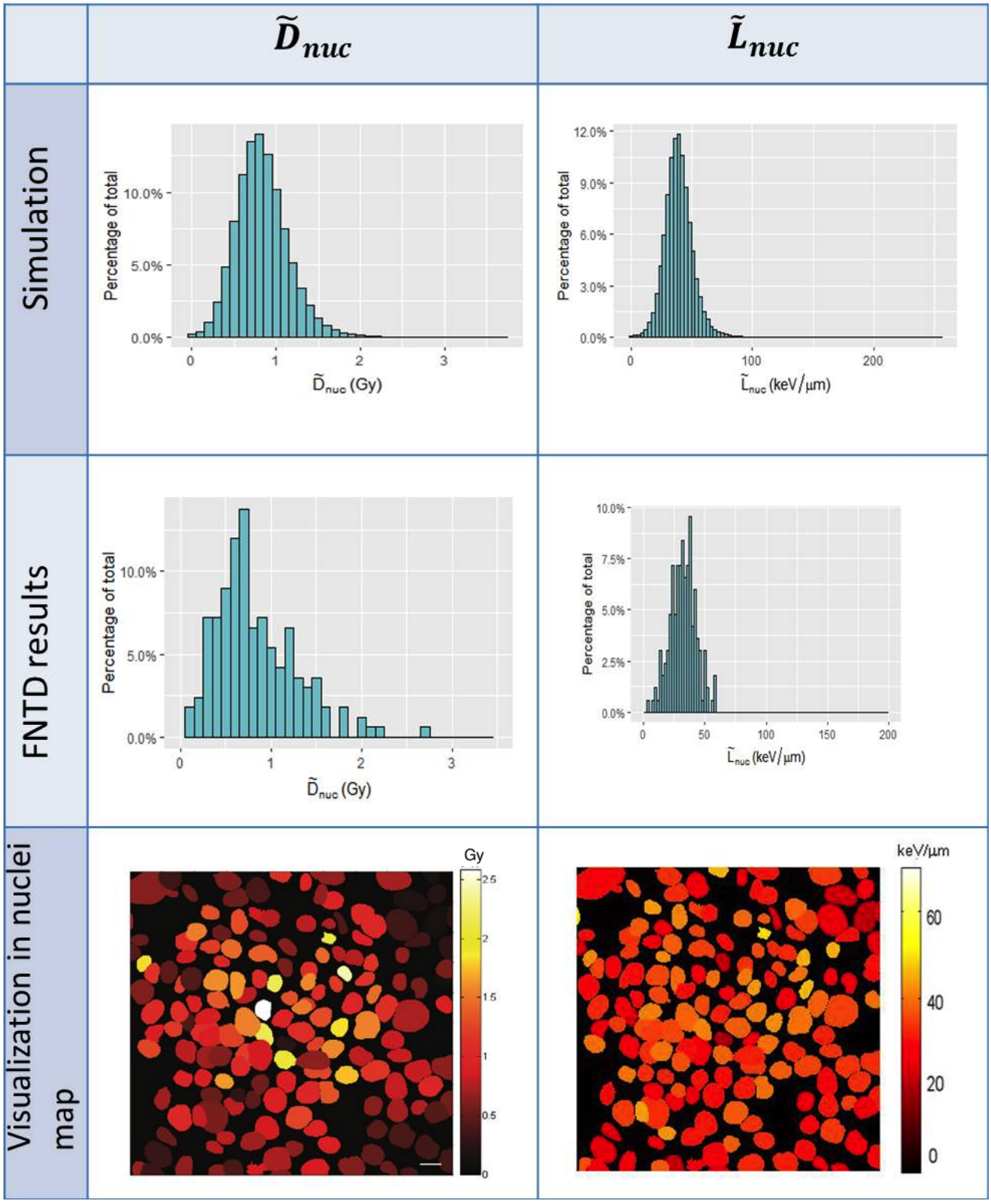

Figure 6.14: Histogram of $\tilde{D}_{nuc}$ and $\tilde{L}_{nuc}$ for MN1000 experiment as compared with simulations

For example the $\tilde{D}_{nuc}$ and $\tilde{L}_{nuc}$ can be compared to measured apoptosis as shown in figure 6.15

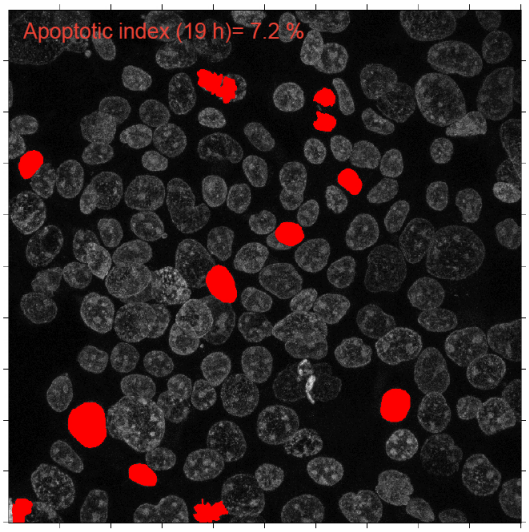

Figure 6.15: Example of map of apoptosis in MN1000 experiment (reprinted from [53]). Red cells show cell deaths due to apoptosis.

6.2.2 Physically Optimized Spread Out Bragg Peak

MN81000 Experiments The SOBP plan for the MN81000 is shown in Figure 6.6, with the samples positioned in the mid-SOBP at 3.9 cm (shown by red vertical dashed lines). Four different FNTDs were used for MN81000 experiment. The LET spectra from the FNTD measurements and from Monte Carlo simulations for this experiment, which were used to obtain the dosimetric and "Cell Dose" quantities, are shown in Appendix B.2. Table 6.12 shows the comparison of the macroscopic values from MC predictions with the combined result from FNTD measurements of the 4 samples. As can be seen from this table, the total dose is only about 3% less in the FNTD measurements. Likewise, the fluence and dose from primaries match well with MC predictions. However, the total flueunce is about 70% less, which comes from missing the secondary tracks as seen with the previous experiment. $\mathrm{LET_f}$ is about 20 keV/μm higher in the FNTD measurements than the simulated data, which again arises from missing secondary tracks. However, $\mathrm{LET_f}$ from primaries matches closely with the MC predictions.

Table 6.12: Comparison of MC simulated values with FNTD measured values for experiment MN81000

Value	MC prediction	FNTD measurement
Absorbed dose (Gy)	1	0.97
Dose from primaries (Gy)	0.94	0.95
Total fluence (cm^{-2})	$1.5{\cdot}10^7$	$9.2{\cdot}10^6$
Primary fluence (cm^{-2})	$8.7{\cdot}10^6$	$8.7{\cdot}10^6$
LET_f(keV/μm)	38.6	65.8
LET_f primaries (keV/μm)	67.2	67.9
LET_d(keV/μm)	98.7	128.0

Table 6.13 compares the results of the simulation from the "Cell Dose" model to the "Cell Dose" quantities along with their variations and the sources of variation as measured with the FNTD/Cell system. As can be seen from this table a higher variation is seen in $\tilde{D}_{nuc}$ and $\tilde{L}_{nuc}$, which will be explained in the discussion [Section 7.2]. The variation in area and number of hits compare very well with the simulations. The chord length was not measured in the experiments as only the 2D area of the cell was used for this experiment.

Table 6.13: Comparison of simulation vs measurement for MN81000 for variation in "cell dose quantities" and sources of variation

Value	Simulation	FNTD/Cell measurement
$\tilde{D}_{nuc}$ (Gy)	0.94	0.94
$\hat{\sigma}(\tilde{N}_{nuc})$ (%)	30.6	46.7
$\tilde{L}_{nuc}$(keV/μm)	37.5	62.5
$\hat{\sigma}(\tilde{L}_{nuc})$ (%)	21.8	32.3
$\bar{n}_{\text{hits}}$	28.8	19.8
$\hat{\sigma}(n_{\text{hits}})$ (%)	54.8	51.2
$\overline{\text{LET}}$(keV/μm)	38.5	63.2
$\hat{\sigma}$(LET) (%)	102.4	110.7
$\bar{x}(\mu m)$	11.1	-
$\hat{\sigma}(x)$ (%)	44.5	-
$\bar{A}(\mu m^2)$	183.7	190.2
$\hat{\sigma}(A)$ (%)	51.4	55.2

Figure 6.16 shows the distribution of $\tilde{D}_{nuc}$ in one of the samples, and Figure 6.17 shows the distribution of $\tilde{D}_{nuc}$ obtained from all of the four FNTD sample with the simulations results. As can be seen from this figure, the $\tilde{D}_{nuc}$ distributions have similar shapes, with the experimental data being a bit wider due to higher variation. The map of $\tilde{D}_{nuc}$ and $\tilde{L}_{nuc}$ for the individual samples are shown in the appendix (Figure C.1).

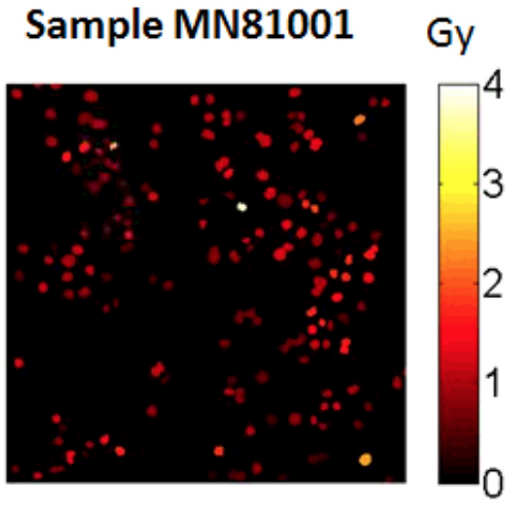

Figure 6.16: Map of $\tilde{D}_{nuc}$ for MN8100 experiment

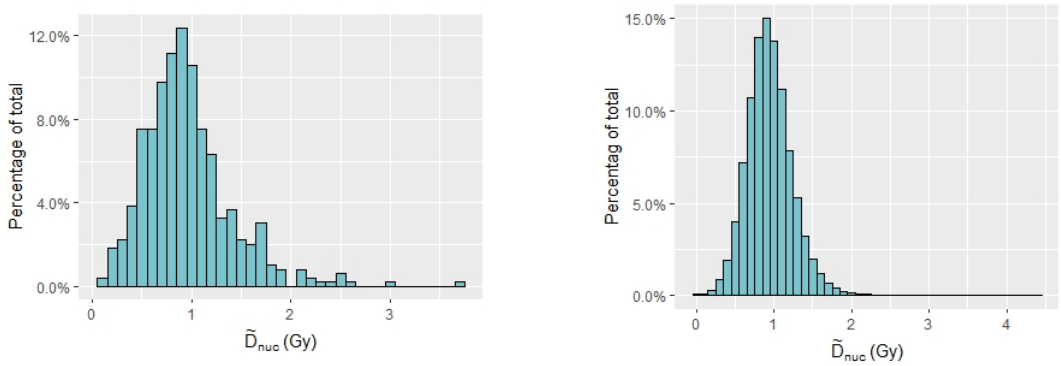

(a) FNTD

(b) Simultion

Figure 6.17: Histogram of $\tilde{D}_{nuc}$ for MN8100 experiment compared with simulation

MN12000 Experiments This experiment has the same irradiation set up as the MN81000 experiment, but the SOBP is optimized to 0.5 Gy absorbed dose. 5 differ-

ent FNTD samples were irradiated. Table 6.14 shows the MC simulation vs FNTD measurements of the the macroscopic parameters for all of the 5 samples (individual samples and the option setting and spectra matching can be found in the appendix). Again, as with the MN81000 experiment total dose, dose from the primaries, LET_f from the primaries and the fluence from the primaries agree well with the MC simulations, while the total fluence is about 70% lower in the measurements, and total LET_f is also higher. However, for this lower fluence sample, LET_f is closer to the simulations results than MN81000 sample (when the fluence/dose is two times higher).
Table 6.15 compares the results of the simulation from the "Cell Dose" model to the "Cell Dose" quantities along with their variations and the sources of variation as measured with the FNTD/Cell system. Similar to the the MN81000 experiment, a higher variation is seen in $\tilde{D}_{nuc}$ and $\tilde{L}_{nuc}$, and similar values are found for other sources of variation.

Table 6.14: Comparison of MC simulated values with FNTD measured values for experiment MN12000

Value	MC prediction	FNTD measurement
Absorbed dose (Gy)	0.5	0.5
Dose from primaries (Gy)	0.47	0.47
Total fluence (cm^2)	$7.5{\cdot}10^6$	$5.24{\cdot}10^6$
Primary fluence (cm^2)	$4.4{\cdot}10^6$	$4.4{\cdot}10^6$
LET_f(keV/μm)	40.7	59.5
LET_f primaries (keV/μm)	67.2	68.1
LET_d(keV/μm)	98.7	110.3

Table 6.15: Comparison of simulation vs measurement for MN12000 for variation in "Cell Dose" quantities and sources of variation

Value	Simulation	FNTD/Cell measurement
$\tilde{D}_{nuc}$ (Gy)	0.47	0.47
$\hat{\sigma}(\tilde{N}_{nuc})$ (%)	43.1	63.5
$\tilde{L}_{nuc}$(keV/μm)	37.4	51.8
$\hat{\sigma}(\tilde{L}_{nuc})$ (%)	31.7	49.0
$\bar{n}_{\text{hits}}$	14.4	10.1
$\hat{\sigma}(n_{\text{hits}})$ (%)	57.1	55.4
$\overline{\text{LET}}$(keV/μm)	38.5	52.4
$\hat{\sigma}$(LET) (%)	102.8	110.3
$\bar{x}(\mu m)$	11.1	-
$\hat{\sigma}(x)$ (%)	44.3	-
$\bar{A}(\mu m^2)$	183.8	188.1
$\hat{\sigma}(A)$ (%)	50.7	53.5

The combined results from experiments MN81000 and MN12000 correlating specific dose to the number of 53BP radiation induced foci (RIFs) is shown in Figure 6.18.

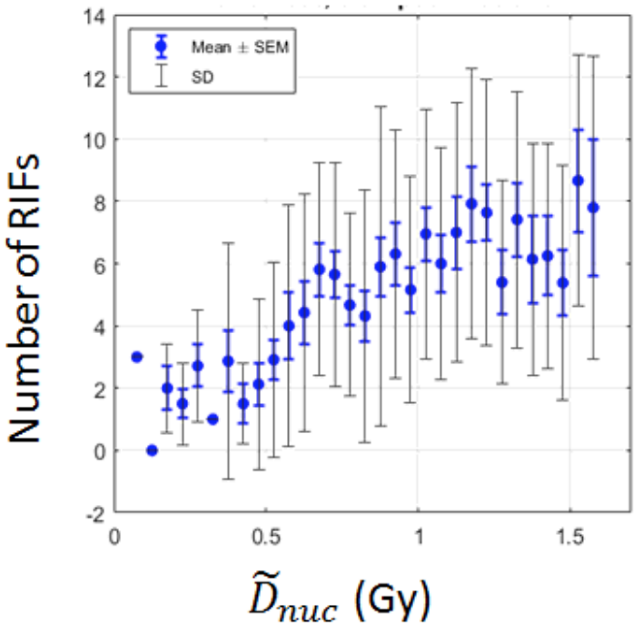

Figure 6.18: Correlation of specific dose with number of RIF for experiments MN81000 and MN12000. (Image courtesy of Martin Niklas)

SINF Experiments SINF experiments were conducted with the beamline microscope explained in Section 3.1.3.2. The cell covered FNTDs were positioned either at the entrance (0.7 cm) or at the distal end of the SOBP (7.2 cm). The measurement positions are shown in the depth-dose profile as depicted by red vertical dashed lines in Figure 6.9. Three FNTDs coated with cells were analyzed for each position. A total of 18 and 14 cells were analyzed for the entrance and SOBP positions, respectively. The LET spectra from the FNTD measurements and from Monte Carlo simulations for these experiments, which were used to obtain the dosimetric and "Cell Dose" quantities, are shown in appendix B.3. Table 6.16 shows the MC simulation vs. FNTD measurements of the macroscopic parameters for the entrance and SOBP samples (results combined for each depth). As seen from this table, the measurements vs. MC predicted values follow the same pattern as the previous experiments for the SOBP position, while a closer match is observed for the values in the entrance channel as there are less fragments.

Table 6.16: Comparison of MC simulated values with FNTD measured values for SINF experiment

	Entrance (0.7 cm)		SOBP (7.2 cm)	
Value	MC	FNTD	MC	FNTD
Absorbed dose (Gy)	0.70	0.69	1.0	0.98
Dose from primaries (Gy)	0.68	0.67	0.87	0.86
Total fluence (cm^2)	$2.43 \cdot 10^7$	$2.39 \cdot 10^7$	$2.52 \cdot 10^7$	$2.01 \cdot 10^7$
Primary fluence (cm^2)	$2.30 \cdot 10^7$	$2.30 \cdot 10^7$	$1.01 \cdot 10^7$	$1.00 \cdot 10^7$
LET_f(keV/μm)	18.0	17.8	24.2	47.1
LET_f primaries (keV/μm)	18.9	19.0	51.9	52.2

Table 6.17 compares the results of the simulation from the "Cell Dose" model to the "Cell Dose" quantities along with their variations and the sources of variation as measured with the FNTD/Cell system. Similar to the previous experiments, a higher variation is seen in $\tilde{D}_{nuc}$ and $\tilde{L}_{nuc}$, and similar values are found for other sources of variation. In this experiment, the chord length and its variation were also measured, and a higher variation is observed in the experimental data.

Table 6.17: Comparison of simulation vs measurement for SINF experiment in "Cell Dose" quantities and sources of variation

	Entrance (0.7 cm)		SOBP (7.2 cm)	
Value	Simulation	FNTD/Cell measurement	Simulation	FNTD/Cell measurement
$\tilde{D}_{nuc}$ (Gy)	0.69	0.68	0.96	0.97
$\hat{\sigma}(\tilde{N}_{nuc})$ (%)	19.3	42.1	28.2	63.1
$\tilde{L}_{nuc}$(keV/μm)	17.7	17.5	23.7	46.5
$\hat{\sigma}(\tilde{L}_{nuc})$ (%)	7.7	20.4	22.5	44.2
$\bar{n}_{\text{hits}}$	21.5	21.1	46.3	38.2
$\hat{\sigma}(n_{\text{hits}})$ (%)	55.1	56.5	52.7	58.2
$\hat{\sigma}$(LET) (%)	155.4	160.3	129.1	140.2
$\bar{x}(\mu m)$	11.1	10.8	11.1	10.5
$\hat{\sigma}(x)$ (%)	44.3	55.8	44.3	56.2
$\bar{A}(\mu m^2)$	183.7	170.4	183.7	174.9
$\hat{\sigma}(A)$ (%)	50.8	62.4	50.6	60.4

For this experiment the number of 53BP1 foci was measured at different time points after irradiation. Furthermore, the foci intensity of 53BP1 were also measured over time, with higher intensity indicating higher severity of DNA damage [51]. It was shown that higher Z particles with higher LET produce the most intense foci over time (Figure 6.19).

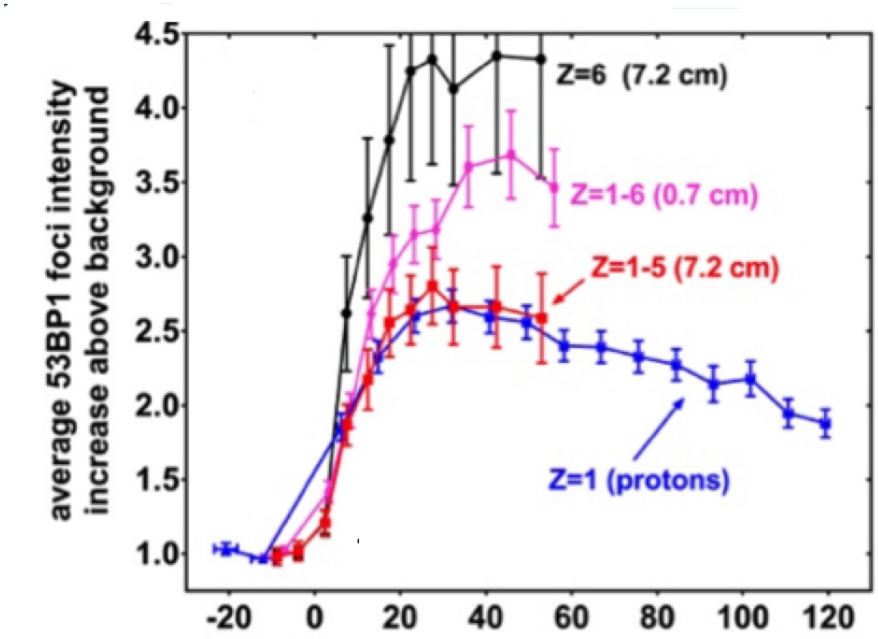

Figure 6.19: Average intensity increase of 53BP1 foci relative to nuclear background for all subgroups (primary and fragments at depths 0.7 cm and 7.2 cm) for the SINF experiment. Reprinted from [51]

Therefore, it was hypothesized in this thesis that the foci intensity would increase with specific LET. Figure 6.20 shows the plot of average foci intensity of 53BP1 foci at 45 minutes (where maximum intensity is observed). As can be seen in this figure, the average 53BP1 foci intensity increases with $\tilde{L}_{nuc}$. As there are only 32 cell nuclei, it couldn't be concluded if the increase is linear or exponential, as there seemed to be a saturation at higher $\tilde{L}_{nuc}$, but only a few cells had a such high $\tilde{L}_{nuc}$ values.

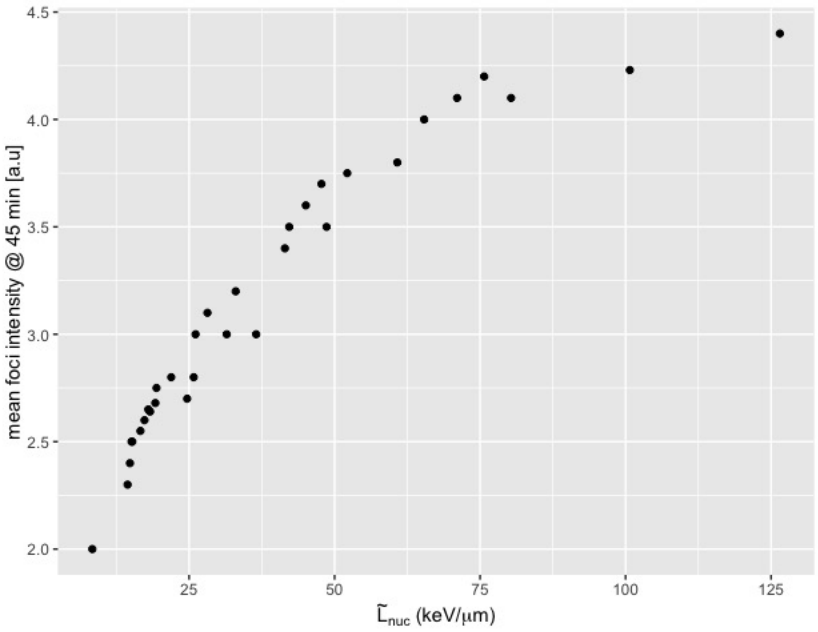

Figure 6.20: Specific dose vs average foci intensity of 53BP1 foci at 45 minutes for the SINF experiment.

6.2.3 Biologically Optimized Spread out Bragg Peak

As mentioned previously, the biologically optimized spread out Bragg peak condition was the case that was published [74] in the course of this thesis. For this study, the FNTDs were irradiated without cells, and no biological endpoint was measured. Instead, a virtual cell layer, using the cell image from MN1000 was used to overlay the tracks into the cell layer. The 137 virtual cells were overlaid on the track data obtained from the FNTD measurements and $\tilde{D}_{nuc}$ and $\tilde{L}_{nuc}$ were calculated for the virtual cells. To obtain a larger sample size, track positions were assumed to be uniformly distributed with complete spatial randomness and shifted for resampling in x direction (5 steps at 20 μm) and y direction (5 steps at 20 μm), rotated around the center (4 orientations at 90°), and mirrored (2 cases). This yielded a total of 200 configurations, resulting in a sample size of 27400 cells.

Table 6.18 summarizes the FNTD measured macroscopic dose and fluence for each depth and compares them to the expected absorbed dose from the treatment plan and MC simulated fluence values. The LET spectra from FNTD measurements and from Monte Carlo simulations used for these dosemetric measurements can be found in the appendix for all 7 depths (Figure B.6). As observed from Table 6.18, the FNTD measured dose

for all depths (except for 14.75 cm) compares fairly well with simulation results while fluence differs by a factor of 1.5-2. This is due to the observation that primary ions (which contribute the most to the overall dose) are well identified with FNTD, while fragments are vastly underestimated [80]. The vast difference for depth 14.75 can be explained by the positioning of the FNTD. As can be seen in Figure 6.11 the FNTD at depth 14.75 cm is at the very distal position of the SOBP where the dose falloff occurs, and thus an error of a few micrometer in the position of the FNTD (which is within the error expectation of this experiment) can result in the FNTD being positioned right after the SOBP.

Table 6.18: Comparison of MC simulated values with FNTD measured values from the biological SOBP experiment (SR308)

Depth (cm)	D_{bio} (Gy.RBE)	$D_{phys,MC}$ (Gy)	$D_{phys,FNTD}$ (Gy)	$\Phi_{tot,MC}$ (cm^{-2})	$\Phi_{tot,FNTD}$ (cm^{-2})
0.75	1.19	0.34	0.26	$1.73 \cdot 10^7$	$1.29 \cdot 10^7$
1.75	1.20	0.35	0.24	$2.02 \cdot 10^7$	$1.45 \cdot 10^7$
8.75	1.61	0.44	0.38	$3.17 \cdot 10^7$	$1.45 \cdot 10^7$
10.75	2.00	0.51	0.42	$3.16 \cdot 10^7$	$1.43 \cdot 10^7$
12.75	2.00	0.48	0.43	$2.22 \cdot 10^7$	$1.13 \cdot 10^7$
14.75	2.00	0.40	0.06	$2.32 \cdot 10^7$	$6.71 \cdot 10^6$
17.75	0.32	0.06	0.02	$1.64 \cdot 10^7$	$5.24 \cdot 10^6$

Figures 6.21 and 6.22 illustrate the mean cellular energy deposition and the overall variation in the virtual cell layer obtained from the experimental FNTD measurements at different SOBP positions in terms of specific dose and specific linear energy, respectively, and compares them to simulated results. Figure 6.23 shows an illustration of this result for better visualization of in terms of cellular energy distribution at 3 different depths and illustrates the FNTD measured values in the virtual cell layer for a single configuration. The complete set of such figures for both and distribution for all depth are provided in the appendix (Figure C.3). As can be seen from Figure 6.21, the expected value of specific dose is lower in the experimental values (about 20-40%) than the simulated values. This is not surprising since the macroscopic absorbed dose is lower in the measurements. The shape of the distributions, however, is similar to the expected values although shifted toward the lower values, as expected. Values from the experimental values are much larger, ranging from 40% in the entrance channel to 70% in the SOBP. Such high variation can be explained by the limited amount of data

and the line-width of the measured LET spectrum (explained in Chapter 7 [Section 7.2: Comparison of macroscopic values]).

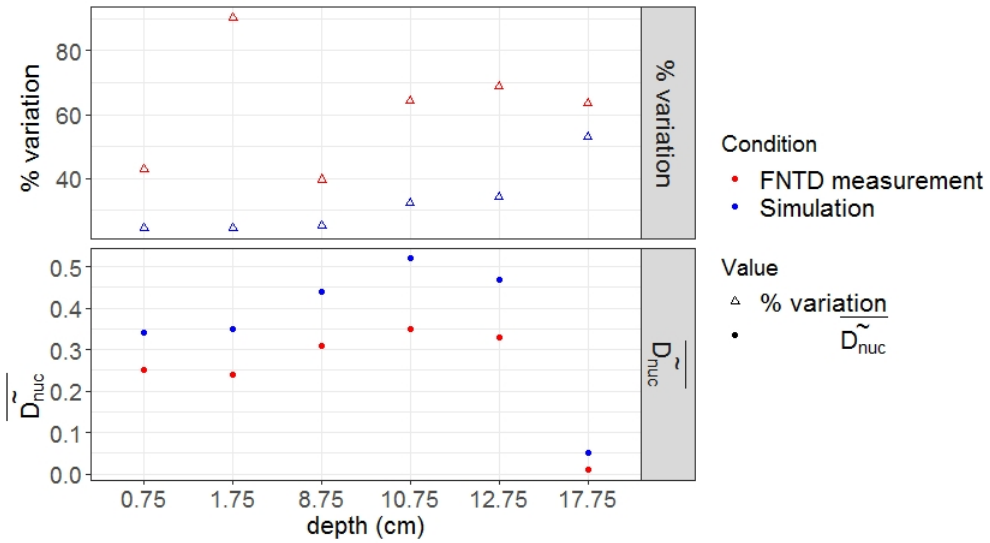

Figure 6.21: Comparison of expected value of specific dose and its variation between FNTD measurements and simulation for SR308 experiment

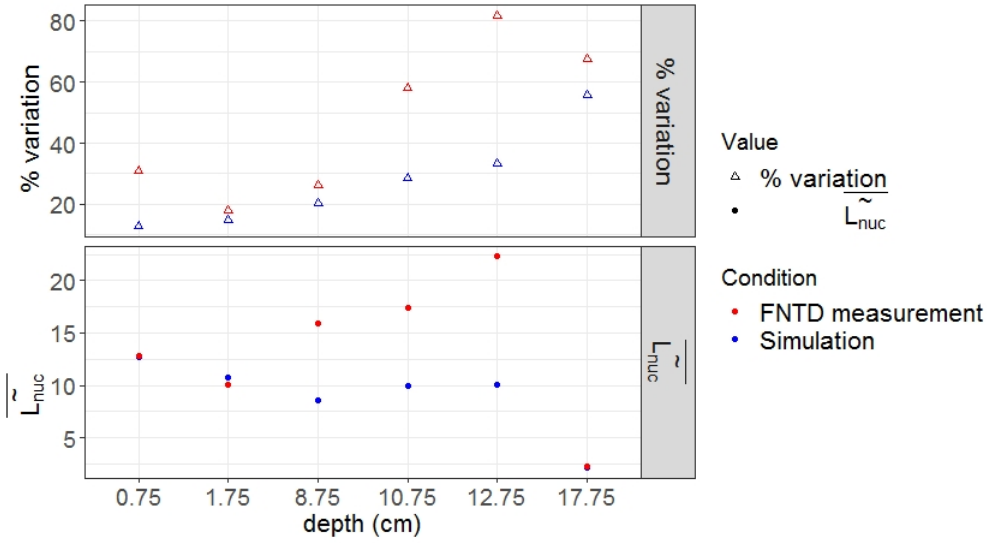

Figure 6.22: Comparison of expected value of specific LET and its variation between FNTD measurements and simulation for SR308 experiment

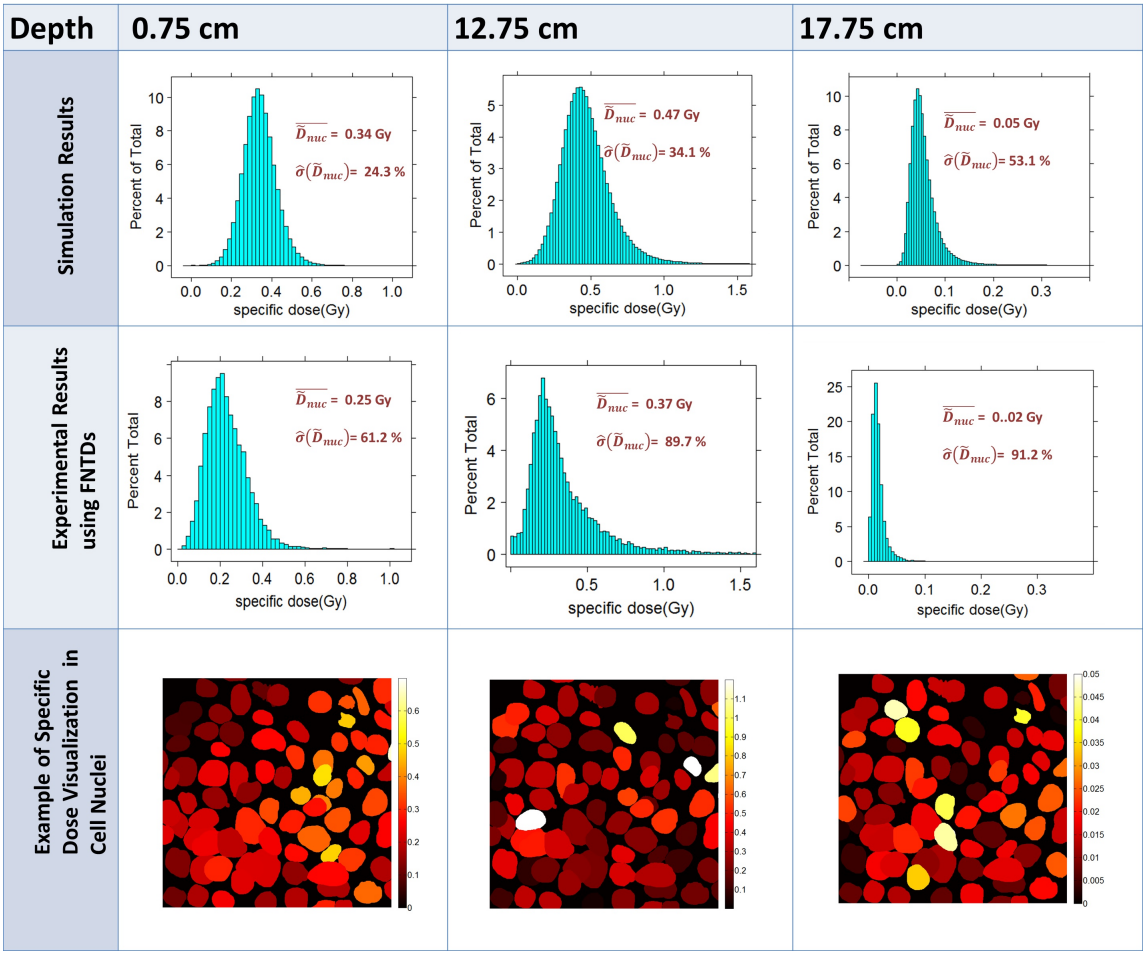

Figure 6.23: Comparison of measured vs. simulated specific dose of experiment SR308 for different depths

Chapter 7

Discussion

In this chapter the results of the application of the new "Cell Dose" framework are discussed. The simulation results from the computational model (as shown in Figure 5.5) is explored and subsequently compared to experimental measurements with FNTDs. The correlation between the introduced microscopic quantities specific dose and specific LET with biological endpoints is examined, including a discussion on the limitations and uncertainties existing in the "Cell dose" framework and potential future experiments.

7.1 Simulation with the "Cell Dose" Model

The simulation results obtained by using the proposed "Cell Dose" model, presented in the previous chapter, show the feasibility of this model and gives insight into how these values are distributed in a cell-wide population.

Monoenergetic beams

First, three monoenergetic carbon ion beams representing the range of therapeutic carbon ion beams at HIT were simulated at different depths. The mean values of $\tilde{D}_{nuc}$ and $\tilde{L}_{nuc}$, as expected, almost equate with their respective macroscopic quantities, dose and $\mathrm{LET_f}$, within the standard error. However, a slight underestimation is observed that may be due to some systematic uncertainty in the program when calculating one of the parameters, such as underestimation of energy loss straggling when sampling from one of the distributions [Section 2.7].
The results indicated, that relative to the Bragg peak (of same physical dose), from

the entrance channel to the Bragg peak, different carbon ion energies show a similar variation in specific dose and specific LET. In the tail region, however, the high energetic carbon ion beam had a reduced variation compared to the lower energies. This difference may be due to the fact that the fragments from the higher energetic ions spread their deposited energy in a wider range.
For a Bragg peak of 1 Gy, for all three energies, already in the entrance channel a significant variation of ∼30% is seen in the specific dose. This variation increases considerably towards the Bragg peak reaching around 45 % in the Bragg peak and up to 110 % in the tail region for the lower energies. The variation in specific LET is much lower in the entrance channel (half of what is observed with the specific dose), but reaches comparable values in the Bragg peak region and the tail. Such pattern of increase with depth with both $\hat{\sigma}(\tilde{D}_{nuc})$ and $\hat{\sigma}(\tilde{L}_{nuc})$ is understandable as more fragmentation occurs at larger depths, and therefore more variation is observed, since a mixture of ions of various energies is present. The large variations in $\tilde{D}_{nuc}$ and $\tilde{L}_{nuc}$ indicate that it is important to quantify energy depositions for single cells, and that even in the entrance channel with lower LETs and less ion diversity, the cells are exposed to a wide range of deposited energy. This becomes even more prominent in the Bragg peak region where more fragments are present.

To see the relationship between absorbed dose and $\hat{\sigma}(\tilde{D}_{nuc})$ and $\hat{\sigma}(\tilde{L}_{nuc})$, the Bragg peak position was simulated from 0.5 Gy to 10 Gy in steps of 0.5 Gy. The results (Figure 6.5) indicated that there is an exponential decrease in both $\hat{\sigma}(\tilde{D}_{nuc})$ and $\hat{\sigma}(\tilde{L}_{nuc})$ with absorbed dose. Thus, it shows that the dose delivered is important when considering the variation of biological effect within the cell population. When the absorbed dose is relatively low (<2 Gy), it is applicable to use cellular dosimetry as the variation in cellular energy deposition is higher. However, with higher doses, the variation is relatively low (around 20 % for $\hat{\sigma}(\tilde{D}_{nuc})$ for 5 Gy as compared to 65 % for 0.5 Gy). Therefore, most cell nuclei will see the same local energy deposition in terms of $\tilde{D}_{nuc}$ and $\tilde{L}_{nuc}$. Such high variation at lower doses can be important when considering biological effects in ion beam therapy, especially with dose fractionation where lower doses are delivered in each fraction.

SOBPs

While IBRT is mostly performed with SOBPs, many radiobiological experiments, such as the MN1000 experiment studied in this thesis, are performed with monoenergetic

ion beams for simplicity and investigating single energies. However, when conducting the measurements close to or at the Bragg peak, it should be considered that the absorbed dose increases drastically towards the Bragg peak. Therefore, in this study several positions within 1 mm of each other in the Bragg peak and rising flank regions were simulated. The results showed that there was a small amount of increase in the variation (3-5 percentage points) of $\tilde{D}_{nuc}$ and $\tilde{L}_{nuc}$ when moving towards the Bragg peak. However, just 1 mm after the Bragg peak, about 10 percentage points increase was observed compared to Bragg peak position. More significantly, $\overline{\tilde{D}_{nuc}}$, which follows the absorbed dose, had a significant difference of 20 % just 1 mm before and after the the MN1000 experimental position. Therefore, while pristine Bragg peaks might be more straightforward to use for radiobiological experiments, for cellular dosimetry it is preferable to use a SOBP as it has the same dose over a wider region and also better represents therapeutic settings. It was observed with SOBP plans that while they show similar $\hat{\sigma}(\tilde{D}_{nuc})$ and $\hat{\sigma}(\tilde{L}_{nuc})$ relative to the depth as monoenergetic beams, there was an increase in total variation from the distal to proximal end of the SOBP, which was also the case for a biologically optimized SOBP. Such increase is an additional factor to consider for treatment planning when considering biological effects.

Comparison of different sources of variations

In addition to assessing the total variation of "Cell Dose" quantities in a cell population, another goal of performing the simulations was to see how each sources of variation contributes to overall variation in energy deposition inside the cell nuclei and how using a cell-hybrid detector (i.e with FNTDs) setup can help to reduce uncertainty in the measurement of specific dose and specific LET (for the different cases explained in table 5.1).

The first source of variation considered was the variation in the cross-sectional area of the cell nuclei. Holding the area constant showed a reduction of 2-3 percentage points in the entrance and SOBP, and 6-13 percentage points at higher depths in the tail region where the variation is much higher. This is about 8-12 percent reduction in total variation for both specific dose and specific LET. Therefore, only using 2D microscopy to image the cells without any detector to correlate the tracks can reduce the uncertainty by a relatively small but significant amount. It should be noted that the nucleus was considered a sphere. However, if the true shape of a nucleus was implemented, it may affect the numbers reported. However, that would be computationally very expensive, and as the contribution of area variation is already small, so implementing the entire

geometry of the nuclei is not of great benefit.

The next source of variation considered was the number of particles crossing the nuclei (nuclear hits). Using fluence information with FNTDs can reduce this uncertainty in the measurements. The simulations indicated that this source is the main contributor of specific dose variation in the entrance, cutting the uncertainty by about 50 %. However the contribution of nuclear hits reduces by depth and in the SOBP region only reduces the uncertainty by 4-5 percentage points (around 15-17 %). Since nuclear hits are dominated by primary particles with similar LET in the entrance region, they play the most significant role in the overall variation in specific dose. Therefore, reducing the uncertainty due to nuclear hits causes a significant decrease in overall uncertainty in the entrance region. At further depths, as more fragmentation occurs and fluence becomes higher, the LET variation becomes more prominent and knowledge of the number of hits becomes less significant. As for specific LET, the number of hits does not contribute a significant amount, and is almost negligible with contributions less than 1 percentage points through all depths. This could be because in the definition of specific LET, the energy imparted is divided by all the chord lengths of the particles, thus cancelling out the effect of individual hits. These results indicate that by using FNTDs (or other detectors) to find the number of hits to nucleus is important for the entrance channel, and can slightly improve uncertainty at higher depths.

The next source of variation considered was the chord length of the particles crossing the cell nuclei. The results indicated that the chord length had the least impact on both $\hat{\sigma}(\tilde{D}_{nuc})$ and $\hat{\sigma}(\tilde{L}_{nuc})$. Only around 2 percentage points decrease were found for $\tilde{D}_{nuc}$ at most depths, and less than 1 percentage points for $\tilde{L}_{nuc}$. Thus, while chord length is important in calculating specific dose and specific LET, it doesn't contribute much to their variation. This is of particular importance for experimental measurements because recording the volume of each cell nuclei and extrapolating the tracks onto the cell volume to measure the chord length takes a lot more efforts for image processing and is computationally very time and data consuming. However, since the variation in chord lengths doesn't contribute much to the overall energy deposition variation, the mean chord length based on cell area, assuming a sphere, can be used. As the contribution to the total variation is quite small, this approximation would fall within experimental uncertainties of measuring the chord length, and thus is reasonable.

The next source of variation was the LET variation of different ions inside the nuclei.

Identifying individual LETs showed the most significant reduction in total variation of specific dose and specific LET at most depths. While in the entrance channel only a 2-3 percentage points reduction of the variation of both $\tilde{D}_{nuc}$ and $\tilde{L}_{nuc}$ is realized, at the SOBP, it showed a significant reduction of around 10-20 percentage points (around 50-75 % reduction in total variation). This reduction was even more significant in tail regions, with a reduction of more than 60 percentage points, dominating the variation. It is understandable that in the entrance region, LET variation doesn't play a significant role, as not much fragmentation has occurred, and thus the beam has a more homogeneous LET distribution. The main issue for achieving a constant LET in the model was, that if an average LET of all particles is considered, as was done with other sources of variation, the entire particle spectrum wouldn't be represented. Since energy loss straggling is still calculated and requires the charge of the particle when sampling from one of the distributions, using an average LET requires to only use carbon as the representative ion with the average LET of the entire spectrum. This estimation only uses the energy loss straggling of carbon ions, which is much lower than of the fragments. Therefore, using this options will indicate a much higher reduction in total variation as compared to what actually would be realized by using FNTDs. To account for this issue, a spectrum of particles based on the number of nuclear hits was sampled, and the same spectrum was used to calculate the variation in each iteration, which in this case only arose from energy loss straggling. This of course slowed the computational time down, but was a better alternative than using a representative single particle. Even with this approach, the results showed the most significant reduction in both $\hat{\sigma}(\tilde{D}_{nuc})$ and $\hat{\sigma}(\tilde{L}_{nuc})$ is observed when information about the particle's LET is added (going from condition D to E in table 4.1). This condition can be realized by correctly evaluating LET of each particle track with the FNTDs. Achieving this condition results in an uncertainty of about 5 to 12% in cellular energy deposition, which represents the variation of energy loss straggling inside the cell nucleus. Measuring this energy loss is beyond the capabilities of current experimental equipment. While energy loss straggling of ions can be quantified with FNTDs [81,82], it cannot be predicted how the straggling will be inside the cells due to its stochastic nature. However, a reduction of down to 75 % is a significant increase in knowledge, which justifies the use of FNTD for cellular dosimetry.

Comparison of different ion types

In addition to simulating different carbon ion energies and SOBPs, different ion types were also simulated to compare the variation in specific LET and specific dose across different ion species. It was shown that the total variation is significantly less for protons at all depths, while for helium ions it s somewhere in between protons and carbons. This difference can be attributed to two different factors. First reason is due to fragmentation which is the primary cause of variation as observed earlier. The primary protons don't undergo any fragmentation, and from helium ions only protons arise as fragments, thus less variation is observed with these particles as compared to carbon ions. The second reason is that the fluence of protons and helium ions is much important than for carbon ions for the same absorbed dose, and the variation reduces with higher fluence of particles. This is more significant when using the same RBE weighted dose, since for protons and helium even a higher fluence is needed to achieve the same RBE weighted dose. This result suggests that using FNTDs to reduce energy deposition uncertainty (in terms of $\tilde{D}_{nuc}$ and $\tilde{L}_{nuc}$) in proton beams would not add any significant additional information due to the already low variation, while it can be slightly beneficial with use of helium ions. These simulation results illustrate that low LET irradiation shows less variation at the cellular level for the same dose. While photon simulations have not been performed (since this thesis focuses on ion beam radiations) similar low variability is expected, which has been shown with radiological experiments elsewhere [83–85]. For low dose experiments (i.e < 100 mGy), however, the variability in low LET irradiation can be important for both photons and particles. Radiobiological experiments performed with other techniques such as microbeam irradiation are thus important to understand the biological effects associated with low dose radiation at sub-cellular levels.

In conclusion, the simulations shed light on the overall variation of $\tilde{D}_{nuc}$ and $\tilde{L}_{nuc}$ and gave detailed information on individual sources of variation. It should be noted that holding single variable constants was not perfectly achievable with the current model since the sources of variations are dependent on each other. For example the area affects both the chord length distribution and number of hits, and number of hits affect the LET variation. Therefore, a further and more complicated approach is needed to isolate the individual sources and investigate the covariance between the sources. Furthermore, the Monte Carlo parameters and physics modeling choices used may also present sources of uncertainty in the simulation results.

7.2 Comparison with the Experimental Results

Comparison of macroscopic values

When comparing experimental and simulation results within the "Cell Dose" framework, it is first important to compare the macroscopic values obtained from FTND measurements to Monte Carlo simulations. For all of the experiments performed in the Bragg peak or SOBP area, the total fluence was about 70 % lower than what was predicted from the MC simulations. The fluence of primary ions only, however, matched fairly well between experiments and simulation. This indicates that FNTDs are efficient in detecting the primary ions but fail to capture the lower LET particles. In other studies with FNTDs [80] it was also shown that the efficiency of detecting lower LET fragments is significantly underestimated, contradicting the findings from other studies that indicated FNTDs are capable of reliably identifying particles with LET values down to 0.3 keV/μm (in water) [46, 86]. However, what was observed from the experiments performed in this thesis and the other works in our group at DKFZ [82], with a mixed beam field the detection of particles with low LET and large polar angles were much lower than expected. The reason for this deficiency may be due to the fact that secondary protons can exhibit both considerable kinetic energy and large polar angles with respect to the primary beam, which yields very low fluorescence signals in the FNTD and therefore degrades detection efficiency. The reason that presence of higher LET ions lowers the detection efficiency can be due to presence of more secondary electrons which have similar fluorescence signal to these low LET particles, thus interfering with the tracking process in the image analysis. Additionally, having bright signals from the high LET ions further changes the detection ability in image processing of low intensity signals from these large angle/high energy particles. Additionally, many of the fragments are missed in FNTD measurements in the track spot and track trajectory identification process [Section 3.2.2] in order to exclude false tracks from background signal and secondary electrons. A higher readout time with the microscope can reduce some of the noises and a more complicated track identification process, perhaps from such methods as machine learning, can improve the track identification process.
Although these fragments are not efficiently detected, they contribute very little to the energy deposited (less than approximately 5 % in the SOBP) as shown by the results of this study and other studies with FNTDs [80]. This explains the observation that with all the experiments shown, the absorbed dose measured by FNTDS matched fairly well the simulation results. The few percentage difference in the total dose was mainly

caused by missing the contribution of low LET particles as already discussed. In the SR308 experiment, only the FNTD positioned at 14.75 cm had a significant decrease in estimated dose compared to MC prediction. The vast difference for depth at 14.75 cm in the SR308 experiment compared to the other positions can be explained by the positioning of the FNTD in the depth dose profile. As can be seen in Figure 6.11, the FNTD at depth 14.75 cm is at the very distal position of the SOBP where the dose falloff occurs, and thus an error of a few micrometers in the position of the FNTD (which is within the error expectation of this experiment) resulted in the FNTD being positioned right after the SOBP where the dose fall off occurs. This can also be observed from Figure B.6 as there is not a prominent primary peak present in the FNTD spectra, indicating that the FNTD was not positioned in the SOBP as planned.

While the absorbed dose and other quantities such as $\mathrm{LET_f}$ and $\mathrm{LET_D}$ of the primaries matched well with the MC simulations, it should be noted that the Monte Carlo simulations were used to calibrate the LET spectrum of FNTDs by matching for the primary peaks and optimizing for dose, $\mathrm{LET_f}$ and $\mathrm{LET_D}$ of primaries [Chapter 5]. Therefore, the main reason that dose matches so well especially in later experiments is that the matching was improved for better optimization for these values. Numerous attempts have been made with other studies within the group [81, 82], to achieve a sample independent calibration for converting intensity signals from FNTDs to LET. However, due to large inter-detector variability in sensitivity, a consistent and reliable method, that is independent of matching the spectra with simulations has not yet been attained. Therefore, at its current state, FNTDs cannot be used as independent dosimeters, and should be calibrated individually with MC simulations of the irradiated position. Further, improvement in spectra matching is also needed to get more reliable results.

Comparison of "Cell Dose" quantities

After comparing the macroscopic values, the "Cell Dose" quantities from the computational model was compared with the experimental measurements. The mean values for $\tilde{D}_{nuc}$ matched pretty well for all experiments. Although for SR308 experiment, the $\overline{\tilde{D}_{nuc}}$ was slightly lower than the simulated values, due to the macroscopic dose also being lower in the measurements. This difference is due to the fact that in the course of this thesis, a lot of improvements have been made in the FNTD image analysis, calibration and spectra matching. Thus, analysis with newer versions resulted in better consistency with MC data. As for the $\hat{\sigma}(\tilde{L}_{nuc})$, while the shape of the distribution

is very similar for FNTD measurements and simulations results, the values are much higher in the experimental results ranging from 40% in the entrance channel to 70% in the SOBP. Such high variation can partially be explained by the line-width of the measured LET spectrum (as seen in appendix B). The FTND measured peak for the carbon primaries appears wider than in the MC spectrum which reflects the line-width of the FNTD system. In previous studies from the group [82], the relative linewidth was measured as 3.8-6.5 % corresponding relative broadening of 4 % (at 1 keV/μm) to 14 % (100 keV/μm). Another reason for the high variation in experimental measurements, was that the number of cells analyzed was much lower in the FNTD experiments than the simulations. Thus, more experimental data and more accurate LET measurements are required to result in a better statistical conclusion regarding $\hat{\sigma}(\tilde{D}_{nuc})$. As for $\tilde{L}_{nuc}$, the mean values are very similar in the entrance region for experimental and simulated values since most of the particles are primaries and FNTDs can detect them with great accuracy. However, in the SOBP region, $\tilde{L}_{nuc}$ is much higher in the experimental results than the simulation because of the current limitation of FNTDs in the detection of secondary protons, as discussed, resulting in greater primary to fragment ratio and subsequently higher $\tilde{L}_{nuc}$. The higher $\hat{\sigma}(\tilde{L}_{nuc})$ in FNTD measurements can be explained again by the broadening of the LET spectrum.

7.3 Correlation of "Cell Dose" Quantities to Biological Response

The ultimate goal of using a cell hybrid detector is to correlate energy deposition in the cell nuclei to a biological endpoint. Therefore, correlation of specific dose and specific LET to biological endpoints was briefly investigated in this thesis. Three biological endpoints were chosen including number of RIFs at different time intervals post irradiation, intensity of RIFs post irradiation, and presence of apoptotic marker indicated by caspase-3/7 activity. Due to the lack of a large data set to draw a statistically significant conclusion, the results of these correlations were presented only as showcasing the biological application of the "Cell Dose model", and further studies with a larger data set are required.

Apart form the SR308 experiment, all the experimental measurements with FNTDs were performed with cells containing one or more biological markers to identify radiation induced response. In the MN1000 experiment, from a previous study [53] it was

shown that only 4% of the ion tracks were causing a RIF sequence, therefore as the numbers were very low, the results were not presented in this study. However, in that same experiment the apoptosis of cells was assessed using capase-3/7 activity. Only 7 % of the cells were apoptotic (based on the caspase signal). Again the small number of apoptotic cells in this experiments prevents to draw reliable conclusions, but at first glance when looking at distribution maps of $\tilde{D}_{nuc}$ and $\tilde{L}_{nuc}$ and comparing it with the apoptotic map, it can be seen that the cells that were apoptotic received both higher $\tilde{D}_{nuc}$ and $\tilde{L}_{nuc}$. Again more experimental data are needed to draw a significant conclusion. However, in this feasibility step it was shown that that it is likely that the apoptosis potential of individual cells depends on "Cell Dose" quantities. A cell survival study with more cells and plotting individual cell survival as a function of $\tilde{D}_{nuc}$ and $\tilde{L}_{nuc}$ after an irradiation time point when apoptosis is expected, can give a better radiobiological insight.

In the MN800/MN12000 experiments, considerably a larger number of cells were studied (n=2100). It should be noted that the biological data from these experiments are still under analysis (manuscript under preparation [52]), which are being carried out by Niklas et al. as mentioned previously. Therefore, the data presented is only preliminary and still needs further validation. The preliminary results presented, showed that there is a linear positive correlation between the number of RIFs induced and $\tilde{D}_{nuc}$. However, as seen with the large error bar in the data (Figure 6.18), there was a substantial variability in RIF formation for individual cells that received $\tilde{D}_{nuc}$, which is reflected by a Pearson-Coefficient of only 0.37 for the linear fit. In this study (data not shown), it was observed that there was a slightly better correlation for RIF formation and number of nuclear hits (Pearson coefficient of .44). A possible explanation is that while the number of number DNA damage sites is dependent on the deposited energy in general, a single RIF might contain more than one DNA lesions, representing complexity of damage.Therefore, it is more important to characterize the complexity of damage. The complexity was not accessed in this experiment, however in the SINF experiment, which will be discussed next, it was evaluated. Furthermore, there are a lot of biological factors that cause single cell variability due to heterogeneity of tumor cells and the condition of the cell environment, which are beyond the scope of this thesis.

For SINF experiment, the average intensity of RIFs over time was evaluated as a surrogate for complexity of lesions. As the intensity was shown to be correlated to the LET of single tracks causing the damage, the $\tilde{L}_{nuc}$ was plotted as as a function of

average foci intensity in cell nucleus. The data showed that the foci intensity indeed increases with $\tilde{L}_{nuc}$. However, only a total of 32 cells were analyzed with this experiment, and therefore a statistical conclusion could not be reached. The beamline CSLM used in this experiment provides a great advantage of online monitoring immediately after irradiation, as the cells don't need to be moved, which provides a better image correction for cell movement (a big source of uncertainty with other methods). Furthermore, it allows to assess RIF formation pre and post irradiation at earlier time points than other methods. This again is of great advantage, because a better count of initial RIFs can be provided, while in other experiments some of the RIFs might have already been repaired during the handling process to move the cells for imaging after irradiation.This will help to better asses the repair kinetics of the RIFs as a function of $\tilde{D}_{nuc}$ and $\tilde{L}_{nuc}$. Furthermore, it helps to account for endogenous foci that were not formed by irradiation to provide a control. Despite all of these advantages, the main issue is the inability to image larger number of cells with the current procedures and cell identification techniques. Therefore, further improvements such as batch imaging and high throughput data processing is needed to use such a microscope for cell dosimetry applications.

Chapter 8

Conclusions and Outlook

In this work, in the first step, a theoretical framework was established to define dosimetric quantities relevant at microscopic scale in the size of the cell nucleus, which encompasses a sampling method that incorporated different sources of variations. These quantities, $\tilde{D}_{nuc}$ and $\tilde{L}_{nuc}$, are stochastic quantities that can be considered as "intermediate" quantities between the macroscopic quantities absorbed dose and LET, and microdosimetric quantities specific energy and lineal energy, respectively. Defining energy deposition in these terms of course does not encapsulate the mechanism of radiation action at the most basic levels. It is widely known that the main target of ionizing radiation is the DNA, and its effectiveness is based on the ability of the radiation to cause DNA lesions that can lead to cell death [1, 2]. Defining and investigating the physics behind creation of such DNA lesions requires description of the interaction of the ionizing radiation from the primary stage of ionization, track structure of the ions, radical creation, chemical interactions and beyond, which is addressed in approaches such as nanodosimtery and multiscale modeling [87, 88]. The model suggested here defines the energy deposition in the cell nucleus, where the DNA is located. While this specification does not go into nanoscale depths, it is a step in between the fundamental level and the macroscopic level. One of the advantages of such intermediate quantification is that the quantities can be measured in situ (for example by using FNTDs). This is an alternate approach that might be helpful in the clinical settings due its relative simplicity and the fact that it can be derived from the current data used in treatment planning systems.

The simulation results showed a great amount of variation (24-55%) in terms of energy distribution and radiation quality (ionization density) in cell nuclei for clinically relevant carbon ions in the SOBP. The greatest effect was due to the LET variation of individual particles. Nuclei area and chord length distributions, in contrast, played only a minor role, the poisson distribution of nuclear hits and energy loss straggling had a more inter-

mediate effect. This observation suggests that detectors capable of recording particles and their energy deposition in combination with MC generated particle spectra (which can also be obtained from treatment planning data without loss of generality) can be used to correctly identify nuclear hits and their LETs, and therefore reduce uncertainty in the cellular dose measurements potentially down to 4-14 %. One implementation of such detectors are FNTDs. However, there are some principle/current shortcomings with these detectors, including low detection efficiency for fragments and inconsistent LET measurements. Therefore, while cell experiments with FNTDs promise a great improvement in microscopic cellular energy measurements, further improvements are required to optimize fluence measurements and accurately measure LET of single tracks.

It was also shown that it is feasible to correlate biological endpoints to the introduced quantities $\tilde{D}_{nuc}$ and $\tilde{L}_{nuc}$. Based on the results, in principal a positive correlation was observed between these quantities and radiation damage. Future work is required to acquire more data for statistical analysis to further validate these findings. Future applications of this framework include studies to correlate RBE as function of $\tilde{D}_{nuc}$ and $\tilde{L}_{nuc}$ and their variation. Different radiation effects, such as the bystander effect [89] can also be studied within this framework, as it allows to see how cells that did not receive any energy deposition can respond to radiation.

Furthermore, the way the model is established, it allows to include more sources of variation and redefine the volume of energy deposition. This property can be utilized to compare the current model with current biological models such as LEM and MMKM. One example is to vary the volume of energy deposition to see at which scale the models converge to obtain the same RBE values. This would be of importance because at smaller volumes it is not feasible to directly correlate biological endpoints to energy deposition in individual cells, as in these volumes energy loss straggling plays a more significant role (which can be tested with the presented model). Moreover, additional sources of variations that can have an effect in the cellular energy deposition, such as radial dose distribution (considered in the LEM), oxygenation conditions, distribution of the sensitive targets and other parameters that were not considered here, can be added to the model to see their effects in future studies.

In conclusion, it was shown that the "Cell Dose" model can help to gain valuable insights in correlating physical properties of ion beams to biological response and allows for a way to describe energy deposition that is appropriate for single cells.

Appendices

Appendix A

Simulation of Carbon Ion Bragg Peaks with the "Cell Dose" Model

A.1 91.1 MeV/u Carbon ions

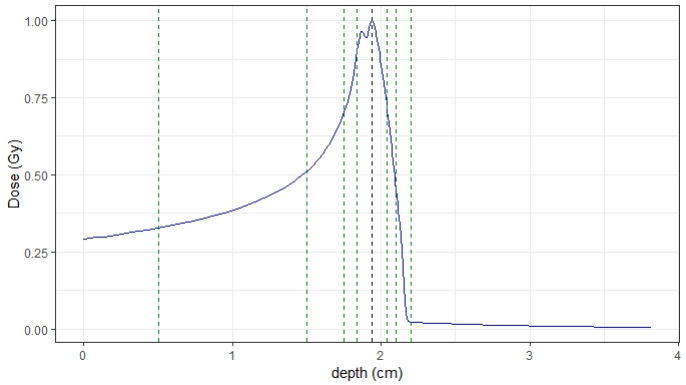

Figure A.1: Depth-dose profile for the 91.1 MeV/u carbon ion. The vertical dashed lines represent the positions that were simulated.

Table A.1: Comparison of variation in specific dose for 5 different variation conditions at different position of a 91 MeV/u Carbon ion beam

		Specific Dose variation (%)						
Depth (cm)	Condition	A	B	C	D	E	$\overline{\tilde{D}_{nuc}}$ (Gy)	D_{phys}(Gy)
0.5		35.6 ± 0.8	32.0 ± 0.8	14.9 ± 0.4	10.5 ± 0.3	6.2 ± 0.3	0.32 ± 0.01	0.32
1.5		36.3 ± 1.0	32.4 ± 0.8	17.9 ± 0.4	14.2 ± 0.3	5.6 ± 0.4	0.50± 0.01	0.51
1.75		37.5 ± 2.3	33.3 ± 0.7	19.7 ± 0.5	16.2 ± 0.3	5.4 ± 0.5	0.69 ±0.01	0.70
1.84		41.2 ±1.2	37.1 ± 0.9	24.0 ± 0.6	20.6 ± 0.5	5.5 ± 0.4	0.89 ± 0.1	0.90
1.94		47.8 ± 1.3	43.3 ± 1.1	31.5 ± 0.8	. 28.1 ± 0.7	7.0 ± 3.6	0.92 ± 0.5	1.0
2.04		63.2 ± 1.9	56.5 ± 1.5	42.1 ± 0.9	37.7 ± 0.9	8.1 ± 4.0	0.69 ± 0.01	0.71
2.1		86.9 ± 3.4	78.2 ± 1.8	65.3 ±1.4	59.7 ± 1.4	13.7 ± 6.7	0.41 ± 0.02	0.45
2.2		157.9 ± 19.3	140.8 ± 9.9	130.7 ± 9.5	120.2 ± 5.6	21.4 ± 6.5	0.02 ± 0.00	0.02

Table A.2: Comparison of variation in specific LET for 5 different variation conditions at different position of a 91 MeV/u Carbon ion beam

		Specific LET variation (%)							
Depth (cm)	Condition	A	B	C	D	E	$\overline{\tilde{L}_{nuc}}$ (Gy)	LET_f ($keV/\mu m$)	LET_d ($keV/\mu m$)
0.5		13.8 ± 0.8	11.3 ± 0.3	10.9 ± 0.3	10.5 ± 0.3	6.2 ± 0.3	29.8 ± 0.1	30.2	33.2
1.5		18.0 ± 0.8	15.3 ± 0.4	15.0 ± 0.4	14.2 ± 0.3	5.6 ± 0.4	43.0 ± 0.1	43.8	54.7
1.75		20.3 ± 0.7	17.5 ± 0.5	17.1 ± 0.5	16.2 ± 0.3	5.4 ± 0.5	58.5 ± 0.3	59.5	81.4
1.84		26.5 ± 1.0	23.0 ± 0.6	21.8 ± 0.5	20.6 ± 0.5	5.5 ± 0.4	79.2 ± 0.5	81.6	130.3
1.94		35.3 ± 1.6	30.8 ± 1.0	29.7 ± 0.8	28.1 ± 0.7	7.0 ± 3.6	91.4 ± 0.8	100.0	217.9
2.04		51.3 ± 2.0	45.1 ± 1.4	40.1 ± 1.0	7.7 ± 0.9	8.1 ± 4.0	99.1 ± 1.5	108.6	257.8
2.1		78.1 ± 2.4	70.6 ± 1.9	63.1 ± 1.4	59.7 ± 1.4	13.7 ± 6.7	89 ± 1.8	101.7	310.7
2.2		158.4 ± 23.1	145.7 ± 17.5	127.9 ± 9.5	120.2 ± 5.6	21.4 ± 6.5	7.2 ± 0.4	8.4	54.7

A.2 430.1 MeV/u Carbon ions

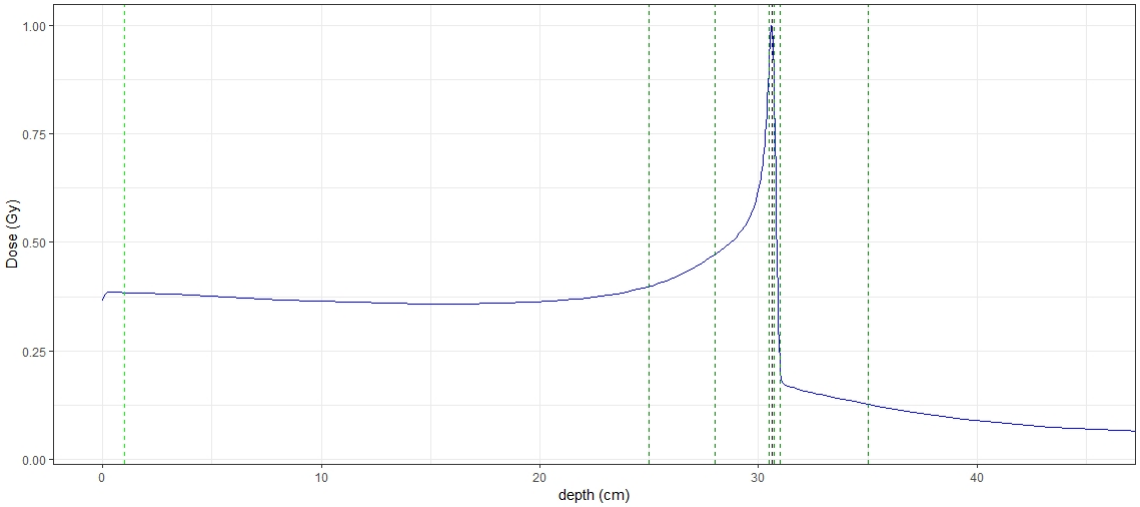

Figure A.2: Depth-dose profile for the 430.14 MeV/u carbon ion. The vertical dashed lines represent the positions that were simulated.

Table A.3: Comparison of variation in specific dose for 5 different variation conditions at different position of a 430. MeV/u Carbon ion beam

		Specific Dose variation (%)						
Depth (cm)	Condition	A	B	C	D	E	$\tilde{D}_{nuc}$ (Gy)	D_{phys}(Gy)
1		20.2 ± 0.6	17.9 ± 0.4	9.4 ± 0.2	7.5 ± 0.2	7.1 ± 0.2	0.37 ± 0.01	0.38
25		24.9 ± 0.7	22.0± 0.5	16.8 ± 0.2	15.5 ± 0.3	7.0 ± 0.6	0.40 ± 0.01	0.40
28		26.2 ± 0.8	23.3 ± 0.3	18.8 ± 0.4	17.1 ± 0.4	5.6 ± 0.5	0.47 ± 0.01	0.47
30.5		41.2 ± 1.4	36.9 ± 0.9	33.4 ± 0.9	30.9 ± 0.7	6.0 ± 2.3	0.91 ± 0.03	0.94
30.6		45.8 ± 1.5	41.1 ± 0.9	38.0 ± 0.9	35.2 ± 0.9	8.1 ± 6.3	0.93 ± 0.02	1.0
30.7		52.9 ± 1.5	47.1 ± 1.2	44.6 ± 1.0	41.8 ± 0.9	10.0 ± 7.5	0.79 ± 0.30	0.88
31		52.2 ± 2.2	44.2 ± 2.3	42.4 ± 2.2	40.1 ± 2.1	7.8 ± 2.4	0.20 ± 0.01	0.20
35		38.0 ± 1.8	33.8 ± 1.4	31.6 ± 1.1	29.6 ± 1.1	8.2 ± 0.7	0.13 ± 0.02	0.13

Table A.4: Comparison of variation in radiation quality for 5 different variation conditions at different position of a 430.14 MeV/u Carbon ion beam

Depth (cm)	Condition	Specific LET variation (%)					$\overline{\tilde{L}_{nuc}}$ (Gy)	LET_f ($keV/\mu m$)	LET_d ($keV/\mu m$)
		A	B	C	D	E			
1		9.4 ± 0.5	7.8 ± 0.2 7.7 ± 0.2	7.5 ± 0.2	7.1 ± 0.2	9.8 ± 0.1	10.3	10.8	
25		18.6 ± 0.6	16.3 ± 0.3	16.1 ± 0.4	15.5 ± 0.3	7.0 ± 0.6	9.3 ± 0.1	9.3	18.6
28		20.7 ± 0.7	18.3 ± 0.4	18.2 ± 0.4	17.1 ± 0.4	5.6 ± 0.5	10.3 ± 0.1 10.3	25.4	
30.5		37.4 ± 1.4	33.1 ± 0.9	32.9 ± 0.8	30.9 ± 0.7	6.0 ± 2.3	26.9 ± 0.3	28.0	146.2
30.6		42.7 ± 1.7	37.9 ± 0.9	37.6 ± 0.9	35.2 ± 0.9	8.1 ± 6.3	27.2 ± 0.3 29.5	204.9	
30.7		50.8 ± 2.1	44.7 ± 1.0	44.2 ± 1.0	41.8 ± 0.9	10.0 ± 7.5	21.5 ± 0.3 24.1	239.4	
31		46.9 ± 4.3	42.6 ± 2.6	42.1 ± 2.2	40.1 ± 2.1	7.8 ± 2.4	3.45 ± 0.05	3.4	46.0
35		35.4 ± 2.2	31.2 ± 1.2	31.3 ± 1.1	29.6 ± 1.1	8.2 ± 0.7	2.40 ± 0.03	2.3	15.8

Appendix B

LET Spectra Matching for the Experiments

B.1 Spectra Matching for MN1000 Sample

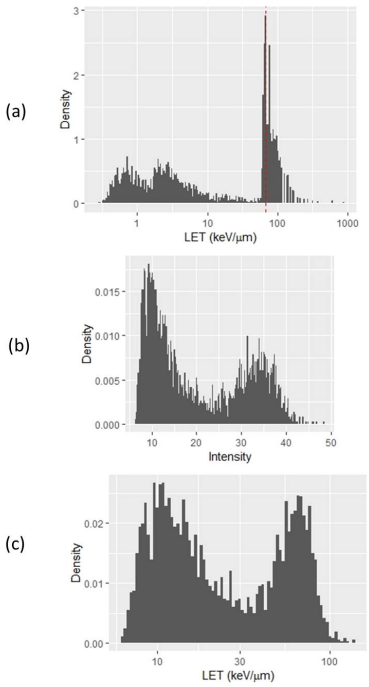

Figure B.1: Comparison of LET distribution of individual tracks for the MN1000 experiment obtained from MC simulations (a) and from FNTD measurements (c). The FNTD LET spectrum was obtained from the the track intensity spectrum (b), according to spectra matching procedure explained in section 5.2.

B.2 Spectra Matching for MN81000 Samples

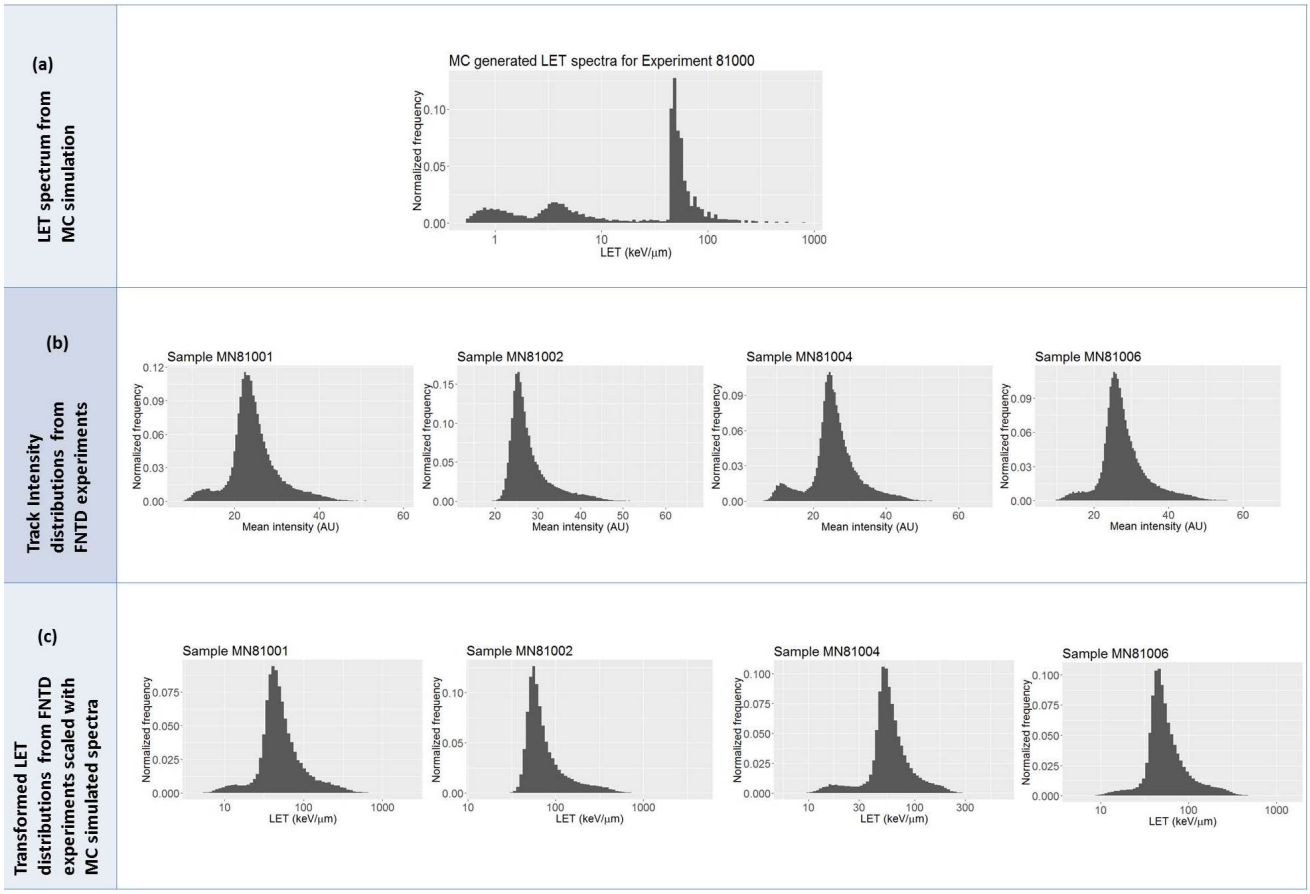

Figure B.2: Comparison of LET distribution of individual tracks for the different samples used in MN81000 experiment obtained from MC simulations (a) and from FNTD measurements (c). The FNTD LET spectrum was obtained from the the track intensity spectrum (b), according to spectra matching procedure explained in section 5.2.

B.3 Spectra Matching for MN12000 Samples

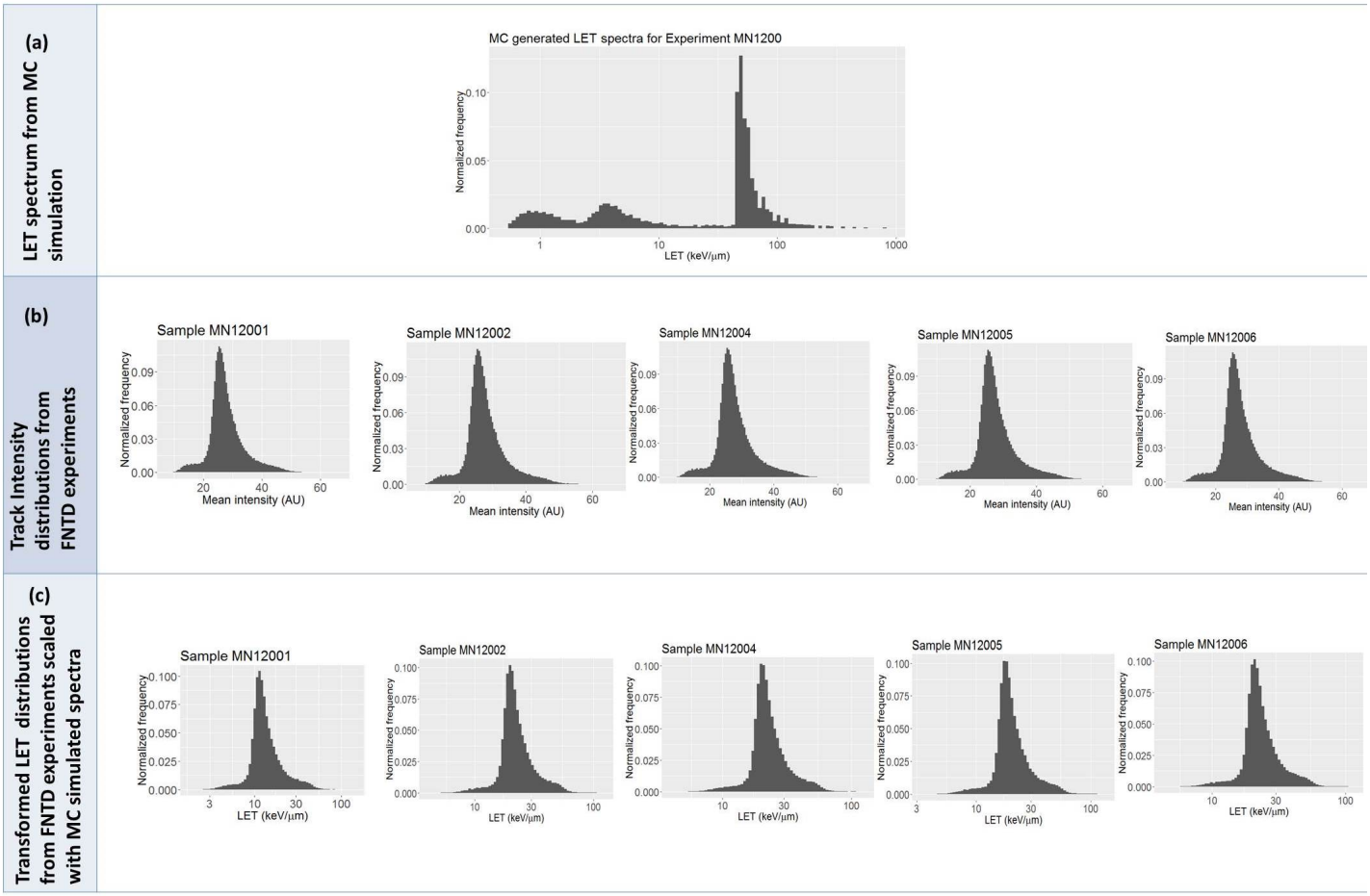

Figure B.3: Comparison of LET distribution of individual tracks for the different samples used in MN12000 experiment obtained from MC simulations (a) and from FNTD measurements (c). The FNTD LET spectrum was obtained from the the track intensity spectrum (b), according to spectra matching procedure explained in section 5.2.

B.4 Spectra Matching for SINF Samples

B.4.1 Entrance Channel

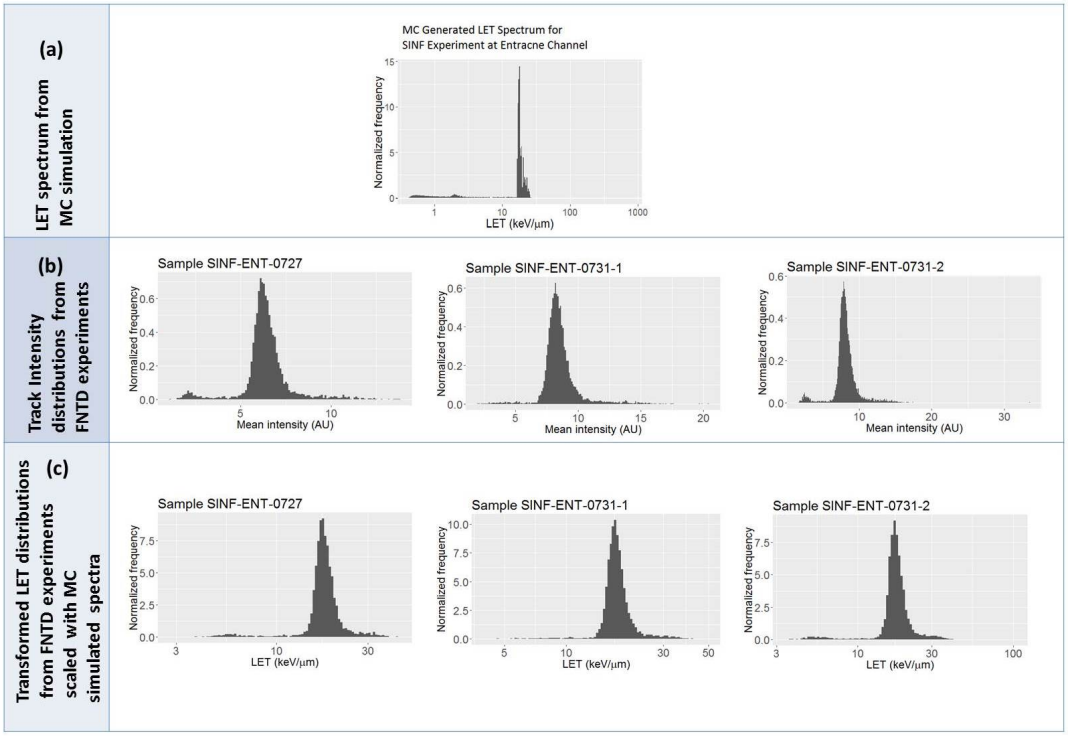

Figure B.4: Comparison of LET distribution of individual tracks for the different samples used in the entrance channel for the SINF experiment obtained from MC simulations (a) and from FNTD measurements (c). The FNTD LET spectrum was obtained from the the track intensity spectrum (b), according to spectra matching procedure explained in section 5.2.

B.4.2 SOBP

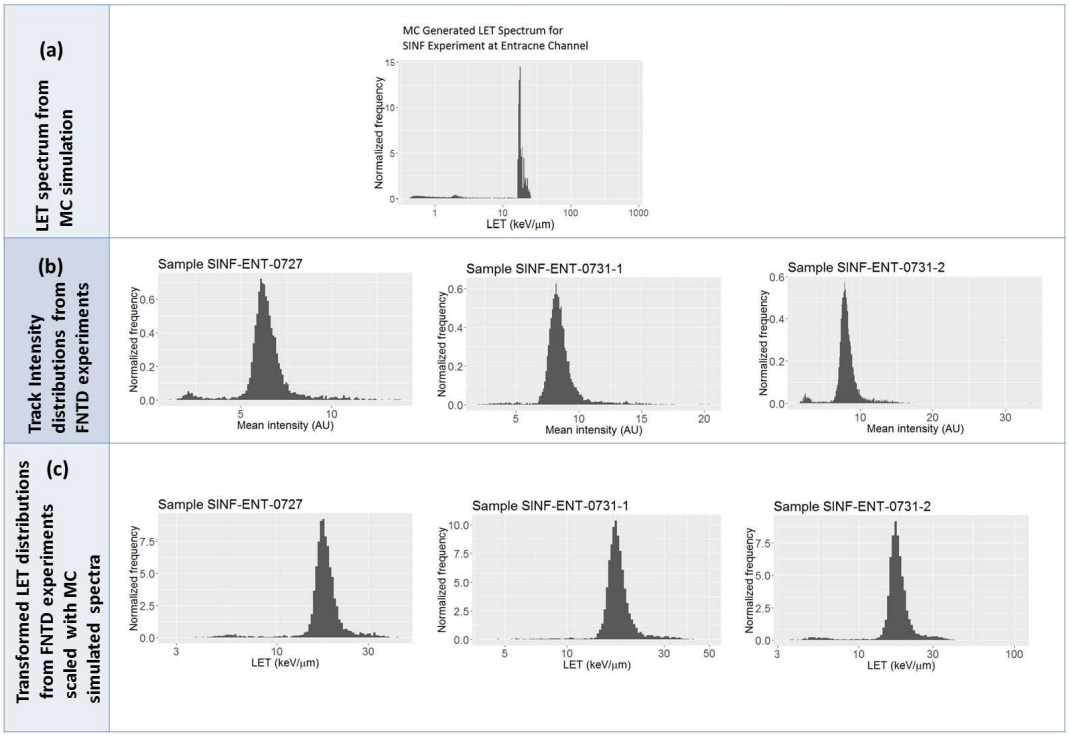

Figure B.5: Comparison of LET distribution of individual tracks for the different samples used in the SOBP for the SINF experiment obtained from MC simulations (a) and from FNTD measurements (c). The FNTD LET spectrum was obtained from the the track intensity spectrum (b), according to spectra matching procedure explained in section 5.2.

B.5 Spectra Matching for SR308 Samples

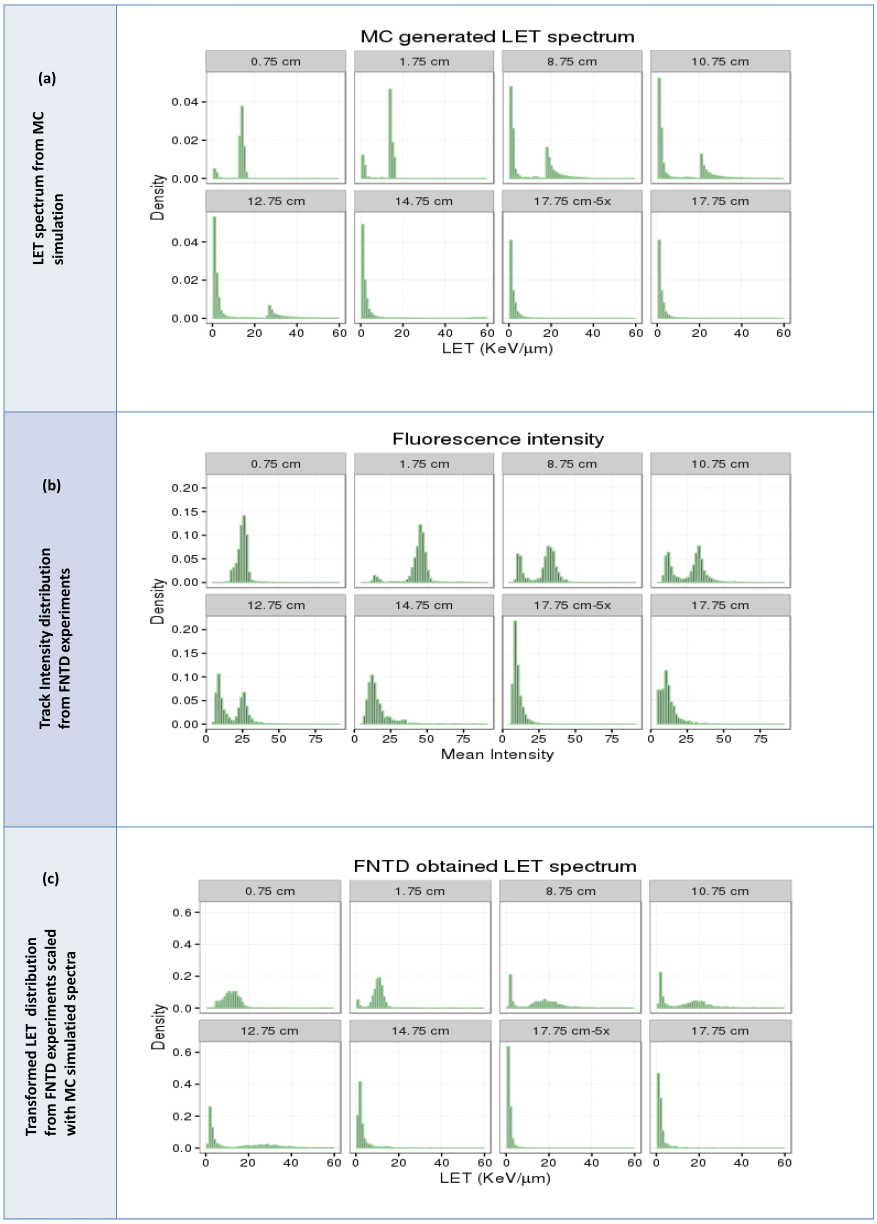

Figure B.6: Comparison of LET distribution of individual tracks for the different depths of SR308 experiments obtained from MC simulations (a) and from FNTD measurements (c). The FNTD LET spectrum was obtained from the the track intensity spectrum (b), according to spectra matching procedure explained in section 5.2.

Appendix C

Distributions of specific dose and specific LET

C.1 MN81000 samples

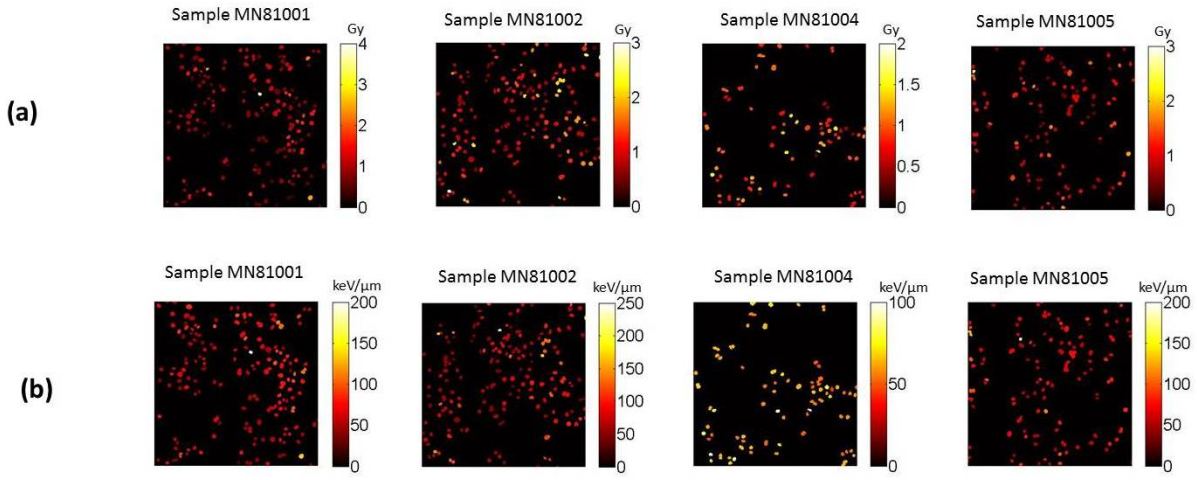

Figure C.1: Distribution of specific dose (a) and specific LET (b) shown as nuclear maps for different samples used in MN81000 experiments.

C.2 SR308 samples

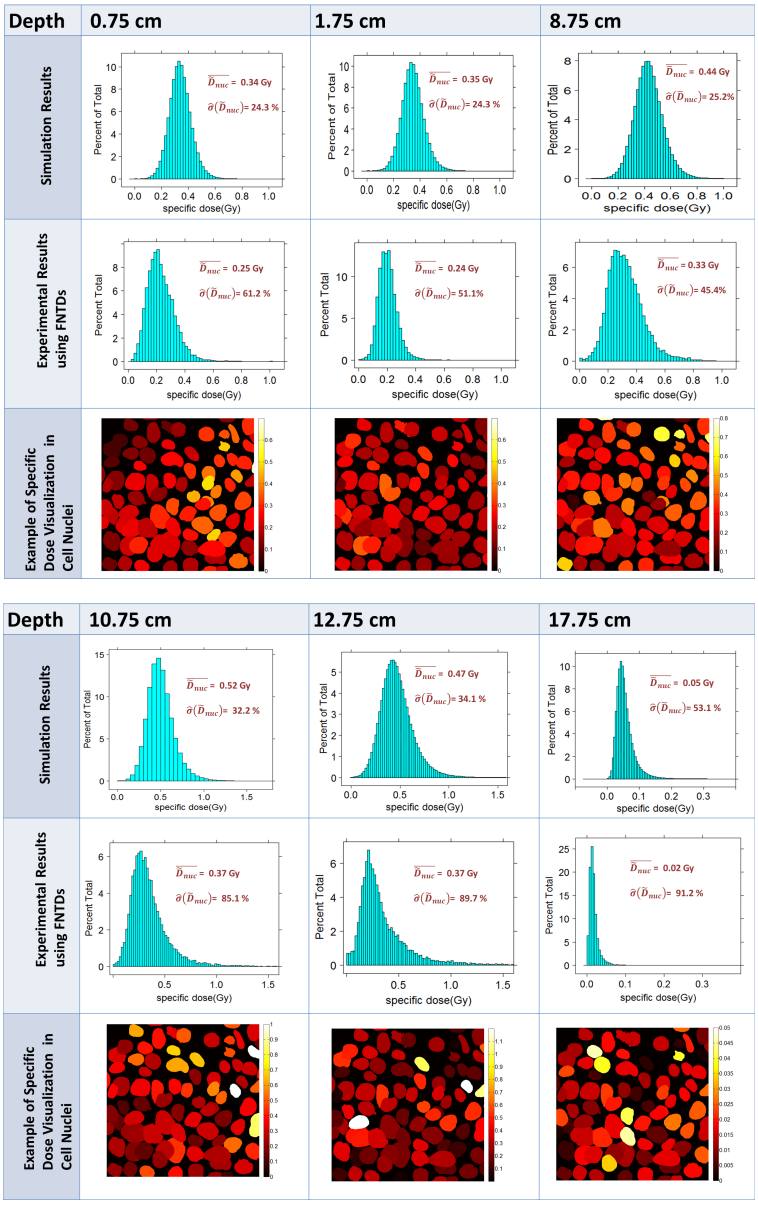

Figure C.2: Comparison of specific dose distributions between FNTD measurements (n = 27400) and simulated results ($n = 1x10^6$) for different depth positions of SR308 experiment.

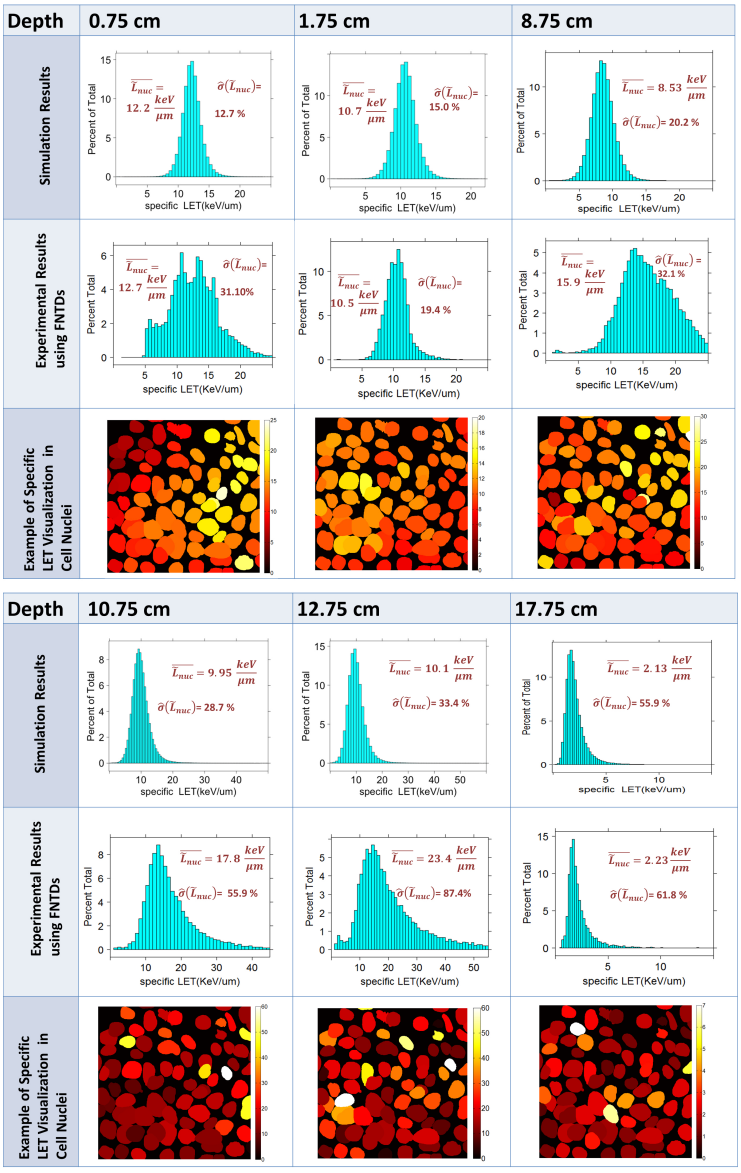

Figure C.3: Comparison of specific LET distributions between FNTD measurements (n = 27400) and simulated results ($n = 1x10^6$) for different depth positions of SR308 experiment.

List of Publications

Parts of this thesis have been published in the following publications:

Peer Reviewed Journals

S. Rahmanian, M. Niklas, A. Abdollahi, O. Jäkel, and S. Greilich, "Application of fluorescent nuclear track detectors for cellular dosimetry," *Physics in Medicine and Biology*, vol. 62, no. 7, pp. 2719–2740, 2017

C. H. McFadden, S. Rahmanian, D. B. Flint, S. J. Bright, D. S. Yoon, D. J. O'Brien, A. Asaithamby, A. Abdollahi, S. Greilich, and G. O. Sawakuchi, "Isolation of time-dependent DNA damage induced by energetic carbon ions and their fragments using fluorescent nuclear track detectors," *Medical Physics*, vol. 47, no. 1, pp. 272–281, 2020

Submitted for Publication

M. Niklas, J. Schlegel, H. Liew, D. Walsh, F. Zimmermann, O. Dzyubachyk, S. Rahmanian, T. Holland-Letz, J. Debus, and A. Abdollahi, "The biomedical sensor cell-fit-hd4d, reveals individual tumor cell fate in response to microscopic ion deposition," *Submitted to eLife*, 2020. BIORXIV/2020/987347

Bibliography

[1] J. F. Ward, "The Yield of DNA Double-strand Breaks Produced Intracellularly by Ionizing Radiation: A Review," *International Journal of Radiation Biology*, vol. 57, no. 6, pp. 1141–1150, 1990.

[2] S. P. Jackson and J. Bartek, "The DNA-damage response in human biology and disease," *Nature*, vol. 461, pp. 1071–1078, Oct. 2009.

[3] D. Schulz-Ertner, O. Jäkel, and W. Schlegel, "Radiation Therapy With Charged Particles," *Seminars in Radiation Oncology*, vol. 16, no. 4, pp. 249 – 259, 2006.

[4] D. Schardt, T. Elsässer, and D. Schulz-Ertner, "Heavy-ion tumor therapy: Physical and radiobiological benefits," *Rev. Mod. Phys.*, vol. 82, pp. 383–425, Feb. 2010.

[5] C. P. Karger and P. Peschke, "RBE and related modeling in carbon-ion therapy," *Physics in Medicine & Biology*, vol. 63, Dec. 2017.

[6] H. Bichsel, "Chapter one - stochastics of energy loss and biological effects of heavy ions in radiation therapy," in *Theory of Heavy Ion Collision Physics in Hadron Therapy* (D. Belkić, ed.), vol. 65 of *Advances in Quantum Chemistry*, pp. 1 – 38, Academic Press, 2013.

[7] M. Niklas, C. Melzig, A. Abdollahi, J. A. Bartz, M. S. Akselrod, J. Debus, O. Jäkel, and S. Greilich, "Spatial correlation between traversal and cellular response in ion radiotherapy - towards single track spectroscopy," *Radiation Measurements*, vol. 56, pp. 285–289, Feb. 2013.

[8] M. Niklas, S. Greilich, C. Melzig, M. S. Akselrod, O. Jäkel, and A. Abdollahi, "Engineering cell- fluorescent ion track hybrid detectors," *Radiation Oncology*, vol. 8, p. 141, 2013.

[9] I. Dokic, M. Niklas, F. Zimmermann, A. Mairani, P. Seidel, D. Krunic, O. Jäkel, J. Debus, S. Greilich, and A. Abdollahi, "Correlation of Particle Traversals with Clonogenic Survival Using Cell-Fluorescent Ion Track Hybrid Detector," *Frontiers in Oncology*, vol. 5, p. 275, 2015.

[10] F. H. Attix, *Introduction to radiological physics and radiation dosimetry*. John Wiley & Sons, New York, 1986.

[11] ICRU, "Stopping power and ranges for protons and alpha particles. report 49," Tech. Rep. 49, International Commission on Radiation Units and Measurements, ICRU, 7910 Woodmont Avenue, Bethesda, Maryland 20814, USA, 1993.

[12] E. Rutherford, "The scattering of α and β particles by matter and structure of the atom," *Philosophical Magazine*, vol. 21, 5 1911.

[13] H. Bethe, "Moliere's theory of multiple scattering," *Physical review*, vol. 89, no. 6, pp. 1256–1266, 1952.

[14] L. Highland, "Some practical remarks on multiple scattering," *Nucl. Instr. and Meth*, vol. 129, no. 2, pp. 497–499, 1975.

[15] ICRU, "ICRU Report 85: Fundamental Quantities and Units for Ionizing Radiation," *Journal of the International Commission on Radiation Units and Measurements*, vol. 11, April 2011.

[16] L. Papiez and J. J. Battista, "Radiance and particle fluence," *Physics in Medicine and Biology*, vol. 39, pp. 1053–1062, June 1994.

[17] M. Krämer and M. Durante, "Ion beam transport calculations and treatment plans in particle therapy," *The European Physical Journal D*, vol. 60, no. 1, pp. 195–202, 2010.

[18] H. Nikjoo, S. Uehara, D. Emfietzoglou, and F. Cucinotta, "Track-structure codes in radiation research," *Radiation Measurements*, vol. 41, no. 9, pp. 1052 – 1074, 2006.

[19] J. J. Butts and R. Katz, "Theory of RBE for heavy ion bombardment of dry enzymes and viruses," *Radiation Research*, vol. 30, no. 4, pp. 855–871, 1967.

[20] G. Kraft, M. Krämer, and M. Scholz, "LET, track structure and models," *Radiation and Environmental Biophysics*, vol. 31, pp. 161–180, 1992.

[21] ICRU, "ICRU 36: Microdosimetry," tech. rep., International Commission on Radiation Units and Measurements, ICRU, 7910 Woodmont Avenue, Bethesda, Maryland 20814, USA, 1983.

[22] R. Brun, F. Bruyant, F. Carminati, S. Giani, M. Maire, A. McPherson, G. Patrick, and L. Urban, "GEANT Detector Description and Simulation Tool," 1994. report numbers: CERN-W5013, CERN-W-5013, W5013, W-5013. URL= http://inspirehep.net/record/863473/files/geantall_ CERN-W5013.pdf.

[23] L. Landau, "56 - on the energy loss of fast particles by ionisation," in *Collected Papers of L.D. Landau* (D. T. HAAR, ed.), pp. 417 – 424, Pergamon, 1965.

[24] P. V. Vavilov, "Ionization losses of high-energy heavy particles," *Sov. Phys. JETP*, vol. 5, pp. 749–751, 1957.

[25] H. Paganetti, A. Niemierko, M. Ancukiewicz, L. E. Gerweck, M. Goitein, J. S. Loeffler, and H. D. Suit, "Relative biological effectiveness (RBE) values for proton beam therapy," *International Journal of Radiation Oncology, Biology, Physics*, vol. 53, pp. 407–421, June 2002.

[26] B. S. Sørensen, J. Overgaard, and N. Bassler, "In vitro RBE-LET dependence for multiple particle types," *Acta Oncologica*, vol. 50, no. 6, pp. 757–762, 2011.

[27] E. Hall and A. Giaccia, *Radiobiology for the Radiologist*, vol. 6. Lippincott Williams & Wilkins Philadelphia, 2006.

[28] S. E. Combs, O. Jäkel, T. Haberer, and J. Debus, "Particle therapy at the heidelberg ion therapy center (HIT); integrated research-driven university-hospital-based radiation oncology service in heidelberg, germany," *Radiotherapy and Oncology*, vol. 95, no. 1, pp. 41–44, 2010.

[29] M. Scholz and G. Kraft, "Track structure and the calculation of biological effects of heavy charged particles," *Advances in space research : the official journal of the Committee on Space Research (COSPAR)*, vol. 18, pp. 5–14, Feb. 1996.

[30] M. Krämer and M. Scholz, "Treatment planning for heavy-ion radiotherapy: calculation and optimization of biologically effective dose," *Physics in Medicine and Biology*, vol. 45, pp. 3319–3330, Nov. 2000.

[31] R. Grün, T. Friedrich, T. Elsässer, M. Krämer, K. Zink, C. P. Karger, M. Durante, R. Engenhart-Cabillic, and M. Scholz, "Impact of enhancements in the local effect model (LEM) on the predicted RBE-weighted target dose distribution in carbon ion therapy," *Physics in Medicine and Biology*, vol. 57, pp. 7261–7274, Nov. 2012.

[32] M. Scholz, A. M. Kellerer, W. Kraft-Weyrather, and G. Kraft, "Computation of cell survival in heavy ion beams for therapy," *Radiation and Environmental Biophysics*, vol. 36, no. 1, pp. 59–66, 1997.

[33] T. Elsässer and M. Scholz, "Cluster Effects within the Local Effect Model," *Radiation Research*, vol. 167, no. 3, pp. 319 – 329, 2007.

[34] T. Elsässer, M. Krämer, and M. Scholz, "Accuracy of the local effect model for the prediction of biologic effects of carbon ion beams ¡em¿in vitro¡/em¿ and ¡em¿in vivo¡/em¿," *International Journal of Radiation Oncology *Biology *Physics*, vol. 71, no. 3, pp. 866–872, 2008.

[35] T. Friedrich, U. Scholz, T. Elsässer, M. Durante, and M. Scholz, "Calculation of the biological effects of ion beams based on the microscopic spatial damage distribution pattern," *International Journal of Radiation Biology*, vol. 88, no. 1-2, pp. 103–107, 2012.

[36] T. Inaniwa, T. Furukawa, Y. Kase, N. Matsufuji, T. Toshito, Y. Matsumoto, Y. Furusawa, and K. Noda, "Treatment planning for a scanned carbon beam with a modified microdosimetric kinetic model," *Physics in Medicine and Biology*, vol. 55, pp. 6721–6737, Oct. 2010.

[37] R. B. Hawkins, "A microdosimetric-kinetic model for the effect of non-Poisson distribution of lethal lesions on the variation of RBE with LET," *Radiation Research*, vol. 160, pp. 61–69, July 2003.

[38] Y. Kase, T. Kanai, Y. Matsumoto, Y. Furusawa, H. Okamoto, T. Asaba, M. Sakama, and H. Shinoda, "Microdosimetric Measurements and Estimation of Human Cell Survival for Heavy-Ion Beams," *Radiation Research*, vol. 166, no. 4, pp. 629 – 638, 2006.

[39] Y. Kase, T. Kanai, N. Matsufuji, Y. Furusawa, T. Elsässer, and M. Scholz, "Biophysical calculation of cell survival probabilities using amorphous track structure models for heavy-ion irradiation," *Physics in Medicine and Biology*, vol. 53, pp. 37–59, Dec. 2007.

[40] G. Akselrod, M. Akselrod, E. Benton, and N. Yasuda, "A novel al2o3 fluorescent nuclear track detector for heavy charged particles and neutrons," *Nuclear Instruments and Methods in Physics Research Section B: Beam Interactions with Materials and Atoms*, vol. 247, no. 2, pp. 295 – 306, 2006.

[41] M. Niklas, A. Abdollahi, M. S. Akselrod, J. Debus, O. Jäkel, and S. Greilich, *Novel hybrid detector for radiobiological investigations in clinical ion beams*, vol. 111. Elsevier, 2014.

[42] M. Niklas, A. Abdollahi, M. S. Akselrod, J. Debus, O. Jäkel, and S. Greilich, "Subcellular spatial correlation of particle traversal and biological response in clinical ion beams," *International Journal of Radiation Oncology*Biology*Physics*, vol. 87, pp. 1141–1147, 2013.

[43] M. Folkard, B. Vojnovic, K. Prise, and B. Michael, "The application of charged-particle microbeams in radiobiology," *Nucl. Ins. Meth. B*, vol. 188, pp. 49–54, April 2002.

[44] J.-M. Osinga, I. Ambrožová, K. Pachnerová Brabcová, M. S. Akselrod, O. Jäkel, M. Davídková, and S. Greilich, "Single track coincidence measurements of fluorescent and plastic nuclear track detectors in therapeutic carbon beams," *Journal of Instrumentation*, vol. 9, p. P04013, 2014.

[45] A. P. Fews and D. L. Henshaw, "High resolution alpha particle spectroscopy using CR-39 plastic track detector," *Nuclear Instruments and Methods*, vol. 197, pp. 517–529, 1982.

[46] M. S. Akselrod and G. J. Sykora, "Fluorescent nuclear track detector technology - A new way to do passive solid state dosimetry," *Radiation Measurements*, vol. 46, pp. 1671–1679, 2011.

[47] S. Sanyal and M. Akselrod, "Anisotropy of optical absorption and fluorescence in al2o3:c,mg crystals," *Journal of Applied Physics*, vol. 98, pp. 033518–033518, Aug. 2005.

[48] J. Pawley, *Handbook of Biological Confocal Microscopy*. Springer, 2006.

[49] C. Z. Microscopy, "Lsm 710." URL http://www.zeiss.com/.

[50] C. H. McFadden, T. M. Hallacy, D. B. Flint, D. A. Granville, A. Asaithamby, N. Sahoo, M. S. Akselrod, and G. O. Sawakuchi, "Time-lapse monitoring of dna damage colocalized with particle tracks in single living cells," *International Journal of Radiation Oncology*Biology*Physics*, vol. 96, no. 1, pp. 221 – 227, 2016.

[51] C. H. McFadden, S. Rahmanian, D. B. Flint, S. J. Bright, D. S. Yoon, D. J. O'Brien, A. Asaithamby, A. Abdollahi, S. Greilich, and G. O. Sawakuchi, "Isolation of time-dependent DNA damage induced by energetic carbon ions and their fragments using fluorescent nuclear track detectors," *Medical Physics*, vol. 47, no. 1, pp. 272–281, 2020.

[52] M. Niklas, J. Schlegel, H. Liew, D. Walsh, F. Zimmermann, O. Dzyubachyk, S. Rahmanian, T. Holland-Letz, J. Debus, and A. Abdollahi, "The biomedical sensor cell-fit-hd4d, reveals individual tumor cell fate in response to microscopic ion deposition," *Submitted to eLife*, 2020. BIORXIV/2020/987347.

[53] M. A. Niklas, *Cell-fluorescent ion track hybrid detector: A novel hybrid technology for direct correlation of single ion tracks and subcellular damage sites in clinical ion beam.* PhD thesis, Department of Physics and Astronomy, Heidelberg University, 2014.

[54] D. J. Giard, S. A. Aaronson, G. J. Todaro, P. Arnstein, J. H. Kersey, H. Dosik, and W. P. Parks, "In Vitro Cultivation of Human Tumors: Establishment of Cell Lines Derived From a Series of Solid Tumors2," *JNCI: Journal of the National Cancer Institute*, vol. 51, pp. 1417–1423, 11 1973.

[55] M. Niklas, S. Greilich, C. Melzig, M. S. Akselrod, O. Jäkel, and A. Abdollahi, "Engineering cell- fluorescent ion track hybrid detectors," *Radiation Oncology*, vol. 8, p. 141, 2013.

[56] Biolegen, "Draq5." URL=https://www.biolegend.com/en-us/products/draq5-9674, (accessed 15 December 2019).

[57] H. Cen, F. Mao, I. Aronchik, R. J. Fuentes, and G. L. Firestone, "Devd-nucview488: a novel class of enzyme substrates for real-time detection of caspase-3 activity in live cells," *The FASEB Journal*, vol. 22, no. 7, pp. 2243–2252, 2008. PMID: 18263700.

[58] T. Nagai, K. Ibata, E. S. Park, M. Kubota, K. Mikoshiba, and A. Miyawaki, "A variant of yellow fluorescent protein with fast and efficient maturation for cell-biological applications," *Nature Biotechnology*, vol. 20, no. 1, pp. 87–90, 2002.

[59] N. C. Shaner, R. E. Campbell, P. A. Steinbach, B. N. G. Giepmans, A. E. Palmer, and R. Y. Tsien, "Improved monomeric red, orange and yellow fluorescent proteins derived from discosoma sp. red fluorescent protein," *Nature Biotechnology*, vol. 22, no. 12, pp. 1567–1572, 2004.

[60] The R Foundation, "The R project for statistical computing." URL=https://www.r-project.org/.

[61] Rstudio. URL=https://rstudio.com/.

[62] Mathworks, "Matlab." URL=https://www.mathworks.com/products/matlab.html.

[63] J. Schindelin, I. Arganda-Carreras, E. Frise, V. Kaynig, M. Longair, T. Pietzsch, S. Preibisch, C. Rueden, S. Saalfeld, B. Schmid, J.-Y. Tinevez, D. J. White, V. Hartenstein, K. Eliceiri, P. Tomancak, and A. Cardona, "Fiji: an open-source platform for biological-image analysis," *Nature methods*, vol. 9, pp. 676–682, June 2012.

[64] C. A. Schneider, W. S. Rasband, and K. W. Eliceiri, "Nih image to imagej: 25 years of image analysis," *Nature Methods*, vol. 9, no. 7, pp. 671–675, 2012.

[65] S. Greilich and Colleagues, "Package libamtrack." URL=https://libamtrack.dkfz.de/libamtrack.

[66] S. Greilich and Colleagues, "Package hitxml." URL=https://r-forge.r-project.org/projects/hitxml/.

[67] S. Greilich and Colleagues, "Fntd project," 2015. URL=https://fntd.dkfz.de/fntd/index.php/Homepage_of_the_DKFZ_FNTD_Project.

[68] MOSAIC Group (MPI-CBG), "Mosaicsuite for imagej and fiji models, simulation and algorithms for interdisciplinary computing." URL=http://mosaic.mpi-cbg.de.

[69] I. F. Sbalzarini and P. Koumoutsakos, "Feature point tracking and trajectory analysis for video imaging in cell biology," *Journal of Structural Biology*, vol. 151, no. 2, pp. 182–195, 2005.

[70] J. A. Bartz, S. Kodaira, M. Kurano, N. Yasuda, and M. S. Akselrod, "High resolution charge spectroscopy of heavy ions with FNTD technology," *Nuclear Instruments and Methods in Physics Research B*, vol. 335, pp. 24–30, Sept. 2014.

[71] J. J. Kouwenberg, L. Ulrich, O. Jäkel, and S. Greilich, "A 3d feature point tracking method for ion radiation," *Physics in Medicine & Biology*, vol. 61, no. 11, p. 4088, 2016.

[72] A. Ferrari, P. R. Sala, A. Fasso, and J. Ranft, "FLUKA: A multi-particle transport code," 2005. DOI: 10.2172/877507, URL=http://www.fluka.org/fluka.php.

[73] E. G. Yukihara, B. A. Doull, M. Ahmed, S. Brons, T. Tessonnier, O. Jäkel, and S. Greilich, "Time-resolved optically stimulated luminescence of Al2o3: C for ion beam therapy dosimetry," *Physics in Medicine and Biology*, vol. 60, no. 17, pp. 6613–6638, 2015.

[74] S. Rahmanian, M. Niklas, A. Abdollahi, O. Jäkel, and S. Greilich, "Application of fluorescent nuclear track detectors for cellular dosimetry," *Physics in Medicine and Biology*, vol. 62, no. 7, pp. 2719–2740, 2017.

[75] F. A. Cucinotta, J. W. Wilson, M. R. Shavers, and R. Katz, "Calculation of heavy ion inactivation and mutation rates in radial dose model of track structure," *NASA Technical Paper*, vol. 3, p. 11, 1997.

[76] A. M. Kellerer, "Chord-length distributions and related quantities for spheroids," *Radiation Research*, vol. 98, no. 3, pp. 425–437, 1984.

[77] S. Seltzer and M. Berger, "Evaluation of the Collision Stopping Power of Elements and Compounds for Electrons and Positrons," *Int. J. Appl. Radiat. Isot.*, vol. 33, pp. 1189–1218, 1982.

[78] W. Leo, *Techniques for Nuclear and Particle Physics Experiments: A How-to Approach*. Springer, 1994.

[79] G. Klimpki, H. Mescher, M. S. Akselrod, O. Jäkel, and S. Greilich, "Fluence-based dosimetry of proton and heavier ion beams using single track detectors," *Physics in Medicine and Biology*, vol. 61, no. 3, pp. 1021–1040, 2016.

[80] S. Greilich, L. Ulrich, J. J. M. Kouwenberg, and S. Rahmanian, "Measurement of fluence, LET, and dose in a carbon ion spread-out Bragg-peak using fluores-

cent nuclear track detectors and an automated reader," 2016. arXiv preprint arXiv:1610.05054. URL=https://arxiv.org/abs/1610.05054v3.

[81] G. Klimpki, H. Mescher, M. S. Akselrod, O. Jäkel, and S. Greilich, "Fluence-based dosimetry of proton and heavier ion beams using single track detectors," *Physics in Medicine and Biology*, vol. 61, no. 3, pp. 1021–1040, 2016.

[82] S. Greilich, J. Jansen, A. Neuholz, A. Stadler, H. Mescher, and G. Klimpki, "Evaluation of Additional Track Parameters from Fluorescent Nuclear Track Detectors to Determine the LET of Individual Ions," *Radiation Protection Dosimetry*, vol. 180, pp. 206–209, Oct. 2017.

[83] B. Marples, P. Lambin, K. A. Skov, and M. C. Joiner, "Low dose hyper-radiosensitivity and increased radioresistance in mammalian cells," *International Journal of Radiation Biology*, vol. 71, pp. 721–735, June 1997.

[84] K. M. Prise, M. Folkard, A. M. Malcolmson, C. H. Pullar, G. Schettino, A. G. Bowey, and B. D. Michael, "Single ion actions: the induction of micronuclei in V79 cells exposed to individual protons," *Advances in space research: the official journal of the Committee on Space Research (COSPAR)*, vol. 25, no. 10, pp. 2095–2101, 2000.

[85] K. M. Prise, O. V. Belyakov, M. Folkard, A. Ozols, G. Schettino, B. Vojnovic, and B. D. Michael, "Investigating the cellular effects of isolated radiation tracks using microbeam techniques," *Advances in space research: the official journal of the Committee on Space Research (COSPAR)*, vol. 30, no. 4, pp. 871–876, 2002.

[86] J.-M. Osinga, M. Akselrod, R. Herrmann, V. Hable, G. Dollinger, O. Jäkel, and S. Greilich, "High-accuracy fluence determination in ion beams using fluorescent nuclear track detectors," *Radiation Measurements*, vol. 56, pp. 294 – 298, 2013. Proceedings of the 8th International Conference on Luminescent Detectors and Transformers of Ionizing Radiation (LUMDETR 2012).

[87] H. Palmans, H. Rabus, A. L. Belchior, M. U. Bug, S. Galer, U. Giesen, G. Gonon, G. Gruel, G. Hilgers, D. Moro, H. Nettelbeck, M. Pinto, A. Pola, S. Pszona, G. Schettino, P. H. G. Sharpe, P. Teles, C. Villagrasa, and J. J. Wilkens, "Future development of biologically relevant dosimetry," *The British Journal of Radiology*, vol. 88, no. 1045, p. 20140392, 2015.

[88] A. Verkhovtsev, E. Surdutovich, and A. V. Solov'yov, "Multiscale approach predictions for biological outcomes in ion-beam cancer therapy," *Scientific Reports*, vol. 6, p. 27654, June 2016.

[89] K. M. Prise, M. Folkard, and B. D. Michael, "A review of the bystander effect and its implications for low-dose exposure," *Radiation protection dosimetry*, vol. 104, no. 4, pp. 347–355, 2003.

Acknowledgements

I would like to acknowledge and express my gratitude to everyone who contributed in different ways to the work presented here and supported me during the course of my PhD thesis.
First, I wish to thank Prof. Dr. Oliver Jäkel, head of the department of Medical Physics in Radiation Oncology at DKFZ, for accepting me as a PhD student in his department and for his great support, supervision, and feedback throughout my PhD work.
I would also like to thank Prof. João Seco, head of the division Biomedical Physics in Radiation Oncology (DKFZ), along with Prof. Dr. Oliver Jäkel, for being the referees of this thesis. I am also grateful for Prof. Dr. Nobert Herrmann and Prof. Dr. Björn-Malte Schäfer, from University of Heidelberg, for agreeing to act as examiners in the disputation of this thesis. I would also like to give special thanks to Dr. Wolfgang Schlegel for his support during the initial phase of my PhD.
I am specially thankful for Dr. Steffen Greilich for accepting me into his research group, Ion Beam Therapy. I am extremely grateful for his supervision throughout this work and guiding me to pursue interesting research ideas.
I would like to thank Prof. Dr. Oliver Jäkel, Dr. Steffen Greilich, Prof. Dr. Christian Karger and Dr. Dr. Amir Abdollahi for serving as members in my thesis advisory committee and giving me feedback and advice in how to proceed with my work.
I would like to thank the members of Clinical Cooperation Unit Translational Radiation Oncology at DKFZ for providing cell experimental data for the FNTDs and familiarizing me with the radiobiological experiments. Particularly, I am grateful to Dr. Amir Abdollahi for his support with the joint project and Dr. Martin Niklas for his collaboration and help with the data analysis.
I wish to thank our colleagues from MD Anderson for their collaboration on the SINF project. I am thankful for Dr. Gabriel Sawakuchi and his research team for exceptional team work and hosting my stay at their research institute. I would also like to thank Conor McFadden for being a great host and an excellent research partner and his

immense help with the project and preparing the manuscript.
I would like thank the members of E408 and E406 for their support at group meetings, and fruitful discussion during coffee breaks including Alex, Josephine, Tom, Christian, Alexey, Kim, Tim, Julia, Leonie, Jeannette, Renato, Laura, Frank and all the other members of the group. I would like to give a special thank to Alex Neuholz for always helping with FNTD reader and keeping a cheerful atmosphere in the office. A special thanks also goes for Tim Gehrke for his constant encouragement and his help with the German translation.
I would also like to thank the entire members of E040 department for providing a great working atmosphere and having fruitful seminars that inspired many great ideas. I would like to thank the members of DKFZ core facility for providing microscopy and help with the operations. I would also like to thank Heidelberg Ion Therapy Center for providing beam time for the irradiations. I am specially thankful for Dr. Stephan Brons with his never ending support at HIT.
I would like to thank the DKFZ graduate school for providing the funds to carry out this work and for their ongoing support.
I would like to thank all my friends that I met in Heidelberg and DKFZ. Without their support and encouragement, I wouldn't be able to succeed. I am specially thankful for Fereydoon Taheri and Azer Acikgöz for always being there for me no matter what and helping me to correct this thesis. Special thanks goes to my friend Bouchra Tawk for supporting me through all the stages of my stay at Heidelberg. I would also like to thank all the other friends that I didn't mention by name who made me feel welcomed and helped me throughout my PhD work.
Finally, but not least, I would like to thank my family. My parents and my brothers have been my rock throughout this journey, and none of this would have been possible without them. Thank you for your love and support!